THE UNIVERSITY *of* EDINBURGH

Model-Based Reconstruction of Accelerated Quantitative Magnetic Resonance Imaging (MRI)

Wajiha Bano

A thesis submitted for the degree of Doctor of Philosophy.
The University of Edinburgh.
May 2019

"Nothing in life is to be feared, it is only to be understood. Now is the time to understand more, so that we may fear less."

- Marie Curie

Abstract

Quantitative MRI refers to the determination of quantitative parameters (T_1,T_2,diffusion, perfusion etc.) in magnetic resonance imaging (MRI). The 'parameter maps' are estimated from a set of acquired MR images using a parameter model, i.e. a set of mathematical equations that describes the MR images as a function of the parameter(s). A precise and accurate high-resolution estimation of the parameters is needed in order to detect small changes and/or to visualize small structures. Particularly in clinical diagnostics, the method provides important information about tissue structures and respective pathologic alterations. Unfortunately, it also requires comparatively long measurement times which preclude widespread practical applications. To overcome such limitations, approaches like Parallel Imaging (PI) and Compressed Sensing (CS) along with the model-based reconstruction concept has been proposed. These methods allow for the estimation of quantitative maps from only a fraction of the usually required data.

The present work deals with the model-based reconstruction methods that are applicable for the most widely available Cartesian (rectilinear) acquisition scheme. The initial implementation was based on accelerating the T_2^* mapping using Maximum Likelihood estimation and Parallel Imaging (PI). The method was tested on a Multiecho Gradient Echo (MEGE) T_2^* mapping experiment in a phantom and a human brain with retrospective undersampling. Since T_2^* is very sensitive to phase perturbations as a result of magnetic field inhomogeneity further work was done to address this. The importance of coherent phase information in improving the accuracy of the accelerated T_2^* mapping fitting was investigated. Using alternating minimization, the method extends the MLE approach based on complex exponential model fitting which avoids loss of phase information in recovering T_2^* relaxation times. The implementation of this method was tested on prospective(real time) undersampling in addition to retrospective. Compared with fully sampled reference scans, the use of phase information reduced the error of the accelerated T_2^* maps by up to 20% as compared to baseline magnitude-only method. The total scan time for the four times accelerated 3D T_2^* mapping was 7 minutes which is clinically acceptable. The second main part of this thesis focuses on the development of a model-based super-resolution framework for the T_2 mapping. 2D multi-echo spin-echo (MESE) acquisitions suffer from low spatial resolution in the slice dimension. To overcome this limitation while keeping acceptable scan times, we combined a classical super-resolution method with an iterative model-based reconstruction to reconstruct T_2 maps from highly undersampled MESE data. Based on an optimal protocol determined from simulations, we were able to reconstruct $1mm^3$ isotropic T_2 maps of both phantom and healthy volunteer data. Comparison of T_2 values obtained with the proposed method with fully sampled reference MESE results showed good agreement. In summary, this thesis has introduced new approaches to employ signal models in different applications, with the aim of either accelerating an acquisition, or improving the accuracy of an existing method. These approaches may help to take the next step away from qualitative towards a fully quantitative MR imaging modality, facilitating precision medicine and personalized treatment.

Lay Summary

Magnetic Resonance Imaging (MRI) is a medical imaging technique that allows us to take very detailed pictures with the help of magnetic field. This magnetic field is generated by a huge donut shaped magnet along with other intricate mechanisms to generate the picture. The data collection to make the images is a slow process and a scan takes 45-60 minutes to complete generally. From a patient's point of view it is not very comfortable to lay still in the scanner and it is noisy. Nevertheless, the utility of MRI for the detection of various neurological condition is unprecedented. The images generated by the MRI are interpreted by a radiologist who is trained to read these images. These qualitative images are subjective in nature and can be influenced by various confounding factors. Quantitative MRI can be useful in comparing the scans amongst different populations and different sites or to study the disease progression of a same subject. Various quantitative techniques have been developed over the years which are very accurate and precise. However, these techniques take much longer than the conventional MRI and hence cannot be applied widely in clinical scenarios. In this thesis I am using various mathematical techniques to produce the images from less amount of data which reduces the scan time.

The thesis has taken the development of quantitative MRI to be applicable in the clinical practice and so all the work has been implemented on the clinical scanners with a focus on the brain imaging. For the first part of the thesis, the scan time of the quantitative MRI was reduced to 7 minutes from 21 minutes. In the second part, I investigated the possibility of acquiring quantitative MRI with a much higher details and in less time. The scan time of this technique was 10 times less than the original scan. This is encouraging results which hopefully will be explored further. Reducing the scan time of quantitative MRI will allow its application in the clinical practice and will increase patient comfort, but more importantly cut down on costs.

Declaration of originality

I hereby declare that the research recorded in this thesis and the thesis itself was composed and originated entirely by myself in the School of Engineering at The University of Edinburgh.

Wajiha Bano

Acknowledgements

The completion of this thesis would not have been possible without the support and encouragement of several special people. Hence, I would like to take this opportunity to show my gratitude to those who have assisted me in a myriad of ways. I would first like to express my heartfelt thanks to my supervisors Prof. Mike Davies and Prof. Ian Marshall. They are the most supportive and considerate supervisors I could have asked for. I have gone to Mike countless times dejected with tears in my eyes and he has always listened compassionately and encouraged me. His willingness to offer me so much of his time and intellect is the major reason this thesis was completed. In addition, Ian's support has been instrumental throughout this project. Whether it was a strange inexplicable scanner fault or the complicated EPIC code, Ian has always been there to help. His words of encouragement have kept me motivated during the past four years. I want to thank the examiners Dr. Gillian Macnaught and Dr. David Atkinson for their precious time in evaluating my thesis.

This PhD couldnot have been possible without the generous funding from sparse representations and compressed sensing network (SpaRTaN) which is part of the Marie Curie Actions-Initial Training Networks (ITN). I got the opportunity to travel and attend various workshops through this network and also got the chance to meet young researchers working in the same field. I would like to thank the coordinators of the SpaRTaN, Mark Plumbley and Helen Cooper for managing the project so smoothly and arranging very helpful workshops and networking events. A key source of help that unlocked the potential of this project, was assistance from Mohammad Golbabaee. Not only did he help me with writing the codes but also offered useful information and advice. I also would like to thank my colleague Arnold Benjamin who has been with me since day one. From sorting out k-space data to figuring out EPIC programming, from attending ceilidhs to EU network workshops, it has been a pleasure working with you. In addition, the not-so-social people of IDCOM Billy, Alessandro, Heyi, Dong Dong, Mikey, Valerio have been a source of inspiration and motivation for me. I would like to thank my colleagues in WGH Dominic Job and Michael Thrippleton who are the best office mates one could ask for. I would also like to thank all the radiographers from BRIC who have helped during the data collection.

The city of Lausanne has been instrumental in my career. My love and passion for MRI started

there when I did my Masters thesis in the Cardiovascular MR group at Lausanne University Hospital (CHUV). I am greatly indebted to Dr. Ruud van Heeswijk from CVMR Lausanne without whom I wouldn't be here. He gave me the opportunity to work on Masters thesis in Cardiac MRI and my first ever publication. During my PhD, I again got a chance to visit EPFL as a part of my secondment. I would like to thank Tom Hilbert for letting me work on one of his projects on super-resolution. His assistance and guidance made the project an absolute success. I had a great time working with the ACIT team during my visit. Special thanks to Gian-Frano Piredda for helping with the data acquisition and Tobias Kober for his guidance.

I could not survive the immense pressure of PhD if it hadnot been for my friends who have been always there for me. I would like to thank my friend Hamza for always being understanding and considerate. I would like to express my gratitude to Aneeka for always being there and for putting up with me during my break downs and Amna for sharing my PhD woes. My ever-optimistic friend Mueez ud Din for always inspiring me and Shariq for always remaining upbeat despite everything. My friends Madiha and Maryam for always remembering me in their prayers.

Finally, I would like to thank my family to whom I owe a great deal. My father and mother whose unconditional love and support have brought me here. Whatever I have accomplished today is because of the trust and the faith they had in me. My mother-in-law who has encouraged me in every way possible. To my late father-in-law, whose resilience will always be a source of inspiration. I am sure he would have been very proud of my accomplishments today. I am grateful to have support from my extended family especially my aunt Sobia who is more than a friend and my childhood friend Alina for always being there for me. I am grateful to my sister Hafsah for taking care of everything so that I can just concentrate on my work and Rabiba for always listening to my endless rants. My brother Fahad and brother-in-law Jawaad for being my strength in this journey. I owe a great deal to these amazing people in my life Aysha, Zainab and Mariam. Thank you for all the support and love you have given me. Special thanks to Imran for always having my back and for showing me the bright side of life. His support and encouragement throughout the writing of the thesis have been instrumental. I cannot thank him enough for his kindness, heartwarming care and inspiration. Finally, Thanks to the most amazing nephews and niece Arham, Arsam, Eeman and Eesaa for brightening my life with their smiles.

Contents

List of figures

List of tables

Acronyms and abbreviations

1D	One Dimensional
2D	Two Dimensional
3D	Three Dimensional
AWGN	Additive White Gaussian Noise
CPMG	Carr-Purcell-Meiboom-Gill
CS	Compressed Sensing
CSF	Cerebrospinal Fluid
DCE	Dynamic Contrast-enhanced
DL-MRI	Dictionary Learning MRI
EPI	Echo Planar Imaging
GE	Gradient Echo
GRAPPA	GeneRalized Autocalibrating Partial Parallel Acquisition
GRASE	Gradient- and Spin-Echo
GM	Gray Matter
FID	Free Induction Decay
FLASH	Fast Low Angle Shot Imaging
FOV	Field of View
LLS	Linear Least Squares
k-svd	k-means Singular Value Decomposition
MRA	Magnetic Resonance Angiography
MRI	Magnetic Resonance Imaging
NEX	Number of Excitation
NLS	Non-linear Least Squares
NMR	Nuclear Magnetic Resonance
OEF	Oxygen Extraction Fractions
OMP	Orthogonal Matching Pursuit
PDF	Probability Density Function
PI	Parallel Imaging
qMRI	Quantitative MRI

RARE	Rapid Acquisition with Relaxation Enhancement
RF	Radiofrequency
RSS	Root Sum of Squares
SAKE	Simultaneous Autocalibrating and k-space Estimation
SAR	Specific Absorption Rate
SE	Spin Echo
SENSE	SENSitivity Encoding
SMASH	Simultaneous Acquisition of Spatial Harmonics
SNR	signal-to-noise ratio
SRR	Super-resolution reconstruction
LORAKS	Low-rank Modeling of Local k-space Neighborhoods
ALOHA	Annihilating Filter based Low-rank Hankel Matrix Approach
SD	Standard Deviation
TE	Echo Time
TR	Repetition Time
WM	White Matter

Chapter 1
Introduction

1.1 Project Motivation and Scope

Magnetic resonance imaging (MRI) is a non-invasive imaging modality based on the concept of nuclear magnetic resonance (NMR). Compared to other imaging modalities, MRI has several unique advantages, which make it preferable in many clinical applications. More importantly, MRI offers high-resolution and excellent soft tissue contrast without employing ionizing radiation.

MRI also provides cross sectional images with arbitrary orientation as well as true three dimensional images. Unlike other modalities, MRI is sensitive to a wide range of contrast mechanisms. These allow assessment of both morphology and physiology. In addition, these mechanisms also give access to parameters like flow, diffusion, perfusion, blood oxygenation, etc.

A major limitation of MRI is that the data acquisition is relatively slow. Long scan time is undesirable because of patient discomfort. In addition, it limits the clinical workflow and can seriously degrade the image quality during the data acquisition, for instance, caused by motion or flow. Furthermore, it limits the capability to temporally resolve dynamic processes such as cardiac [4] or abdominal imaging [5].

Since MRI was first introduced in the early 1970s, imaging speed has been improved dramatically. This has mainly been achieved by improvements in hardware and pulse sequence design to achieve faster data acquisition [6]. Modern MR scanners are already operating at a point where further improvement in data acquisition speed is limited by physical and physiological limitations. However, in many clinical applications imaging speed is still a limiting factor. An improvement in imaging speed might significantly improve the quality and accuracy of clinical diagnosis.

Further improvements in imaging speed can be achieved by reducing the amount of data required to perform image reconstruction without degrading image quality. Examples of this strategy include partial Fourier reconstruction [7] and Parallel Imaging (PI) [8, 9]. Partial

Fourier reconstruction algorithms exploit the redundancy in MR data sets so that a fraction of data is calculated during image reconstruction rather than acquired. The PI approach exploits the fact that the collected signals from coils with different spatial sensitivities carry distinct information about spatial localization. This redundancy in the data complements the conventional spatial encoding and allows skipping acquisition of some k-space points [10].

In 2006, a new sampling theory Compressed Sensing (CS) [11, 12] emerged, suggesting that signal reconstruction from a reduced amount of data can be achieved by exploiting signal sparsity. The main idea of compressed sensing is to acquire data efficiently, such that the number of measurements is directly proportional to the signal's information content. In terms of MR imaging this implies that if an MR image is compressible, which is true to some degree for all MR images, data acquisition can be performed in a way that image compression is performed already within the acquisition process. In compressed sensing, the data are acquired as a small set of incoherent measurements [13]. The image is then obtained by applying a nonlinear sparsity promoting reconstruction. The ability to reconstruct images from a reduced amount of data consequently accelerating the acquisition has attracted a lot of interest in the MR community, leading to active research in this area. Since 2006, the body of literature concerning fast MRI acquisitions and its application to a multitude of different clinical MR applications has increased significantly (Figure 7.1).

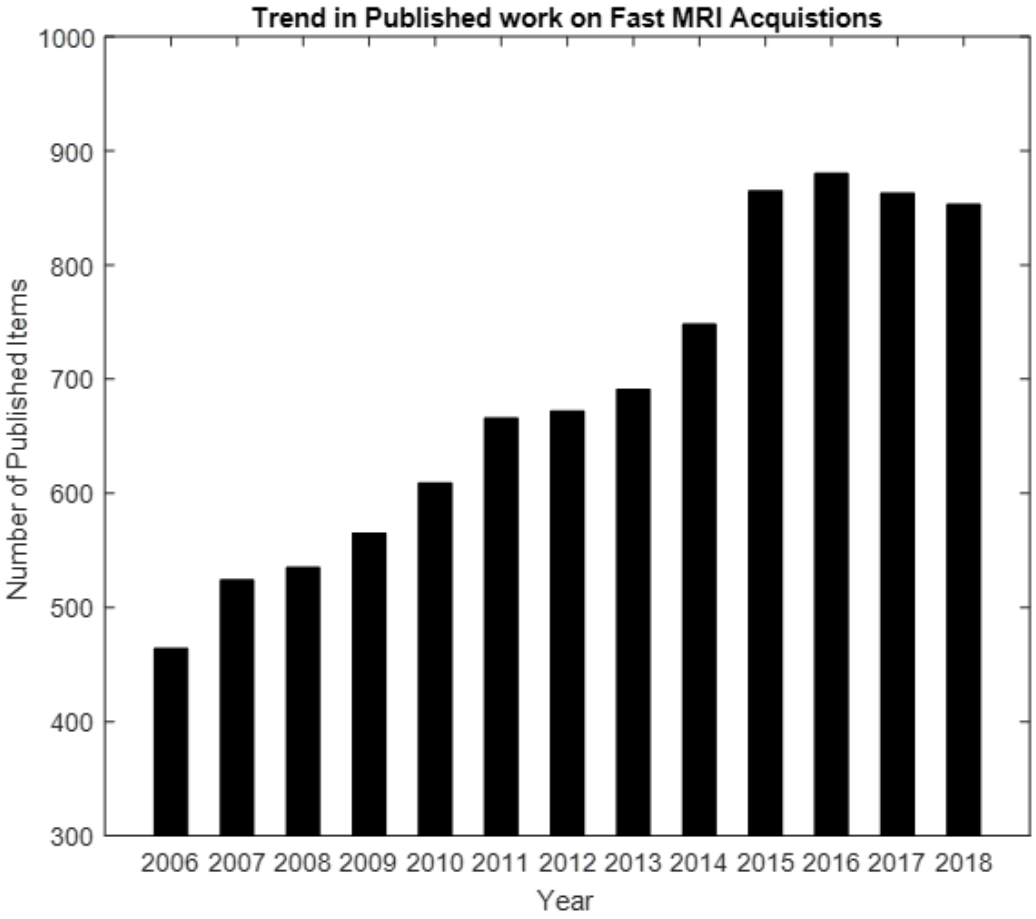

Figure 1.1: *Graph showing the increase in the number of published literature since 2006. The data was searched using the Web of Science database wth the search terms: fast MRI, accelerated MRI, Parallel Imaging, Compressed sensing MRI). The published literature includes journal articles, proceedings, book chapters and meeting abstracts*

Conventional MRI images are qualitative in nature, meaning that the contrast is mostly affected by tissue properties, but still depends on many other hardware-related and physiological effects, preventing direct comparison across patients and scans. These non-standardized images limit the ability to run longitudinal studies hence requiring new techniques that are unaffected by the experimental conditions. However, quantitative MRI (qMRI) aims to directly measure tissue properties, ideally independently from the experimental conditions. In qMRI, tissue properties are expressed as quantitative values with physical units, analogous to the measurement of systolic and diastolic blood pressure, expressed in mmHg. This technique spatially maps the

measured tissue properties resulting in an image called a quantitative map. This facilitates comparisons either within one patient at multiple time points to extract a trend of tissue alteration (intra-subject), or between a tissue property of a patient and a normative range derived from a healthy cohort to detect abnormal values (intersubject).

Although quantitative measures have proven to be a good biomarker for disease in the very early days of NMR [14], it has not been established in a clinical routine yet, partly because qMRI often requires even longer acquisition times than conventional MRI. An entire field of MRI research has been devoted to overcome these limitations, with the final goal to move MRI from a qualitative to a standardized quantitative examination. One key step towards reaching this goal is to reduce the acquisition time while retaining or improving the accuracy and precision of the estimated quantitative values.

To achieve sufficient signal-to-noise ratio (SNR) within a feasible acquisition time, quantitative MR images are typically acquired with a low spatial resolution. This low spatial resolution, however, leads to large partial volume effects, i.e. voxels will contain a mixture of different tissue types and thus different signals. Moreover, low spatial resolution makes it impossible to detect small structures. With this respect, a high-resolution quantitative map is highly desirable for visualizing small structures allowing early and accurate diagnosis. However, due to time constraints and hardware limitations, achieving high-resolution is not always feasible. The trade-off between SNR, spatial resolution and acquisition time is shown in Figure 1.2. One solution to this challenge is super-resolution (SR) reconstruction [15], in which a high-resolution image is estimated from a set of acquired low-resolution images. These low-resolution images each contain different information of the imaged object. In principle, the improvement in the resolution is governed by the number of low-resolution images but the increase in the overall scan time precludes this. Employing accelerated methods can mitigate the longer scan time and make the approach much more feasible for clinical applications.

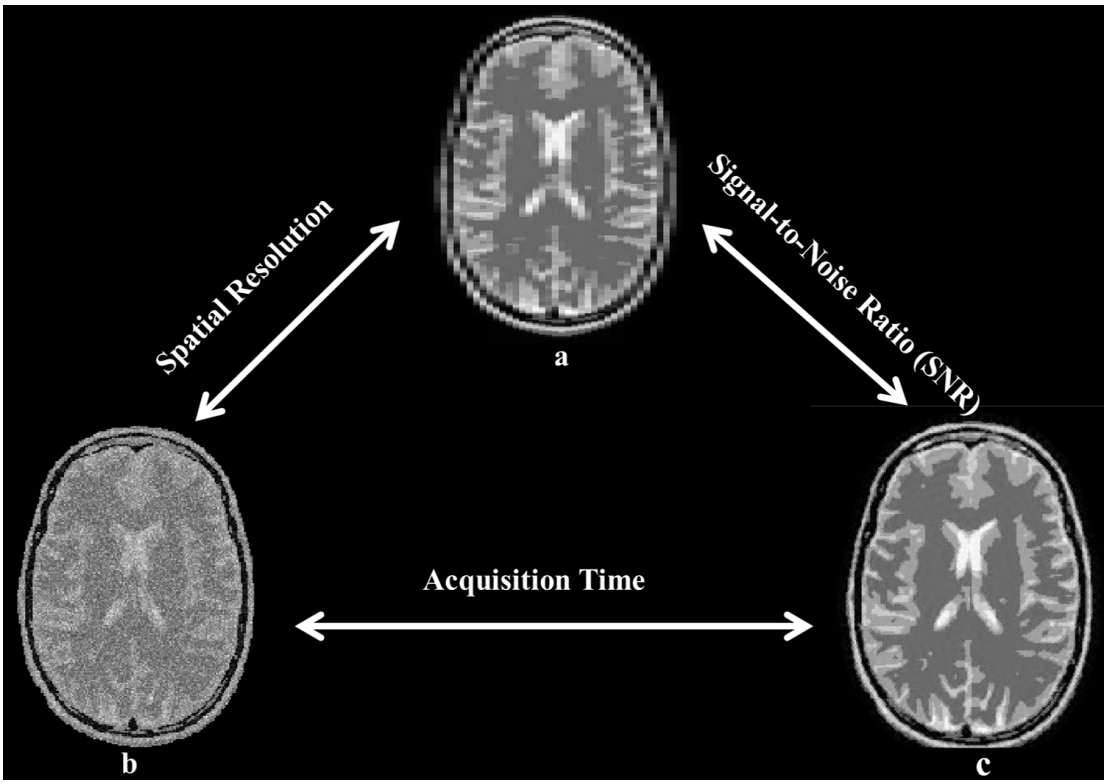

Figure 1.2: *Trade-off between spatial resolution, SNR and acquisition time is shown. Increasing SNR (b to c) by increasing the Number of Excitation (NEX, Averages) will directly affect the length of scan time. To increase the SNR (b to a) by acquiring thick slices or to increase the voxel size will reduce the spatial resolution. This will increase the SNR with no change to the length of scan time. Increasing the resolution from (a to c) decrease the signal intensity within each voxel hence affecting the overall SNR.*

1.2 Aim and structure of the thesis

The goal of this dissertation is to develop and optimize image acquisition and reconstruction methods to help obtain quantitative image information faster than conventional imaging techniques.

Chapter 2 provides a brief introduction to conventional MR imaging. It introduces the principles of signal formation, data acquisition, and image reconstruction in MRI, necessary for understanding the MR part of the thesis. Also, it gives brief overview of various accelerated

MRI methods necessary to understand most of the work done in the thesis.

Chapter 3 describes the proof-of-concept study that implemented model-based reconstruction with PI. The problems identified in this work will be addressed in the next chapter.

Chapter 4 introduces a method that aims to explore coherent information from PI in estimating parameters. The proposed approach has better accuracy over the conventional magnitude-only method. The method was applied to accelerate T_2^* mapping. It additionally provides valuable information about magnetic field inhomogeneity.

Chapter 5 explains the method to acquire high-resolution T_2 mapping by the development of a model-based super-resolution reconstruction. This work was done in collaboration with ACIT, Siemens Healthineers Lausanne as part of a SpaRTaN secondment. The proposed method enables the reconstruction of ($1mm^3$) isotropic relaxation maps with ten times faster acquisition.

Finally, in **Chapter 6**, the thesis is concluded and a future outlook for the introduced methods is discussed.

1.2.1 Project Output

- **Journal Articles**

  1. Improved Accuracy of Accelerated 3D T_2^* Mapping with Coherent Parallel Maximum Likelihood Estimation.

     Wajiha Bano, Mohammad Golbabaee, Arnold JV Benjamin, Ian Marshall and Mike Davies.

     Magnetic Resonance Imaging [Under revision]

  2. Model-Based Super-Resolution Reconstruction of T_2 Maps.

     Wajiha Bano, Gian Franco Piredda, Mike Davies, Ian Marshall, Mohammad Golbabaee, Tobias Kober, Jean-Philippe Thiran and Tom Hilbert.

     Magnetic Resonance in Medicine [Accepted: https://doi.org/10.1002/mrm.27981]

- **Conference Proceedings**

  1. Accelerating T_2^* Mapping with Maximum Likelihood Estimation (MLE) and Parallel Imaging (PI)

     Wajiha Bano , Arnold Julian Vinoj Benjamin , Ian Marshall and Mike Davies

Proceedings of ISMRM 25th Annual Scientific Meeting Exhibition. 22nd-27th April 2017. Honolulu, Hawaii.

2. Improved Accuracy of Accelerated 3D T_2^* Mapping with Coherent Parallel Maximum Likelihood Estimation.

   Wajiha Bano , Mohammad Golbabaee, Arnold Julian Vinoj Benjamin , Ian Marshall and Mike Davies.

   Joint Annual Meeting ISMRM-ESMRMB 2018, 16-21 June 2018, Paris France.

3. High-resolution Isotropic Whole Brain T_2 Mapping with Model-based Super-resolution Reconstruction.*

   Wajiha Bano, Gian Franco Piredda, Mike Davies, Ian Marshall, Mohammad Golbabaee, Tobias Kober, Jean-Philippe Thiran and Tom Hilbert.

   ISMRM 27th Annual Meeting Exhibition, 11-16 May 2019, Montreal, Canada.

   * Awarded ISMRM Merit Award (Magna Cum Laude).

Chapter 2
Background

2.1 Nuclear Magnetic Resonance

All atomic nuclei with an odd number of protons or neutrons possess an intrinsic spin angular momentum $\boldsymbol{J}$:

$$\boldsymbol{J} = \hbar\, \boldsymbol{I} \|\boldsymbol{J}\| = \hbar\sqrt{I(I+1)} \tag{2.1}$$

with $\hbar$ the reduced Planck's constant (1.05 x 10^{-34} J s), $\boldsymbol{I}$ the intrinsic spin (dimensionless) and I the intrinsic quantum number. This spin angular momentum can be considered as an outcome of the rotational or spinning motion of the nucleus about its own axis. Therefore, nuclei that have a spin angular momentum are often referred to as nuclear spins. Because the nucleus is a charged particle, this intrinsic angular momentum $\boldsymbol{J}$ is proportionally coupled with a magnetic dipole moment μ:

$$\mu = \gamma \boldsymbol{J}, \tag{2.2}$$

with γ the nucleus-dependent gyromagnetic ratio. When an external magnetic field $\mathbf{B}_0$ is applied, the magnetic moment μ will precess around this magnetic field with an angular frequency known as the Larmor frequency:

$$\omega_L = \gamma \mathbf{B}_0. \tag{2.3}$$

All nuclei for which the spin quantum I is non-zero, exhibit the property of magnetic resonance. ^{1}1H, ^{13}C, ^{19}F, ^{23}Na and ^{31}P are some of these nuclei that can be studied with NMR [16–18]. The most common nucleus considered in clinical MRI exams and the one used in this work, is the hydrogen proton (^{1}H). This proton has a natural abundance in the body in the form of H_2O water molecules. For ^{1}H, the gyromagnetic ratio is 2.675 x 10^{8} rad/s/T, and its spin quantum number $I = 1/2$.

When nuclei are placed in an externally applied static magnetic field $\mathbf{B}_0$, the orientation of their spin angular momentum, and hence their magnetic moment, will no longer be arbitrary. In a

magnetic field, the nuclear magnetic moment can only have $2I + 1$ orientations. Hence, the magnetic moment of a ^{1}H nucleus has two possible states i.e. $+\frac{1}{2}\gamma\hbar$ and $-\frac{1}{2}\gamma\hbar$. In an external applied static magnetic field $\mathbf{B}_0$, the nuclear magnetic dipole moment has a potential energy E [19]. For the hydrogen proton, there are two energy levels:

$$E = -\mu.B_0 = \begin{cases} +1/2\gamma\hbar\mathbf{B}_0 & \text{spin down} \\ -1/2\gamma\hbar\mathbf{B}_0 & \text{spin up} \end{cases} \tag{2.4}$$

This splitting of energy levels is called Zeeman-splitting. The higher energy level is referred to as the 'spin down' (anti-parallel with $\mathbf{B}_0$) and the lower energy level as 'spin up' (parallel with $\mathbf{B}_0$). Transitions between these two energy levels are possible by absorption or emission of a photon with energy $\Delta E = \gamma\hbar\mathbf{B}_0$. The energy of these transition photons is proportional to their frequency, $\omega_L = \gamma\mathbf{B}_0$, which is called the Larmor frequency. In practice, matter consists of a large group of similar nuclei. When an ensemble of nuclei is subjected to an external magnetic field $\mathbf{B}_0$, the occupation of the energy states (Eq. 2.4), proceeds in accordance with the Boltzmann statics. The spin up state (lower energy) has a higher prevalence than the spin-down state (higher energy):

$$\frac{N_\uparrow}{N_\downarrow} = \exp(\frac{\Delta E}{\kappa_B T}) > 1 \tag{2.5}$$

with κ_B the Boltzmann constant (1.380 x 10^{-23} mkg^2/s^2/K), T the absolute temperature, $N_\uparrow$ and $N_\downarrow$ the number of spins in spin-up and spin-down state respectively. Although the difference in occupation of the states (10^{-5}) is extremely small at normal body temperature in a magnetic field of clinical strength (3T), the population difference is significant due to the large number of ^{1}H protons [20].

2.1.1 Macroscopic Magnetization

On a macroscopic scale, the magnetic dipoles can be grouped in spin ensembles, containing a large population of spins within a small volume. In a spin ensemble, the magnetic moments add up to a macroscopic nuclear magnetic momentum M = $[M_x, M_y, M_z]$. In case of hydrogen protons, the macroscopic magnetic moment at equilibrium becomes:

$$\mathbf{M}_0 = \chi\mathbf{B}_0, \tag{2.6}$$

with χ the magnetic susceptibility which relates the macroscopic magnetization **M** with the static magnetic field B_0. Thus, when $\mathbf{B}_0$ is applied along the z-direction, at equilibrium, both transverse components of the macroscopic magnetization ($M_x(0)$ and $M_y(0)$) are zero, while the z-component will be [21]:

$$M_z(0) = N_s \frac{\gamma^2 \hbar^2 \mathbf{B}_0}{4k_B T}, \tag{2.7}$$

with N_s the number of spins in the ensemble.

When this magnetization vector **M** is placed in an external static magnetic field , it will experience a torque. If the magnetic field $\mathbf{B}_0$ is directed along the z-axis, the resulting rate with which **M** changes in time is given by [22]:

$$\frac{d\mathbf{M}}{dt} = \gamma \mathbf{M} \times \mathbf{B}_0 = [\omega_L M_y, \omega_L M_x, 0], \tag{2.8}$$

with ω_L the Larmor frequency:

$$\omega_L = \gamma \, \mathbf{B}_0. \tag{2.9}$$

From this equation, the solution for the magnetization **M** is then:

$$\begin{bmatrix} M_x(t) \\ M_y(t) \\ M_z(t) \end{bmatrix} = \begin{bmatrix} \cos(\omega_L t) & \sin(\omega_L t) & 0 \\ -\sin(\omega_L t) & \cos(\omega_L t) & 0 \\ 0 & 0 & 1 \end{bmatrix} \begin{bmatrix} M_x(0) \\ M_y(0) \\ M_z(0) \end{bmatrix} \tag{2.10}$$

These equations describe the precession of the magnetization **M** around the direction of the magnetic field (Figure 2.1) with angular frequency ω_L.

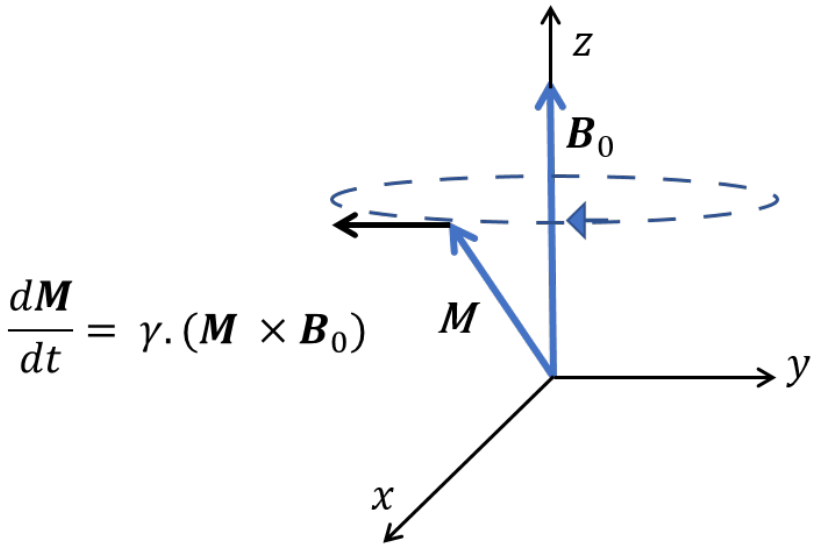

Figure 2.1: *The precession of the spin magnetization vector **M** around the external magnetic field $\boldsymbol{B}_0$ with an angular frequency ω_L*

2.1.2 RF Excitation

When the subject is placed inside an electrically conducting coil, which is perpendicular to the transverse plane, the rotating transverse component of **M** will induce a voltage in the coil [23]. The amplitude of this voltage will be proportional to the magnitude of the transverse component. In order to generate this detectable signal, the system needs to be perturbed from its equilibrium state. A second magnetic field $\mathbf{B}_1$ also called the radio frequency (RF) pulse is applied, which is perpendicular to $\mathbf{B}_0$ and oscillating at ω_L. This time varying magnetic field $\mathbf{B}_1$, which is an electromagnetic wave generated by a transmitter coil is much weaker than $\mathbf{B}_0$.

Upon applying the RF pulse, the magnetization **M** will precess simultaneously around both $\mathbf{B}_0$ at ω_L and $\mathbf{B}_1$ at $\omega_1 = \gamma\mathbf{B}_1$. In the laboratory reference frame, which is static with respect to $\mathbf{B}_0$, applying $\mathbf{B}_1$ causes the magnetization to rotate in a spiral fashion on the surface of a sphere (Figure 2.2a). Thus, applying an RF pulse during a time Δt, will flip **M** towards the transverse plane by the angle $\alpha = \gamma B_1 \Delta t$, as illustrated in Figure 2.2b. Typically, RF pulses are characterized by their flip angle. For example, a 90° RF pulse will tip the longitudinal magnetization **M** 90° into the the transverse plane.

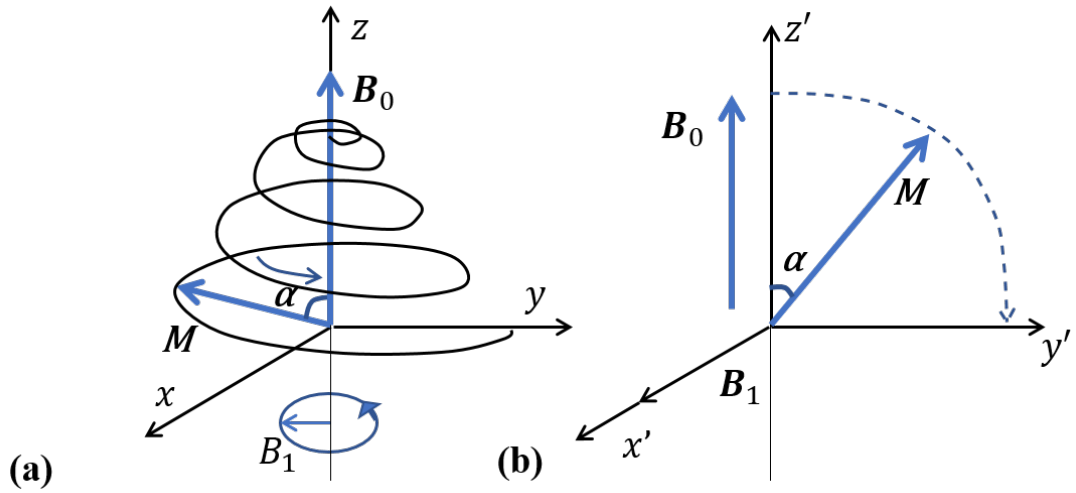

Figure 2.2: *Motion of the magnetization* ***M*** *under the influence of a static magnetic field* B_0 *and a perpendicular time-varying magnetic field* B_1 *in (a) the laboratory reference frame and (b) the rotating reference frame*

2.1.3 Relaxation

Due to the absorption of energy, the system is no longer in equilibrium. Hence, when the RF pulse is switched off, the magnetization will gradually return to its equilibrium state. The absorbed energy is dispersed by a number of processes, known as the relaxation mechanisms. These mechanisms can be grouped into two categories: longitudinal relaxation and a transverse relaxation [24]. The **longitudinal or spin-lattice relaxation** stems from the redistribution of the spin states in order to reach thermal equilibrium. The energy released during this redistribution is transferred from the spins to their surrounding environment (the lattice) by molecular vibrations. This results in a growth of M_z, characterized by the longitudinal relaxation time T_1. After a 90° RF pulse, the longitudinal magnetization can be written as a function of time:

$$M_z(t) = M_0(1 - e^{\frac{-t}{T_1}}), \tag{2.11}$$

with M_0 the magnetization along $\mathbf{B}_0$ at equilibrium (Figure 2.3).

The **transverse or spin-spin relaxation** is due to the loss in phase coherence of the spins. Random fluctuations of the local magnetic field lead to variations of the Larmor frequency

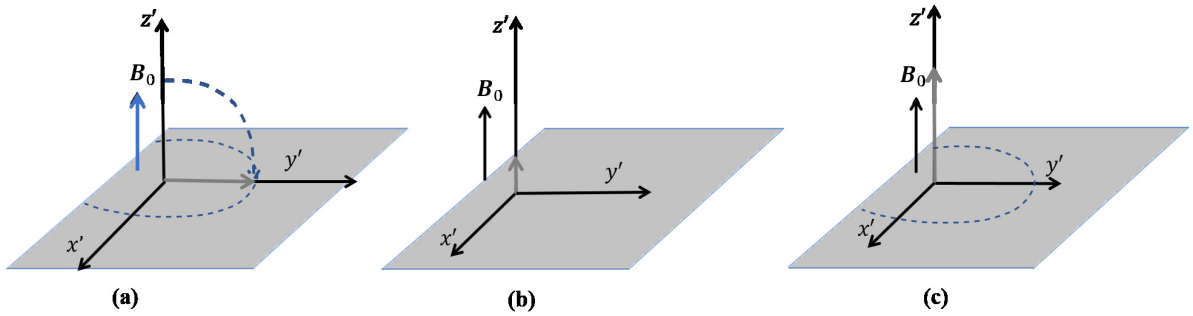

Figure 2.3: *Spin-lattice Relaxation: (a) The 90° RF pulse tips the magnetization along the transverse plane (b,c) The longitudinal magnetization relaxes and starts to grow to equilibrium.*

of the different spins. As a result, the inherently coherent spin precession will dephase (Figure 2.4). Consequently, the net magnetization of the spin ensemble, which is equal to the transversal component of the magnetization vector, will decrease. After a 90° RF pulse, the evolution of M_x and M_y over time can be written as:

$$M_x(t) = M_0 \sin(\omega_L t) e^{\frac{-t}{T_2}}, \tag{2.12}$$

$$M_y(t) = M_0 \cos(\omega_L t) e^{\frac{-t}{T_2}} \tag{2.13}$$

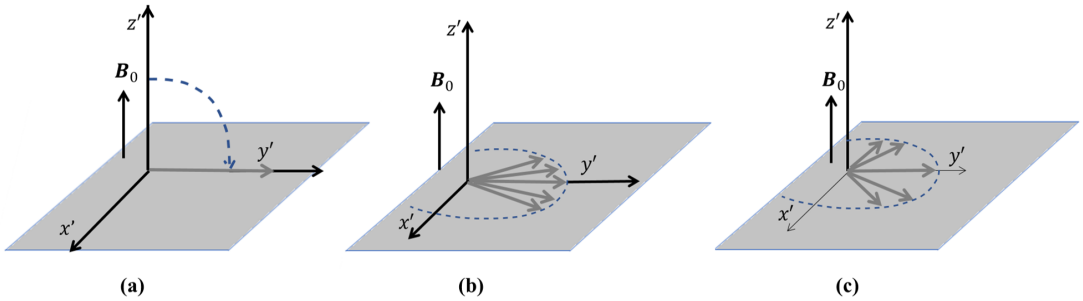

Figure 2.4: *Spin-spin relaxation: (a) The 90° RF pulse tips the magnetization along the transverse plane (b,c) The nuclear magnetic dipole moments, which constitute the magnetization* ***M****, dephase during precession (depicted in a rotating reference frame*

The total transversal component, $M_{xy} = (M_x(t), M_y(t))$, keeps precessing around the z-axis with a constant angular frequency equal to the original Larmor frequency. In heterogeneous samples, where the differences in magnetic susceptibility cause inhomogeneities in the magnetic field, the decay will be faster than T_2 [25]. The transversal relaxation due to these time

independent inhomogeneities is called T′$_2$ decay. The total relaxation time is then $\frac{1}{T_2^*} = \frac{1}{T_2} + \frac{1}{T_2'}$ and the transversal relaxation can be written as:

$$M_{xy} = M_0 e^{\frac{-t}{T_2^*}}. \tag{2.14}$$

The NMR signal is the voltage that can be measured in a coil located close to the sample. This induced voltage originates from the fluctuation of the magnetic field caused by transverse magnetization ($M_{x,y}$). It is nearly impossible to directly measure the longitudinal magnetization since the NMR signal is minimal (e.g. 1μT) in comparison to the main magnetic field (e.g. 1.5T). Therefore, only the transverse magnetization can be measured after an RF pulse was applied. The amplitude of the voltage will decay exponentially characterized by the transverse relaxation T$_2^*$. This captured signal is called the free induction decay (FID) signal [26, 27].

2.2 MR Pulse Sequence Designs

The image contrast in NMR arises from tissues generating MR signals with different intensities because of their physical properties [28]. Contrast weighting of the NMR signal is obtained by the design of pulse sequences, which consist of repetitive trains of RF pulses [29, 30]. In this section, the two most basic pulse sequences are described.

2.2.1 Gradient Echo (GE) sequence

In a gradient echo (GE) sequence (Figure 2.5), the FID signal is manipulated by a bi-polar gradient [31, 32]. The excitation pulse tilts the magnetization by α degrees. If α is 90°, the longitudinal magnetization is rotated in the transverse plane. The data is sampled during a gradient echo at time TE (TE: echo time) after the excitation pulse. This gradient echo is achieved by dephasing the spins with a negative gradient before they are rephased by an opposite gradient with opposite polarity to generate an echo. The pulse sequence is repeated a number of times to acquire the entire image. The time between two excitation pulses is called the repetition time (TR). Changing the TR, TE, and flip angles of a GE sequence influences the contrast weighting. T$_2^*$-weighted contrast can be achieved by using small flip angles and a long TE and moderate TR. By using large flip angles, a short TR and a short TE, a T$_1$-weighted signal can be acquired. Using small flip angles in combination with a long TR and a short TE generates proton density

contrast.

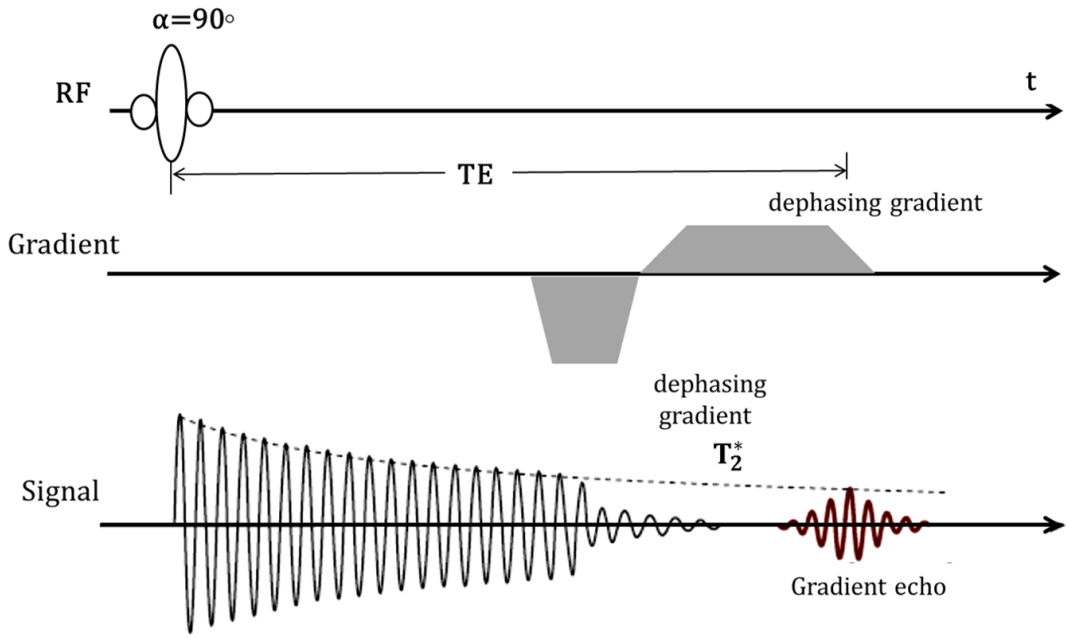

Figure 2.5: *Gradient echo sequence: The FID signal is manipulated by a bi-polar gradient, resulting in a gradient echo at TE.*

2.2.2 Spin Echo (SE) Sequence

With a spin echo (SE) sequence (Figure 2.6), pure T_2-weighted contrast can be generated [26]. When a 90° pulse rotates the magnetization into the transverse plane, the resulting FID signal quickly decays due to the strong T_2^* dephasing. If after a time TE/2 a 180° pulse is applied, the spins will be flipped and start to rephase. After another time, TE/2, a measurable echo signal is created. The spin dephasing due to static magnetic field inhomogeneities is compensated by inverting the spins with the 180° refocusing pulse. Consequently, the decay of the signal at time TE will solely originate from the T_2 relaxation. A SE sequence can also be used to generate proton density or T_1-weighted signals by using a short TE and a long or short TR, respectively [33].

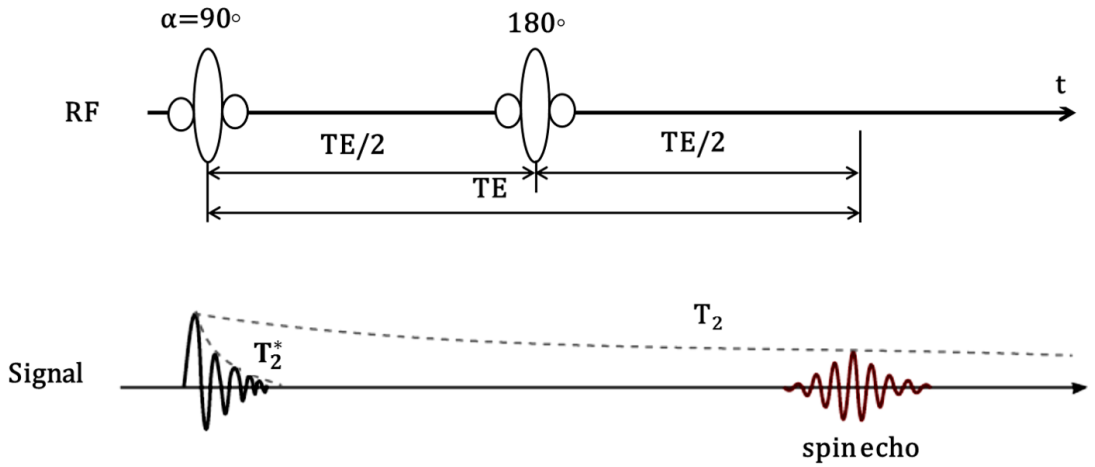

Figure 2.6: *Spin echo sequence: At TE/2 the spins are flipped by applying a 180° pulse. The rephasing spins give rise to a spin echo at time TE.*

2.3 Image formation

2.3.1 Spatial Encoding

Spatial localization of the NMR signals is essential for the formation of MR images. Hence, the subject is subdivided in voxels (volumetric pixels). The voxel-based encoding of the spatial information is achieved by superimposing spatially dependent magnetic imaging gradients $\mathbf{G} = [G_x, G_y, G_z]$ on the main magnetic field $\mathbf{B_0}$ [34]. Note that $\mathbf{G}$ is small relative to $\mathbf{B_0}$. By successive application of the gradients $\mathbf{G}$ in three orthogonal directions, the NMR signal gets encoded into a three-dimensional (3D) frequency space, from which an MRI image can be reconstructed. Although the data can be directly encoded in three dimensions, the classical approach is to encode the image in a number of 2D slices, resulting in a multi-slice image [20]. This multi-slice image is encoded in three consecutive steps:

Slice selection: During the RF pulses a slice-selective magnetic gradient field $\mathbf{G}$ is applied. For simplicity, we assume that the magnetic gradient field is applied in the z-direction: G_z (Figure 2.7). However, any slice orientation can be acquired by using a combination of the three orthogonal gradients G_x, G_y and G_z. The linear magnetic gradient causes planes orthogonal to the z-axis to have a different Larmor frequency:

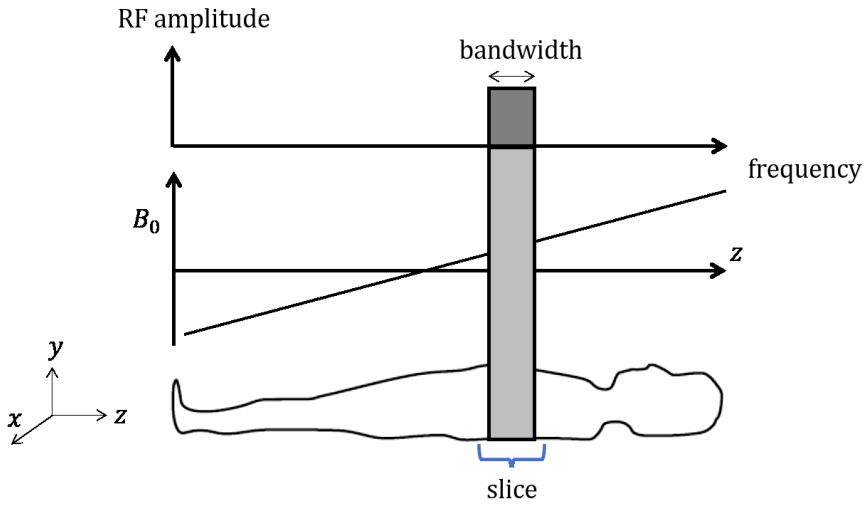

Figure 2.7: *In 2D imaging, an image slice is excited using slice selective gradients.*

$$\omega_L(z) = \gamma(B_0 + G_z Z). \tag{2.15}$$

As a result of the spatially varying Larmor frequency in the z-direction, only the magnetization vectors in a specific slice are in resonance with the RF pulses. Hence, only the magnetization vectors in that specific slice will be excited (Figure 2.7). The features of this slice can be manipulated by adjusting the gradient or RF properties. The position of the slice can be varied by changing the carrier frequency of the RF pulse while maintaining the gradient strength. A different region will now fulfill the resonant condition. The slice thickness is controlled by the bandwidth of the RF pulses and the strength of the gradient. Using a stronger gradient or a narrower RF pulse bandwidth will reduce the slice thickness Δz:

$$\Delta Z = \frac{2\pi\,(RF\,\text{bandwidth})}{\gamma G_z}. \tag{2.16}$$

In practice, the RF bandwidth is held constant, and the slice thickness is varied by adjusting the gradient strength.

Phase encoding: After the RF pulse, a time-dependent phase encoding gradient G_y is applied for a given time, τ. After time τ, a localized phase difference will be accumulated by the

magnetization vectors (Figure 2.8):

$$\phi(y) = \gamma G_y y \tau \tag{2.17}$$

Frequency encoding: A frequency encoding gradient G_x is applied during read-out. The application of this gradient results in a variation of the frequency of the spins across the x-direction (Figure 2.8):

$$\omega(x) = \omega_0 + \gamma G_x x. \tag{2.18}$$

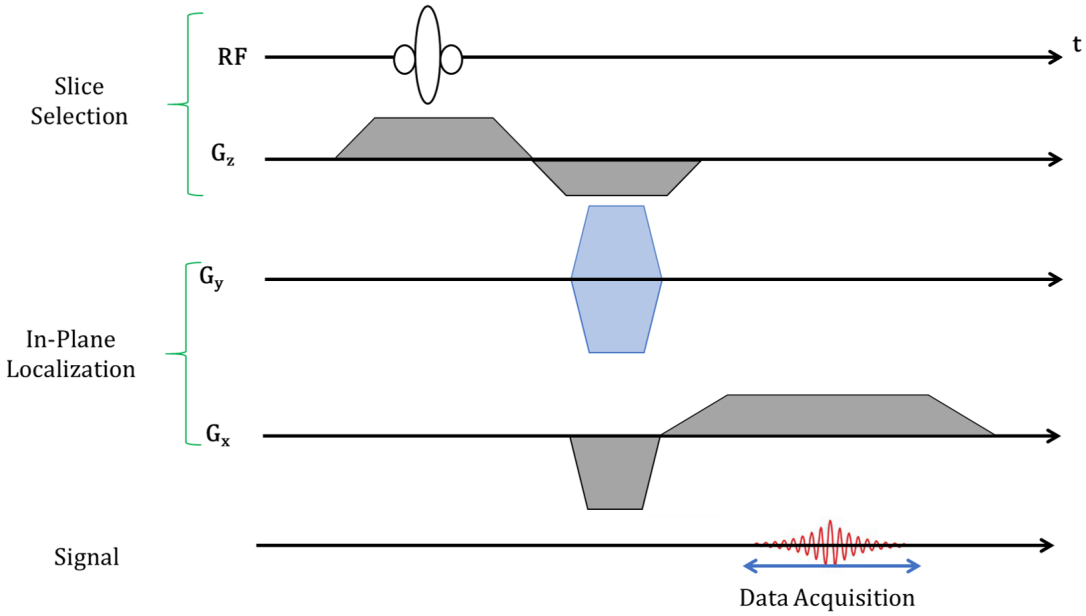

Figure 2.8: *First (top line), an RF pulse is applied simultaneously with a slice-selective gradient G_z (line 2). The interaction of RF pulse with the protons in the excited slice lead to MR signal. By combining the RF excitation with a gradient, the MR interactions are restricted to a two-dimensional plane, slab or slice. Next, in line 3, phase encoding is applied in a direction orthogonal to the slice selection. This gradient encodes the MR signal in the phase-encode direction. In line 4, the frequency-encode or readout gradient is applied in the third direction, and finally, line 5 shows the time when the MR signal is measured or acquired. Note that this is during the frequency-encode gradient but after the phase encoding.*

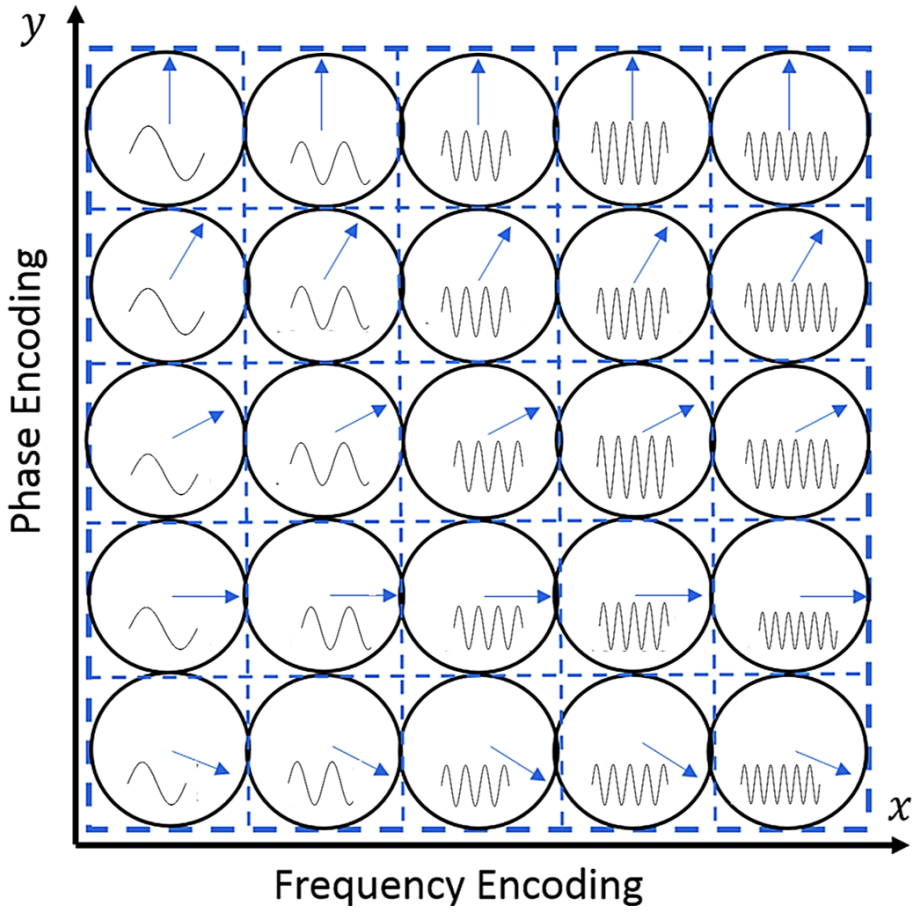

Figure 2.9: *Illustration of phase and frequency distribution after the 2D encoding. The magnetization vectors accumulate a y-position dependent phase by application of a phase encoding gradient. The frequency encoding gradient changes the resonance frequency of the magnetization vectors according to their x-position.*

The effect of phase and frequency encoding on the magnetization is shown in Figure 2.9 with each dotted box representing a voxel. When the phase-encoding gradient is turned on, we have the condition illustrated in the columns along the y-axis. As shown, the signals from the individual voxels are different in terms of their phase relationship. In other words, the signals are phase-encoded. When the frequency encoding is applied, which in this case is along the x-axis, each voxel is located in different field strength and is resonating at a frequency different from all of the others. The resonant and RF signal frequencies increase from the left to right, as shown in Figure 2.9. All of the signals are emitted at the same time and mixed as a composite echo signal. Therefore, the magnetization in each voxel is spinning at a different rate with speed

increasing from bottom to top. This happens at the time of the echo event when the signals are produced. Later, the reconstruction process will sort the individual signal components.

The signals acquired with the signal encoding described above is collected in k-space [35, 36].. Each phase-encoding gradient strength fills one row of k-space. To emphasize, each row of k-space is reserved for signals with a specific degree of phase-encoding. The degree of phase-encoding is determined by the strength and duration of the phasing gradient applied during each cycle. Therefore, the phase-encoding process must be repeated depending on the size of k-space and that is determined by the image matrix size in the phase-encoded direction.

When using a 3D sequence, an additional dimension has to be spatially encoded by phase encoding. Therefore, not only a gradient in the y-direction (G_y) but also a gradient in the z-direction (G_z) is applied for a certain amount of time Δt_z before the frequency encoding step. Using this 3D approach, the MR signal is obtained from all spins within the scanner and therefore the SNR increases in comparison to a 2D approach with only a restricted amount of spins. Nevertheless, more repetitions are required to get the entire volume, resulting in longer acquisition times. Furthermore, some sequence designs may not even be possible in 3D due to the specific absorption rate (SAR) limitations.

2.3.2 k-space and image reconstruction

The received signal is the sum of all precessing magnetization vectors. The 2D encoded signal can be written as [37]:

$$S(k_x(t), k_y(t)) = \iint \rho(x, y, z_0) e^{i2\pi(k_x(t)x + k_y(t)y)} dxdy, \tag{2.19}$$

with z_0 the position of the slice selection, $\rho(x, y, z_0)$ the density of the magnetization vectors,

$$k_x(t) = \frac{\gamma}{2\pi} \int_0^t G_x(\tau)\delta\tau \text{ and } k_y(t) = \frac{\gamma}{2\pi} \int_0^t G_y(\tau)\delta\tau, \tag{2.20}$$

with t the time between two acquired data points or 'dwell time'. equation 2.19 is easily extendable to 3D encoding. equation 2.19 describes the Fourier relationship between the image data $\rho(x, y, z_0)$ and the measured k-space data $S(k_x, k_y)$. After the k-space is sampled at sufficient frequencies (k_x, k_y), an inverse Fourier transformation $\mathcal{F}^1$ is used to compute the 2D image

from the acquired data (Figure 2.10) [38].

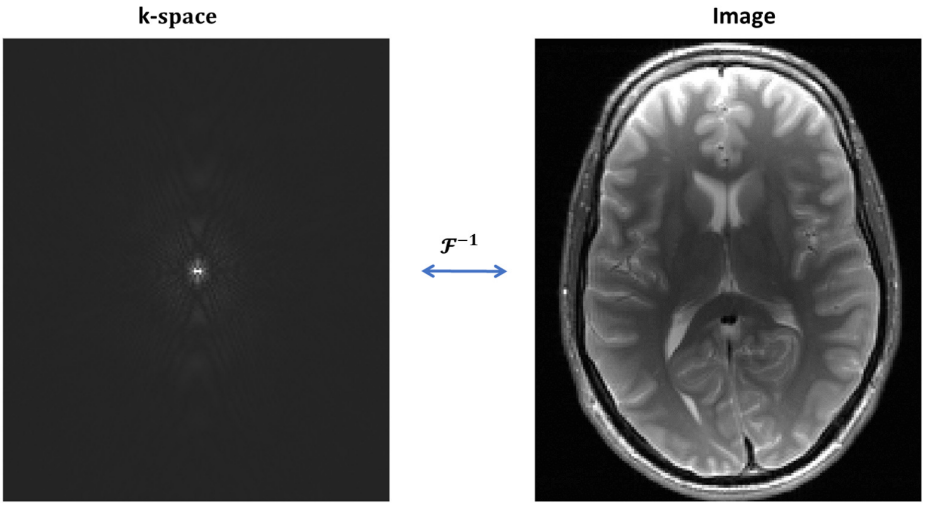

Figure 2.10: *The corresponding image can be reconstructed from the k-space data by using a discrete Fourier transform. Only the magnitude of the complex-valued k-space and image is shown.*

Many schemes to sample this k-space have been developed, each with their strengths and limitations [39, 40]. In this thesis, all the data is acquired with a Cartesian sampling scheme. The specific k-space trajectory used to fill the Cartesian grid will depend on the sequence. Sequences are either single or multi-shot. In single shot sequences the complete k-space is obtained after one RF excitation (the 90° pulse in a GE sequence or the 90°, -180° pulse combination in a SE sequence). In multi-shot sequences, only a part of k-space is obtained after one RF excitation. Hence, several separate RF excitations are needed to acquire complete k-space. Typically a 256×256 matrix image is acquired, which require 256 MR excitations which will take 256 × TR ms.

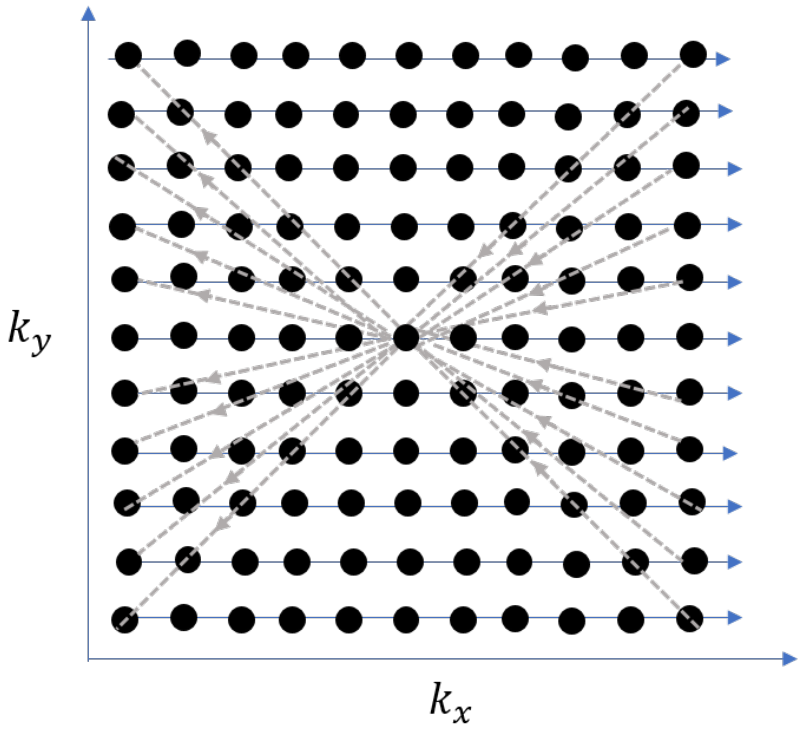

Figure 2.11: *Trajectory in k-space for the SE sequence. A slice is selected using a gradient along z-direction (G_z), the k-space is traversed using the frequency-encoding (G_x) and phase-encoding (G_y) gradients. The grey dashed lines indicate traveling in the k-space without sampling; the black dots indicate the sampled points.*

In Figure 2.11, the k-space trajectory of a spin-echo sequence is shown. Each signal is the first slice encoded along the z-axis (i.e. perpendicular to the figure) during the 90° pulse. Starting in the centre of k-space, the trajectory is moved to the lower bound of the k-space by shortly applying a negative phase-encoding gradient G_y. A frequency encoding gradient G_x moves the trajectory to the lower right corner. During 180° pulse and slice selection gradient, the trajectory moves to the upper left corner of the k-space. A positive frequency-encoding gradient G_x moves the trajectory to the right while the MR signal is being acquired. In order to fill the k-space completely, this is repeated with increasing phase-encoding gradient strength. The complete data set in k-space is reconstructed to the corresponding image data by using a discrete Fourier transform (Figure 2.10).

2.4 Image quality

In MRI, a compromise has to be made between the acquisition time and the image quality. The acquisition time is dependent on several factors such as the number of signal averages N_{SA}, the repetition time of the sequence TR, the number of phase encoding steps N_{PE} and the number of slices N_s:

$$\text{acquistion time} \propto N_{SA}\, TR \frac{N_{PE}}{N_{PE/TR}} \frac{N_s}{N_{s/TR}} \tag{2.21}$$

with $N_{PE/TR}$ the number of phase encoding lines that are acquired within one TR and N_s/TR the number of slices that are acquired within one TR. The quality of an MR image depends on:

- spatial resolution
- image contrast
- signal-to-noise ratio

So, each MR protocol and its sequence parameters have to be optimized as a function of the subject and pathology.

2.4.1 Spatial resolution

In MRI, the spatial resolution of an image is defined by its voxel size ($[\Delta x, \Delta y, \Delta z]$). The through-plane resolution is defined by the slice thickness of Δz. The in-plane resolution is defined by:

$$\begin{cases} \Delta x = \frac{\text{FOV}_x}{N_{FE}} \\ \Delta y = \frac{\text{FOV}_y}{N_{PE}} \end{cases} \tag{2.22}$$

with N_{FE} the number of frequency encoding steps, N_{PE} the number of phase encoding steps and FOV the field of view which refers to the distance over which an MR image is acquired or displayed. The matrix size is given as $N_{FE} \times N_{PE}$. The through-plane spatial resolution can be increased by decreasing the slice thickness. This can be done by using a stronger gradient or a narrower RF pulse bandwidth. Thinner slices are less susceptible to partial volume effects, i.e. many voxels will consist of a mixture of signals from different anatomical structures. In

addition, thinner slices will contain fewer spins and thus emit less signal. Moreover, decreasing the slice thickness increases the number of slices needed for full coverage of the subject, which in turn might increase the acquisition time. In practice, the voxel size is limited by the gradient strength, acquisition time and targeted SNR.

2.4.2 Spatial resolution and k-space

In Figure 2.12 the relationship between the k-space, image resolution and FOV is visualized. To avoid loss of image information, the sampling interval, i.e. the distance between two acquired k-space points (Δk_x and Δk_y) has to satisfy the Nyquist criterion. Furthermore, the k-space sampling is finite: the signal $S(k_x, k_y)$ is not sampled for $|k_x| > k_{\text{max},x}$ and $|ky| > k_{\text{max},y}$ with $k_{\text{max},x} = (N_{FE}/2)\Delta k_x$ and $k_{\text{max},y} = (N_{PE}/2)\Delta k_y$ the maximum frequency sampled in frequency and phase encoding direction, respectively. Therefore, according to the Nyquist criterion, the largest acceptable pixel size of the image is [41]:

$$\Delta x = \frac{1}{\text{FOV}_{k,x}} \text{ and } \Delta y = \frac{1}{\text{FOV}_{k,y}}, \tag{2.23}$$

with $\text{FOV}_{k,x} = 2k_{\text{max},x}$ and $\text{FOV}_{k,y} = 2k_{\text{max},y}$. Since $\text{FOV}_x = N_{FE}\Delta x$ and $\text{FOV}_y = N_{PE}\Delta y$, the FOV will thus be determined by the sampling interval:

$$\text{FOV}_{x,y} = \frac{1}{\Delta k_{x,y}} \tag{2.24}$$

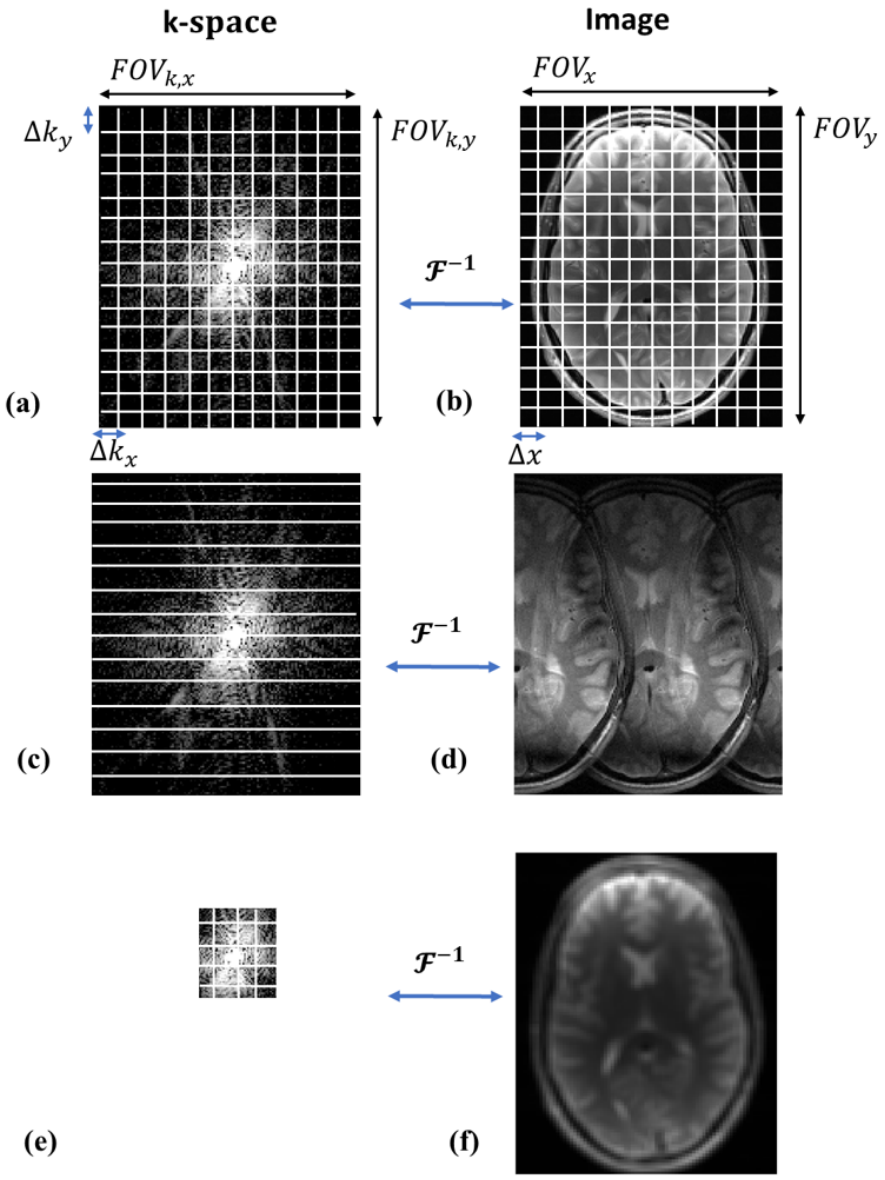

Figure 2.12: *Relationship between k-space sampling and image resolution and FOV. From a fully sampled k-space (a) the corresponding MRI image (b) can be computed. Undersampling the k-space (c) results in aliasing in the image space (d). Decreasing the maximum sampled frequency (e) decreases the spatial resolution of the corresponding image (f).*

In Figure 2.12(c-d) the inverse relationship between the spacing of the data samples $(\Delta k_{x,y})$

and the FOV is shown. When the spacing between the acquired data points is increased, the resulting image will have the same voxel size, but the FOV will be smaller. Since the Nyquist criterion is not fulfilled, edges of the brain which fall outside the smaller FOV will wrap over the sides of reconstructed images. This phenomenon is called aliasing. In modern clinical MR imaging, aliasing only occurs in the phase-encoding direction. Aliasing in the frequency-encoding direction is not usually a problem since it is eliminated by signal oversampling or bandpass filtering before reconstruction of the image [42]. Figure 2.11(e-f) visualizes the inverse relationship between voxel size and the range of sampled frequencies in k-space. The sampling rate and spacing (Δk) are kept constant, while the N_{PE} and N_{FE} are reduced, which reduces the maximum acquired frequency k_{max} as well. This manipulation of k-space results in an increase of voxel size ($\Delta x, \Delta y$). Thus, sampling high frequencies in k-space are required to achieve a high spatial resolution in MRI.

2.4.3 Signal-to-noise ratio

The acquired MRI signal intensity is corrupted by noise. This noise originates from the patient's body (human tissue can conduct electricity) and the receiver circuit of the scanner, which causes random fluctuations in the electrical current. In turn, these electrical fluctuations generate fluctuating magnetic fields which induce a noise voltage in the coil [43]. The signal intensity depends on the specific sequence and sequence parameters, as well as on the spatial resolution or voxel dimensions [44]:

$$\text{signal} \propto \Delta x \Delta y \Delta z F_{\text{sequence}}, \tag{2.25}$$

with F_{sequence} a sequence-dependent factor, which calculates the influence of the relaxation on the signal. Hence, F_{sequence} depends on the sequence parameters such as TR and TE (see section 2.2). Furthermore, the signal will also increase with increasing magnetic field strength as the excited magnetization, and thus, the observed signal is larger.

Noise and random differences in voxel values will be related to the bandwidth (BW) and sequence parameters [45]:

$$noise \propto \frac{\sqrt{BW}}{\sqrt{N_{SA} N_{PE} N_{FE}}}, \tag{2.26}$$

With N_{SA} the number of signal averages. The bandwidth corresponds to the range of frequencies captured during the read-out. The speed of k-space traversal is proportional to the

bandwidth. Hence, a larger bandwidth means that more information can be collected in a single read-out, speeding up the acquisition.

However, the thermal noise power in the coil is proportional to the bandwidth, which means that increasing the bandwidth leads to increasing the noise level [46]. On the other hand, a low bandwidth tends to cause chemical shift artefacts [45, 47]. The bandwidth can be set on the scanner and will depend on the readout gradient strength and the data sampling rate. The type and quality of coils will also have a high impact on the noise level. Combining these relationships for signal and noise, we get the SNR of an MR image [48]:

$$SNR \propto \frac{\Delta x \Delta y \Delta z F_{\text{sequence}} \sqrt{N_{SA} N_{PE} N_{FE}}}{\sqrt{\text{BW}}}, \tag{2.27}$$

Since Δx, Δy and Δz define the spatial resolution, and N_{SA}, N_{PE} and N_{FE} define the acquisition time, one can state that the SNR depends on the spatial resolution and the acquisition time [49]:

$$SNR \propto (\text{voxel size}) \sqrt{\text{acquistion time}}. \tag{2.28}$$

Thus in MRI, there is a trade-off between the spatial resolution, SNR and acquisition time of the images. After the image is acquired, the SNR of the image is typically calculated by taking the ratio of the mean and standard deviation (SD) of the signal in a homogeneous region [50]:

$$SNR = \frac{\text{mean}(S)}{\text{SD}(S)}. \tag{2.29}$$

If there is no significant enough homogeneous region in the image, instead of the standard deviation of the signal, the standard deviation of the noise (the background) is used.

2.5 Quantitative MRI

MRI is a widely used modality for the visualization of internal structure owing to its excellent contrast resolution. Generally, MRI images are qualitative in nature that are interpreted by a skilled observer. This means that the image contrast is weighted towards tissue properties and the scanner parameters such as receiver gain, RF pulsed and image scaling. Also, the contrast may depend on experimental conditions such as the B_0 homogeneity in a GRE sequence.

This is acceptable for qualitative analysis but prevents proper quantitative analysis of the tissue parameters. The quantification (or measurement) of tissue parameters with MRI would substantially increase the reproducibility of the research into biological changes in disease, and their response to potential treatments. This can change the MRI from just taking pictures that are subjective in nature to actual measurements which are meaningful. These measurements (T_1, T_2 etc.) reflect the actual biological changes happening in the tissue, e.g. increased T_2 relaxation time due to oedema as a result of myocardial infarction. In quantitative MRI (qMRI), qualitative images are replaced by quantitative parameter maps. These quantitative parameter maps appear as the weighted images but each voxel value provides tissue-specific T_1 and T_2 values rather than representing signal intensity on an arbitrary scale [24].

2.5.1 T_2^* Mapping

T_2^* relaxation refers to the decay of transverse magnetization seen with GRE sequences. It is one of the main determinants of image contrast and forms the basis for many MR applications. Most techniques for T_2^* mapping are based on multi-GE sequences, acquiring a series of gradient echoes by successive inversion of the readout gradient.

Magnetic field inhomogeneities from susceptibility differences among tissues and materials cause faster T_2^* relaxation, leading to signal intensity loss on GRE images. Magnetic field inhomogeneity can be macroscopic (intervoxel, which is constant across a voxel) or microscopic (changing within a voxel). Macroscopic inhomogeneity can be caused by deoxyhemoglobin in tiny veins, by air-tissue interfaces, or by metallic implants. Causes of microscopic inhomogeneity include paramagnetic contrast agents, blood products, or iron deposits.

T_2^*-based imaging includes making GRE sequences more sensitive to T_2^* decay by changing user-selectable parameters such as TE, flip angle, and TR in an appropriate way. T_2^* decay due to dephasing starts with the excitation and progresses with time. The longer the TE, the greater the signal loss. Hence, as TE increases, T_2^* sensitivity of the GRE sequence increases because of more dephasing. With a low flip angle, excitation longitudinal magnetization remains close to the fully relaxed state, independent of different T_1 values. Hence, a low flip angle reduces the T_1 influence, and the T_2^* differences become dominant. A long TR also reduces the T_1 effect. Therefore, GRE sequences can be made T_2^* weighted by using a low flip angle, long TE, and long TR.

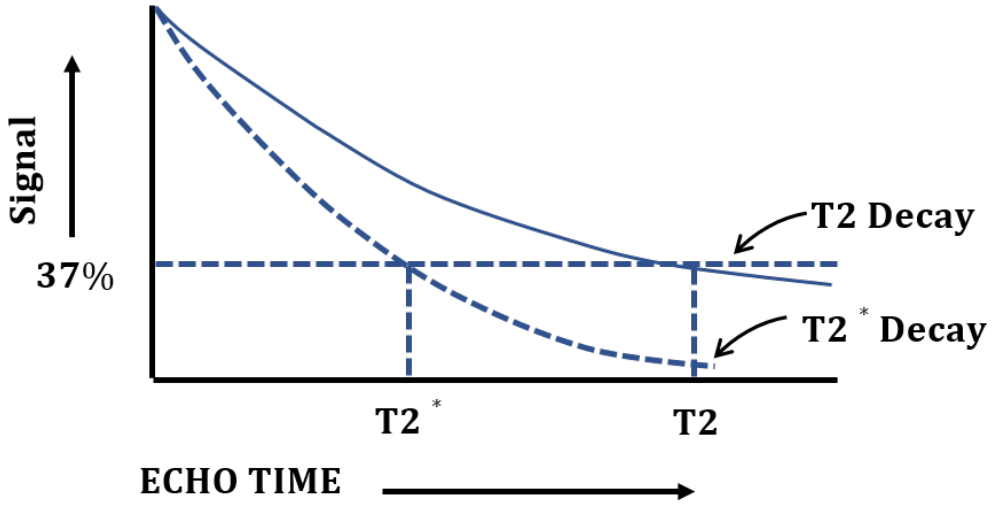

Figure 2.13: *Graph shows T_2 and T_2^* relaxation curves. T_2^* is shorter than T_2*

With these T_2^*-weighted sequences, the lesion, structures, or areas of dephasing are shown as dark areas, leading to their detection or characterization. In GRE sequences, there is no 180° refocusing pulse and these dephasing effects are not eliminated. Hence, transverse relaxation in GRE sequences (i.e, T_2^* relaxation) is a combination of "true" T_2 relaxation and relaxation caused by magnetic field inhomogeneities. T_2^* is shorter than T_2 (Figure 2.13) and their relationship is expressed in section 2.1.3.The reported values of T_2^* and T_2 in literature [51] are shown in table 2.1.

Tissue Type	**Relative Spin Density**	**T_2^* (ms)**	**T_2 (ms)**
Gray Matter	83	65	100
White Matter	71	78	80
CSF	100	2000	2200

Table 2.1: *T_2^* and T_2 values in different brain structures at 1.5T as reported in literature*

Various applications for the acquisition of T_2^*-weighted images have been described, such as the detection of haemorrhagic lesions in traumatic brain injuries [52], the assessment of vascular fragility via detection of microbleeds [53], and the investigation of neurodegeneration with brain iron accumulation [54]. Several studies employ quantitative MRI (qMRI), directly measuring local T_2 and T_2^* values. Applications comprise the investigation of tumour vascularisation [55], the measurement of the cerebral oxygen extraction fraction and the cerebral venous blood volume [56], the detection of superparamagnetic iron oxides [57], the investigation of

patients with Parkinson disease [58, 59], the measurement of the age dependence of iron accumulation in the basal ganglia [60], and the investigation of patients with amyotrophic lateral sclerosis [61].

Furthermore, simultaneous mapping of T_2 and T_2^* and derivation of $T_2^{'}$ values has been used for the measurement of brain iron contents in Parkinson patients [62], the assessment of iron concentrations and tissue metabolism in Multiple Sclerosis [63], and the investigation of deoxyhaemoglobin levels and oxygen extraction fractions (OEF) in acute stroke [64].

2.5.2 T_2 Mapping

SE is the most commonly used sequence for quantifying T_2 relaxation. As discussed in Section 2.2.2, the amplitude of a spin-echo depends on the echo time (TE) and on the tissue characteristics M_0, T_2 (see equation 2.14). Multiple images are acquired with different TEs, and a voxel-wise fitting is performed to find the best combination of T_2 and M_0. Notably, this assumes that the longitudinal magnetization fully recovers during the TR. This approach often yields very accurate T_2 values and is considered the gold standard if spectroscopic SE is not available. However, acquiring multiple SE images increases the scan time considerably. For example, to acquire a T_2 map with a SE sequence of a matrix size 256×256; with a TR of 4s and only two echo times TE. The resulting acquisition time is approximately 34 min (TR x Number of Lines x Number of TE). Acquiring two echoes also affects the accuracy of the fit and requires more TEs. Therefore 16 echoes are commonly used, which linearly scales the acquisition time to 4:32h.

To accelerate the acquisition, a Carr-Purcell-Meiboom-Gill (CPMG) [65] sequence can be used to sample all echoes within a single TR by applying multiple 180° refocusing pulses. The example above would then result in an acquisition time of 17 mins (TR x Number of Lines), which is much shorter in comparison to SE's acquisition time. This approach has become the standard for quantitative T_2 mapping but is still rarely used in clinical routine.

However, the CPMG sequence has various other limitations. The sequence requires a homogeneous B_1 field and ideal (rectangular) slice profile in order for the refocusing pulse to rephase the spins. This is important as the signal model is applied under the assumption of perfect refocusing. Since these requirements are difficult or even impossible to achieve, the acquired signal diverts from the signal-model. An additional T_1 related signal is superimposed on the

mono-exponential decay, which is called stimulated echo and causes an overestimation of T_2. Several methods were proposed to mitigate this effect, for example by ignoring the first echo [66], estimating and removing the systematic bias [67] or directly fitting the stimulated echo signal model [68–70].

Alternatively, various other sequence designs can be used to estimate T_2, e.g. by using a GRE acquisition. A T_2 magnetization preparation is used in such sequence with 180° refocusing pulse to ensure T_2 contrast. Again, this has to be repeated for various different T_2 weightings and the corresponding signal model has to be fitted to this series of images. This approach is still sensitive to B_1 inhomogeneity and is influenced by T_1 but showed good results in cardiac imaging [71]. A major advantage of the method is that it only requires a 180° pulse in the magnetization preparation but not in the actual acquisition of the image. Therefore, it can be used as a 3D sequence without exceeding SAR limitations.

T_2 mapping has been used in cardiac [72, 73] and muscloskletal [74–76] applications. In addition, various studies have demonstrated the importance of T_2 mapping to study various neurological conditions such as stroke [64], epilepsy [77], multiple sclerosis , tumor detection [78] and Alzheimer's disease [79] .

2.6 Accelerated Quantitative MRI

As described before, image acquisition in MRI requires acquiring multiple lines of k-space that subsequently result in long scan times. This limits the application of qMRI in clinical settings. Various attempts have been made to address the inherent slow acquisition of MRI. In the following sections, some of these approaches are presented.

2.6.1 k-space and Sequence Sampling Techniques

Throughout the history of MRI there have been innovations which have tried to overcome the limitation of the repeated repetition times, including echo planar imaging (EPI) [80], rapid acquisition with relaxation enhancement (RARE, also known as fast or turbo spin echo) [81], and fast low angle shot imaging (FLASH) and its variants [82]. Rather than the simple acquisition described above, where only one line of k-space is acquired from one gradient or spin echo per repetition time, these techniques use multiple RF pulses or gradient refocussings to generate

multiple echoes and acquire multiple lines of k-space per repetition time.

Further acceleration can be achieved by using the Gradient- and Spin-Echo (GRASE) technique, which generates multiple gradient echoes on top of a spin echo [83]. The first portion consists of typical spin-echo excitation steps and is followed by both frequency- and phase-encoding gradients to produce multiple gradients and spin echoes. Subsequent refocusing pulses with accompanying gradients can be applied until k-space is filled. Moreover, the addition of gradient echoes may lead to unwanted sensitivity to magnetic field inhomogeneity (B_0) and susceptibility differences (T_2^*). These techniques accelerate the acquisition of the full k-space coverage demanded by the Nyquist criterion and can therefore still be regarded as accelerated fully sampled acquisitions.

Interleaved slice sampling is a widely used acceleration technique in 2D imaging. Sequence designs with a short acquisition but long TR (e.g. spin-echo) have a long unused delay until another excitation is performed. Interleaved slice sampling exploits this down-time and performs the data acquisition of other slices. Finally, prior knowledge can be used to reconstruct images from reduced k-space data. Probably the simplest of these methods is partial Fourier imaging [84, 85]. In partial Fourier imaging, it is assumed that the image phase varies slowly over the FOV. Data acquisition is performed asymmetrically, covering a little bit more than half of k-space. The image phase is estimated from a small part of fully sampled data around the k-space origin, and the conjugate symmetry of the Fourier transform is used to estimate a real-valued image.

2.6.2 Parallel Imaging (PI)

The basic idea of PI is to employ several independent receiver coil elements in parallel to reduce the number of phase-encoding steps. Thus, a certain amount of the spatial encoding originally achieved by the phase-encoding gradients is now substituted by evaluating data from several coil elements with spatially different coil sensitivity profiles. Thus it is possible to compensate for the missing k-space data by exploiting this additional spatial information from the coil sensitivity profiles. Related methods are usually categorized to be either proposed in image space or in k-space. While the general methodology was already published in the late 1980s [10, 86] the first clinical applications were established in 1999 as the SENSE (sensitivity encoding) [8] and the SMASH (simultaneous acquisition of spatial harmonics) [87] algorithm, respectively. Since then, both methods have been further improved to utilize the data of undersampled k-

space even more efficiently [9, 88, 89].

2.6.2.1 SENSE

For discrete Cartesian sampling, given the unknown image x and the measured signal y, the image reconstruction can be written as a linear operation:

$$y = Ax. \tag{2.30}$$

For fully sampled k-space, the matrix A is square and has full rank. If known prior to reconstruction, the matrix A can be extended by a matrix S containing the sensitivity-weighting coefficients from all available receiver coils. Given the multiple coil measurements $y = [y_1, ..., y_C]$, B the undersampling mask and F the Fourier transform, equation 2.30 takes the form:

$$y_c = BFS_c x \tag{2.31}$$

where

$$A = [BFS_1; ...; BFS_C] \tag{2.32}$$

With multichannel coils, the number of rows in A now exceeds the number of columns. Hence the system of equations becomes over-determined, and a direct inversion of A is not feasible. However, a good solution in the least-squares sense can often be achieved by the Moore-Penrose pseudoinverse:

$$\hat{x} = \hat{A}y \quad \hat{A} = (A^H A)^{-1} A^H \tag{2.33}$$

where H is the adjoint, i.e. the transposed matrix with each entry replaced by its complex conjugate. If the sensitivities of the individual elements contribute a sufficient number of linearly independent row vectors in A, the additional information can be exploited for undersampling. This is the basic strategy behind SENSE [8]. With ideal coil configuration, the method allows for data reduction or acceleration factors (R) up to the number of coil elements. In practice, however, the achievable acceleration is usually much smaller due to linear dependencies of the profiles or the independence of each coil elements. If the coil sensitivities from receiver coils are highly correlated, the unfolding of the aliased pixels will be hard, which reduces the SNR of the SENSE reconstruction.

2.6.2.2 Estimation of coil sensitivity profiles

PI methods exploit spatially varying coil sensitivity profiles, therefore, requiring knowledge of the underlying profiles S. Unfortunately, the sensitivities are not only dependent on the coil design, but also the dielectric properties of the object within the FOV. As these conditions may change between different experiments, the coefficients have to be recalibrated for every patient and setup. Good estimates of S can be acquired in a preparation scan, where the reconstructed images of the array coil are divided by the image of the whole-body volume coil [86]. However, the inherent additional scan time spoils the original effort of acceleration. Also, patient movements and body fluids may spoil the accuracy of the coil profiles with respect to subsequent scans. To avoid these limitations, most current PI implementations employ so-called autocalibration methods. Hereby, a small region in the center of k-space is sampled at full Nyquist rate (Figure 2.14) [90, 91]. The lines can subsequently be filtered, and inversely Fourier transformed to create low resolution images for every coil element. Depending on the implementation, coil profiles may subsequently be taken from low-order polynomials, fitted to the individual images. A variety of other estimation methods have been proposed [92, 93], including methods that jointly estimate the sensitivity maps and the image [94, 95].

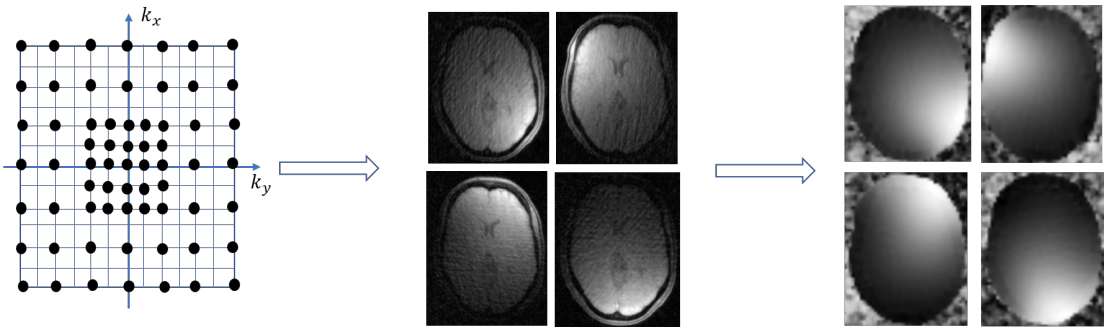

Figure 2.14: *Auto-calibration: From a fully sampled centre, low-resolution images can be calculated. Division by a Root sum of squares (RSS) image and post-processing yields approximate coil sensitivities.*

2.6.2.3 GRAPPA

Generalized Autocalibrating Partially Parallel Acquisition (GRAPPA) assumes that a missing k-space sample (target sample) can be interpolated by a linear combination of its neighbours and its representation in all receiver coils (source samples) as is illustrated in Figure 2.15. This

prior knowledge is used to retrieve missing k-space lines by first training this linear dependency (autocalibration), and second, use the previously learned dependencies to synthesize missing k-space points. Here, the weights are not determined by a fit of the coil sensitivities, but instead by a direct fit of some measured signal lines against one [90] or more [89] reference lines also known as an autocalibration signal (ACS). Because inaccurate calibration might lead to cancellation artifacts, coil-by-coil reconstruction [96] was introduced. Here, the missing data points are recovered for each channel and then combined with the actually measured data. The completed data set can then be reconstructed by applying an inverse Fourier transform for each channel, followed by a root sum of squares (RSS) reconstruction. Thus, no signal energy is lost in a linear combination of the channels. All these advancements were finally integrated into the GRAPPA algorithm [9], where the combination of coil-by-coil reconstruction with a variable density sampling scheme has the additional advantage, that the reference lines can be directly incorporated into the reconstruction, thus increasing the SNR.

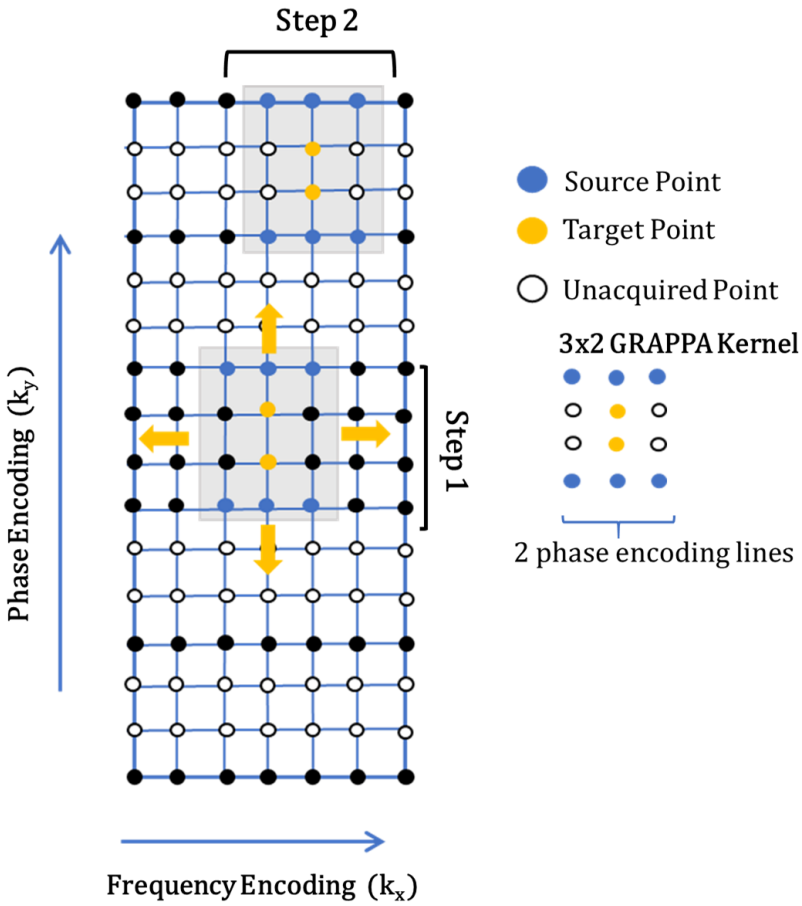

Figure 2.15: *GRAPPA: Undersampled k-space data are collected from each coil. Step 1: For GRAPPA calibration, several additional lines are collected at the center of k-space (the ACS region) to estimate the GRAPPA weights. The kernel (outlined by the gray box) consisting of some source points (blue circles) and target points (yellow circles) defines the neighbourhood of k-space points that will be used for the GRAPPA reconstruction. Although not shown in the diagram, the kernel uses source points from all coils to synthesize target points in one coil. Step 2: The GRAPPA kernel is applied to fill in the missing k-space data from each coil to produce fully sampled single-coil data. All missing data from all coils are reconstructed from neighbouring k-space data. Figure adapted from Hamilton et al. [1].*

Further developments include the extension to 2D acceleration in 3D imaging [97] and to dynamic imaging [98]. Various extensions and similar algorithms based on the k-space locality

principle have been proposed for non-Cartesian imaging. [99, 100].

2.6.2.4 Self-Consistent Parallel Imaging

Iterative self-consistent parallel imaging (SPIRiT) [101] combines SENSE and GRAPPA. Like GRAPPA, SPIRiT uses k-space kernels to recover missing information by exploiting correlations between neighboring k-space points. However, the reconstruction is framed as an inverse problem like SENSE. The calibration consistency equation is independent of the sampling pattern. The SPIRiT reconstruction is typically initialized with the zero-filled and undersampled k-space, and the optimization problem is solved iteratively. The algorithm moves toward a solution that minimizes and balances the errors between two terms: calibration consistency and data consistency

The first error term is calculated using a k-space convolution kernel or SPIRiT kernel and is called the "calibration consistency" term. Traditional GRAPPA enforces calibration consistency only between synthesized points and the acquired points in their associated neighborhoods. Whereas SPIRiT expands the notion of consistency by enforcing consistency between every point on the grid and its entire neighborhood across all coils. It is important to emphasize that the notion entire neighborhood includes all the k-space points in all coils, whether they were acquired or not. This process is visualized as convolving or sliding the SPIRiT kernel throughout k-space. An example of a kernel is shown in Figure 2.16, which includes both collected and missing k-space points. Like GRAPPA, SPIRiT requires ACS to estimate the SPIRiT kernel coefficients. The difference between SPIRiT and the traditional GRAPPA weights is that SPIRiT kernel is independent of the actual k-space sampling pattern and is the same for all k-space points.

The second term in the optimization enforces consistency with the undersampled data and is called the "data consistency" term. In other words, the reconstruction is allowed to recover missing k-space points, but it should not change the acquired data points. At the originally sampled k-space positions, the difference between the reconstructed data and acquired data should be zero [1].

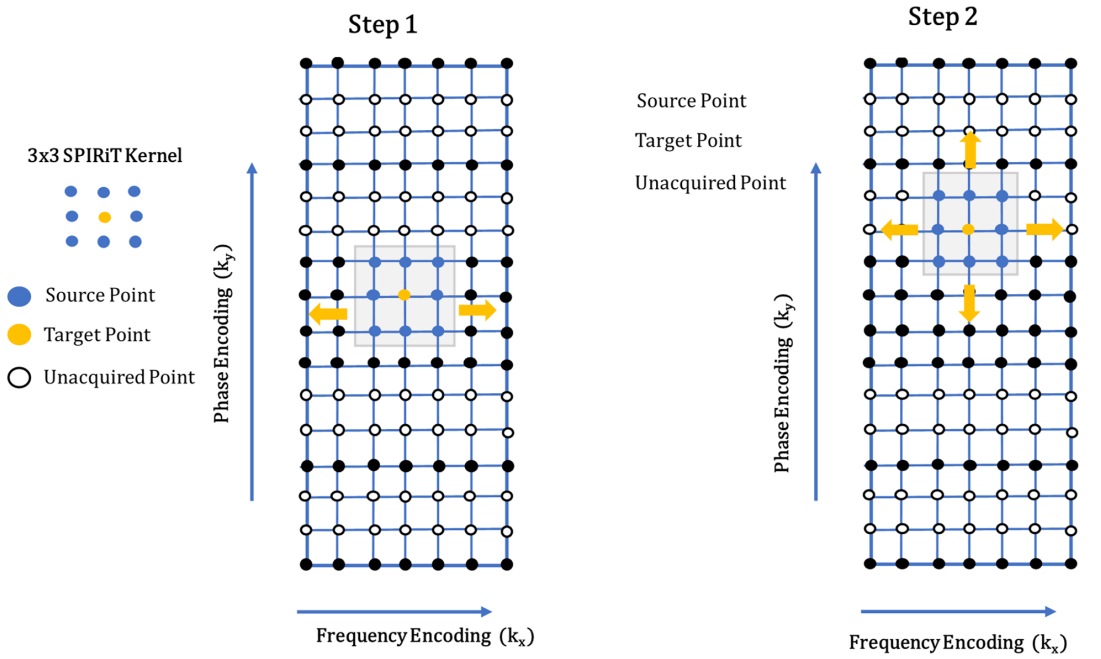

Figure 2.16: *SPIRiT:A 3×3 SPIRiT kernel (left) is defined where each target point (shown in yellow) is expressed as a linear combination of all surrounding grid points (shown in blue). Step 1: The SPIRiT kernel is calibrated using a fully-sampled region near the center of k-space. Step 2: Then, a solution is found that satisfies the SPIRiT kernel relationships and is consistent with the acquired data (Step 2).Figure adapted from Hamilton et al. [1].*

2.6.3 Compressed Sensing

Compressed sensing (CS) is an emerging area in signal processing and information theory which has recently attracted much attention. The idea behind CS is that sparse or compressible signals can be acquired in an efficient way by applying compression already in the data acquisition process. According to CS theory, sparse or compressible signals can be recovered from fewer samples than required by the Shannon-Nyquist sampling theorem [11, 12]. This is achieved by applying an appropriate sampling scheme and reconstruction that employs signal sparsity to recover the signal. Unlike PI approaches, k-space is incoherently sampled; thus, noise-like artefacts appear in the image when a direct inverse Fourier transform is performed. To remove the artefacts caused by the undersampling, iterative reconstruction is used (see section 2.6.2.1: Equation 2.30), but with the addition of regularization that enforces sparsity by

penalizing coefficients in some domain (e.g. Wavelet, finite difference) with a L_1-norm:

$$min\|\|\Psi x\|_1 s.t. \|Ax - y\|_2 \leq \epsilon \tag{2.34}$$

where Ψ is the sparsifying transform. There are a number of sparsifying transforms introduced in compressed sensing. Wavelet is one of the most commonly used transforms, which decomposes the image at different scales within three directions (vertical, horizontal, diagonal). In addition, total variation, which enforces the sparsity of the image gradients, is emerging as a popular method. The advantages of total variation include its simplicity, rotation invariance, and capability of preserving edges and providing good image quality [102, 103]. Numerous experiments have shown that total variation reconstruction is comparable to more sophisticated schemes such as wavelet and x-let reconstruction [104]. Figure 2.17 shows sparsity of MR images.

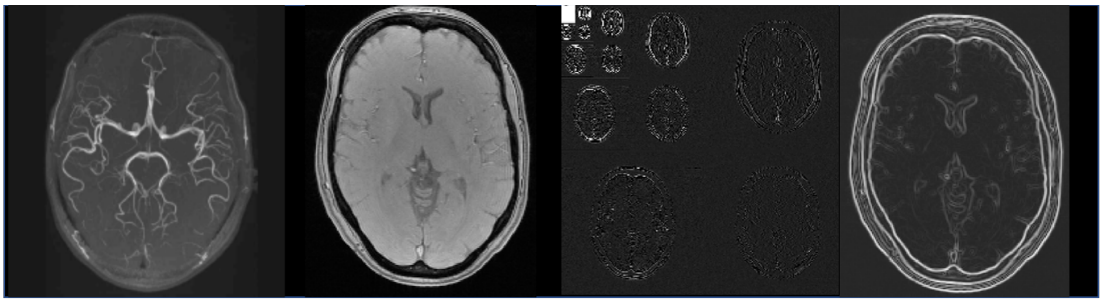

(a) MR Angiography (b) MRI Brain (c) Wavelet Domain (d)Finite Difference

Figure 2.17: *Sparsity of MR images. (a) Shows a sparse MR angiography image, where only a few pixels indicating the blood vessels are with high intensity. Some MR images are sparse in the transform domain. For example, (b) presents a brain MR image, which is sparse in the wavelet domain, as shown in (c); or finite differences representation, illustrated in (d).*

Several methods combining CS and PI have been proposed to achieve higher acceleration, for example, [105–108]. The problem to be solved can be expressed by modifying equation 2.34 to incorporate the sensitivity profiles, S, in the measurement matrix A.

One of the simplest approaches can be a SENSE type approach that explicitly utilizes the estimated coil maps to fill the missing k-space points. [109–112]. Specifically, if the coil sensitivity is known and given by the sensitivity S_c, where $c = 1, ..., C$, then the SENSE type compressed

sensing MRI problem can be formulated as:

$$\min_x \sum_c^C \|BFS_c x - y_c\|^2 + \lambda \|\Psi x\|_1 \tag{2.35}$$

where B is the undersampling mask, F is the Fourier transform, x is the image to be reconstructed and y_c is the vector of k-space data. The optimization is the standard optimization framework under sparsity constraint, so proximal optimization algorithms [13] can be used to solve this problem. Two of these methods include SPIRiT [113] that operates in k-space and ESPIRiT [108] that works in the image domain. These methods incorporate arbitrary k-space sampling with L_1-norm minimization to additionally enforce sparsity.

Blind compressed sensing approaches attempt to simultaneously reconstruct the underlying image as well as the sparsifying transform from highly undersampled measurements. Ravishankar and his colleagues pioneered two distinct approaches: synthesis dictionary learning [114] and analysis transforms learning [115]. Sparsifying transform learning is effective and efficient in applications, while also enjoying good convergence guarantees. Several important works have been proposed in this context, which attempts at designing an adaptive framework for sparsifying the MRI data. Otazo and Sodickson [116] proposed a method for adaptive compressed sensing MRI using a similar framework. The combined reconstruction and dictionary update problem was solved iteratively, where each iteration included two stages: (a) sparse recovery and (b) dictionary update. In the first stage, the size and elements of the dictionary are fixed based on a presumption, and then Orthogonal Matching Pursuit (OMP) algorithm is used for CS reconstruction. In the second stage, the dictionary is updated using k-means singular value decomposition (k-SVD) algorithm. The results of the proposed work reduced noise as compared to traditional-CS methods, thereby lowering reconstruction artefacts of the image. Ravishankar and Bresler [114] designed a novel framework of Dictionary learning MRI (DL-MRI) which can simultaneously learn a dictionary and reconstruction MR image from highly undersampled k-space data.

Dynamic MRI is a technique to acquire a sequence of temporally varying MR images such as cardiac cine, perfusion, time-resolved angiography, functional MRI, etc. In dynamic MRI, there exist significant redundancies along with the temporal directions, which can be utilized in various compressed sensing approaches. Preliminary CS dynamic MRI approaches [117, 118] were seemingly different from the classical k-t approach such as k-t (Broad-use Linear Acquisition

Speed-up Technique) BLAST/SENSE [119]. Another method is known as k-t FOCUSS by Jung et al. [109, 110] demonstrated significant improvement in the classical k-t BLAST/SENSE. More specifically, by using incoherent sampling patterns, multiple iterations and the correct weighting factor for the diagonal matrix, clear improvement was seen. This improvement originated from exploiting the sparsity into the spatio-temporal domain.

Compared to the standard compressed sensing approaches, k-space structured low- rank approaches such as SAKE [120], LORAKS [121], ALOHA [122, 123] are relatively new but have significant potential in MRI imaging. These methods all rely on the low-rank property of the Hankel matrix to reconstruct images. SAKE exploits correlation among the multi-coil, LORAKS exploits finite spatial-support or smooth phase condition, and ALOHA reformulates sparsity in the transform domain as low-rankness in Fourier domain. In the context of qMRI, the presence of parametric dimension may offer additional means for acceleration. To formulate the reconstruction problem, the parametric dimension is used as a source of a priori knowledge. Various approaches employing sparsity constraints[124], low-rank approaches [125, 126] and joint sparsity [127, 128] have been studied to accelerate parametric mapping.

Since CS MRI allows significant acceleration of MR acquisition, it has been extensively applied for various clinical applications such as fast cardiac MRI [4, 129], whole heart MRI [112], dynamic contrast-enhanced (DCE)-MRI [32], diffusion MRI [130], spectroscopic imaging, etc., that usually require significant acquisition time using standard methods.

2.6.4 Model-based Reconstruction

The framework of PI methods demonstrates how data acquisition can be accelerated by using the combined data of different receivers to reconstruct a single aliase-free image from undersampled multichannel data. However, the general idea of exploiting complementary sources of image information is not restricted to sensitivity profiles. In recent years, new techniques have evolved that make use of several different kinds of prior information about data dependencies or image properties. As discussed before, CS allows for data reduction by considering the reconstructed images to be sparse in suitably chosen domains. Most recently, such sparsity transforms were extended to the T_1 and T_2 parameter space and used for dictionary-based reconstructions of corresponding maps [131] employing the OMP. Another strategy is to directly describe sequence specific data-dependencies in a suitable model and then try to estimate the correct model parameters from a set of (potentially undersampled) k-space samples [132].

In a typical qMRI experiment, the tissue parameters of interest (θ) are obtained by acquiring several images at different values of the acquisition parameters, e.g. echo time t_n with $n = 1, ..., N$ and performing a pixel-wise fit to the signal model $f(\theta, t_n)$. Thus, in addition to spatial encoding, the measurement involves a parametric encoding direction. Figure 2.18 shows a typical T_2 mapping experiment where the parametric encoding direction is represented by a vector of echo time (TE).

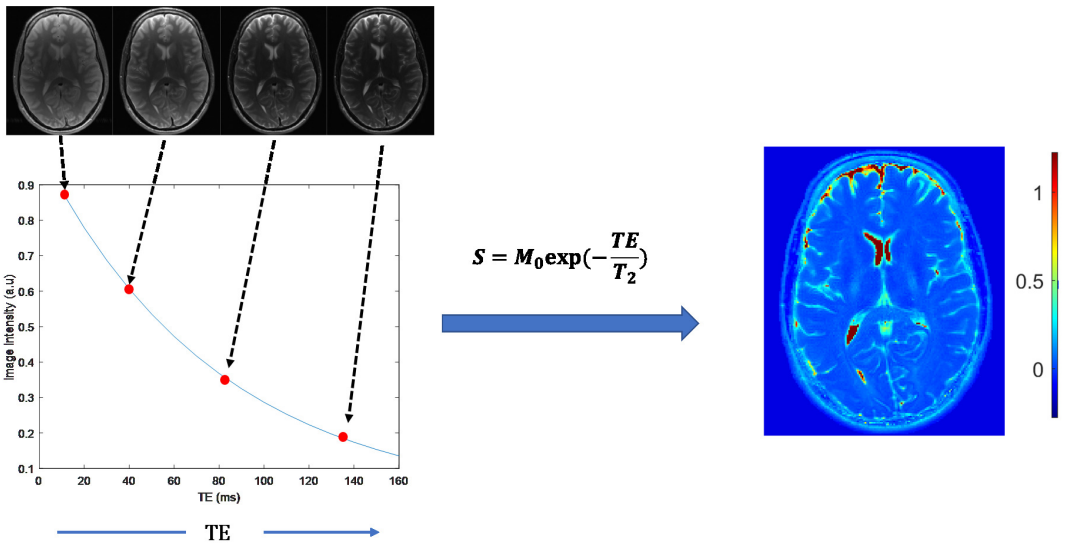

Figure 2.18: *T_2 mapping experiment using spin echo sequence. Several images are collected using different TE and T_2 map is obtained by fitting the signal intensities according to the signal model mentioned in equation 2.14*

Instead of first reconstructing the images and then later deriving the parameters of interest, the signal model can be integrated into the reconstruction, which can potentially enable the reconstruction of parametric maps from fewer data. Hence the reconstruction problem from equation 2.35 can be formulated as:

$$\min_\theta \sum_c^C \sum_n^N \|BFS_c f(\theta, t_n) - y_{c,n}\|^2 \tag{2.36}$$

The inversion problem in equation 2.36 is usually nonlinear and possibly with multiple local minima, which require good initialization and the application of additional constraints to obtain accurate parameter maps. Prior knowledge can be incorporated in the reconstruction by applying further constraints or penalty terms in addition to the data consistency term in equation 2.36

denoting the penalty function with $R(\theta, t_n)$ and the corresponding regularization parameter λ that control the relative weight of the penalty, the regularized inversion problem becomes:

$$\min_\theta \sum_c^C \sum_n^N \|BFS_c f(\theta, t_n) - y_{c,n}\|^2 + \lambda R(\theta, t_n) \tag{2.37}$$

Equation 2.37 represents a generalized model-based problem. To stabilize the solution, different penalty functions can be used for regularization. A common choice of constraint is the l_2 norm of the estimate, which is known as Tikhonov regularization. Additional prior knowledge like the estimate of the spatial support of the signal can be used as regularization. Several methods have been proposed to use analytical models or their linearization to constrain signal evolution in the a parametric dimension which is mentioned below.

Earlier work utilizing model-based reconstruction for T_2 mapping was proposed by Block et al. [105] that employed a signal model and directly estimated parametric maps. Instead of calculating any intermediate images, the proposed method estimated a spin density and a relaxivity map directly from the acquired k-space data using a numerical optimization technique. This work was proposed for radial k-space, Sumpf et al. [66] extended this work for Cartesian sampling, which is most commonly used. An automatic gradient-scaling method to avoid ill-conditioning of the inverse reconstruction problem was proposed along with a dedicated undersampling pattern which minimizes the undersampling artefact. Further work included an advanced signal model for T_2 relaxation that accounts for contributions from indirect echoes in a train of multiple spin echoes [69]. Tran-Gia et al. proposed an algorithm [133, 134] that alternates between image space and k-space and fills up the missing k-space information by the iterative (but still pixel-wise) fitting of model parameters. Recently, joint sparsity constraints on the parameter maps were exploited to improve the performance of the iteratively regularized Gauss-Newton method chosen for solving the nonlinear inverse problem [135] and have been demonstrated for T_1 mapping.

When the model-based reconstruction is combined with compressed sensing, the L_1 regularization is used to enforce signal sparsity. This means that additional constraints can be added to exploit this sparsity and that sparse sampling schemes can be spatio-temporal. For this purpose, the undersampling scheme should also be consistent with the spatiotemporal model. Exploiting the spatiotemporal sparsity has been used in the cardiac and dynamic MRI and includes kt FOCUSS [110] and kt SPARSE SENSE [119] techniques. The concept has been further extended

into quantitative MRI where the k-t principal component analysis was applied to generate parametric maps [128].

In addition, the model-based dictionary can be applied in a compressed sensing reconstruction [136]. MR Fingerprinting [137] is a dictionary-based approach in which highly undersampled pixel time courses are matched to a dictionary of possible time courses to derive T_1 and T_2 maps. While MR Fingerprinting does not rely on the image time series itself to be sparse, this method uses the idea that the dictionary elements can be sparse which can be used to represent the time course of each pixel [138]. In addition, various methods employ a signal model directly in the reconstruction to constrain the resulting images or time courses to follow a specific mathematical form [139–142]. Such approaches do not require the user to explicitly calculate all of the possible elements to form a dictionary, which may allow improved results as any values of the model parameters can result from the reconstruction (and not just those found in the dictionary).

Model-based reconstruction methods for accelerating qMRI have been explored and applied in this thesis, which will be discussed in Chapter 3,4 and 5.

2.7 Super-resolution

In many medical applications, high-resolution 3D images are required for early and accurate diagnosis. However, due to acquisition time constraints and hardware limitations, achieving this high spatial resolution is not always feasible. Therefore, several image processing techniques to augment the spatial resolution a posteriori have been introduced [15, 143–146]. On a standard MRI scanner, a basic interpolation (zero-filling) is available to decrease the voxel size of the images. Although this facilitates the visualization, no new information is introduced into the image [147]. Super-resolution reconstruction (SRR) techniques give the opportunity to improve the spatial resolution of the acquired images [148] efficiently. In SRR, an unaliased high-resolution image is estimated from a series of low-resolution images. The low-resolution images are acquired in such a way that each low-resolution image contributes new information to the reconstruction process. It is important to note that there is a difference between SRR and SR restoration. Although the goal of both SR concepts is to recover high frequency information that is lost or degraded during the image acquisition, the causes of the loss of high-frequency information are different [143]. SR restoration, which was introduced in optics, refers to al-

gorithms that mainly operate on a single image and attempt to recover information beyond the diffraction cutoff frequency by extrapolation. In contrast, the SR reconstruction method tries to recover the high-frequency components corrupted by aliasing. In this thesis, SRR based methods have been used.

Several different methodologies are developed in order to recover the high-resolution information from the acquired low-resolution data. These methodologies can be classified into two different techniques [149]: frequency domain [150–152] and spatial domain [146]. First, the limitations of MRI in acquiring high-resolution images with SRR as a potential solution will be discussed. Later, model-based SR reconstruction, which was developed in this thesis for T_2 mapping, will be discussed in Chapter 5.

2.7.1 Resolution challenges in MRI

As discussed in section 2.4, in each MRI experiment, a trade-off has to be made between the spatial resolution, the SNR and the acquisition time. Although a high-resolution 3D image is desired, 3D image acquisition is not always effective or possible. Therefore, it is most common to acquire a set of 2D slices, i.e. a multi-slice image. Acquiring this image at high resolution might allow observation of smaller details, but typically reduces the SNR, while a certain level of SNR is required to distinguish the signal of interest from the noise. The SNR could be improved by averaging over multiple acquisitions of the signal. However, this increases the acquisition time, while this is costly, uncomfortable for the patient and induces motion artefacts in the images. Moreover, the slice thickness is determined by the slice selection pulse, which in turn is determined by hardware limitations coupled with pulse sequence timing considerations, making the acquisition of thin slices not always feasible. As a result, multi-slice images are often acquired with a high in-plane resolution, but relatively thick slices Figure 2.19. However, these thick slices lead to large partial volume effects, which arise when two different tissues occur within a single voxel.

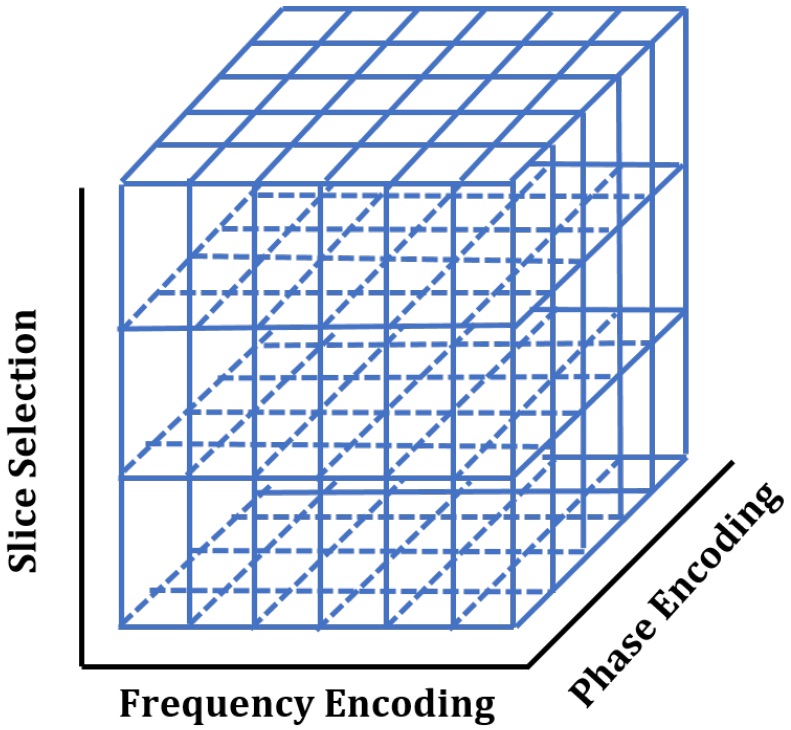

Figure 2.19: *Schematic representation of a low-resolution image, which has a high isotropic in-plane resolution and a slice thickness larger than this in-plane resolution.*

Due to partial volume effects, the borders between different tissues are blurred in the low-resolution image. The trade-off between spatial resolution, acquisition time and SNR can be improved at acquisition level by techniques such as PI [8, 9, 153], CS [40] and simultaneous multi slice (SMS) [85, 154]. An interesting complementary alternative is to use SRR.

2.7.2 Super-resolution reconstruction

In SRR, several distinct low-resolution observations of the same object are combined to reconstruct a high-resolution image. The first imaging domain in which SRR algorithms were applied was video processing [152], where a high-resolution frame was created from consecutive frames where the object was moved by a subpixel amount through a simple translation. The first application of SRR to MRI was reported in a patent filed in 1997 [155].

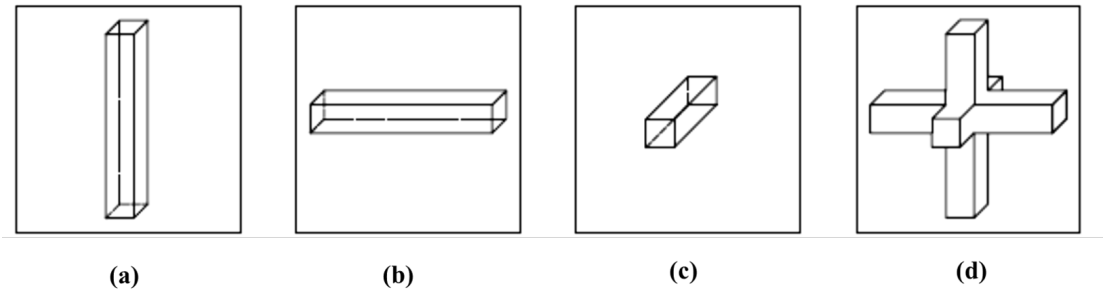

Figure 2.20: *The low-resolution k-space boundaries for the SR experiments by Herment et al. [2003]. (a-c) Sampled k-space data from the three 3D MRI acquisitions, (d) effective k-space sampling boundary. One of the first experiments with SR in MRI was performed by Herment et al.[2003]*

Their method combines partial k-space data, which are successively acquired by rotating the acquisition matrix of highly anisotropic 3D magnetic resonance angiography (MRA) volumes (Figure 2.20a-c). To reconstruct the image, the unknown regions contained in the compound volume of the three k-space data volumes (Figure 2.20d) were zero-filled. The other parts of k-space were weighted by the number of times the k-space region had been acquired. Next, a Fourier transformation was used to calculate the high-resolution image. The results showed an improvement in the spatial resolution, but only in the directions shared by the high-frequency k-space data samples. The method has been useful for imaging tissues with specific direction such as arteries, but not for brain imaging, where isotropic resolution is desired. Since then, several attempts have been made to improve both the in-plane and the through-plane resolution of MR images.

- **In-Plane Improvement:** The earlier SR methods [156, 157] focused on the improvement of the in-plane resolution of MR images. To achieve this in-plane resolution improvement, several images with a subpixel shifted FOV in the in-plane directions were acquired (Figure 2.21).

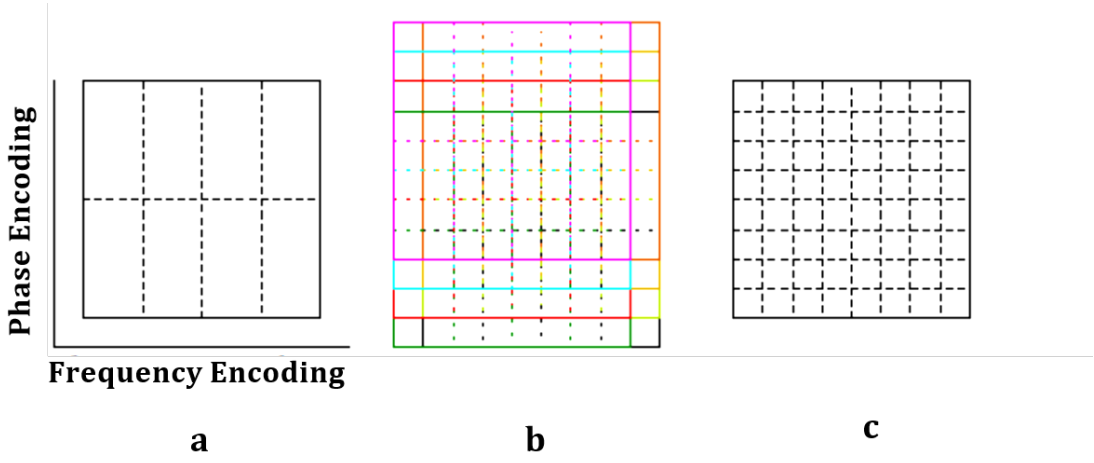

Figure 2.21: *SR experiment by Peled and Yeshurun [2001]. (a) Configuration for one low-resolution image, pixel size: 2×4 high-resolution pixel units. (b) Eight low-resolution images with subpixel spatial shifts, (c) High-resolution scan. Note that only the frequency and phase encoding direction are shown*

However, the validity of these methods was questioned by [158]. MRI images are Fourier-encoded in the frequency domain (k-space), and the FOV in the spatial domain is directly controlled by the choice of $\frac{1}{\Delta k}$(see section 2.4.2). Consequently, if the resolution and FOV of the low-resolution images are identical, then the locations of the frequency samples must be identical. The subpixel shift of the FOV in the in-plane direction corresponds with a linear phase modulation in the k-space. As a result, the shifted images acquire no new frequency content. Since the images contain the same information, except for measurement noise, it is not possible to improve the resolution. Greenspan et al. [15] showed that similar in-plane resolution improvements as in [156] can be replicated by using zero-padding interpolation. According to both [158] and [15], the apparent improvement in the in-plane resolution was due to an improvement in the SNR.

- **Through-plane improvement:** As the through-plane resolution of multi-slice images is often lower than the in-plane resolution; most SR methods focus on decreasing the slice thickness and reaching voxel isotropy [15, 149, 159]. Unlike in the in-plane dimension, the sampling rate in the through-plane dimension is usually too low, which causes the slice selection process to create aliasing [84, 160]. This aliasing provides the basis for using SRR algorithms to enhance the spatial resolution in the slice selection direction. Various acquisition and reconstruction strategies for SRR in the slice selection direction

have been proposed [144, 146, 148]. They will be discussed in the next section.

2.7.3 Acquisition strategies

In MRI, there is a consensus that resolution enhancement is not achievable in the in-plane directions since the Fourier encoding scheme excludes aliasing in the frequency and phase encoding directions [158]. Therefore, the low-resolution images are acquired with a high isotropic in-plane resolution and a slice thickness larger than this in-plane resolution (Figure 2.19). In multi-slice acquisitions, increasing the slice thickness improves the SNR of the acquired images. Moreover, as fewer slices need to be acquired to cover the region of interest, in turn, the acquisition time might be reduced. In order to recover the high-resolution information, the low-resolution images need to contain complementary information about the object. Several strategies can be adapted to acquire such a set of low-resolution images [146, 161].

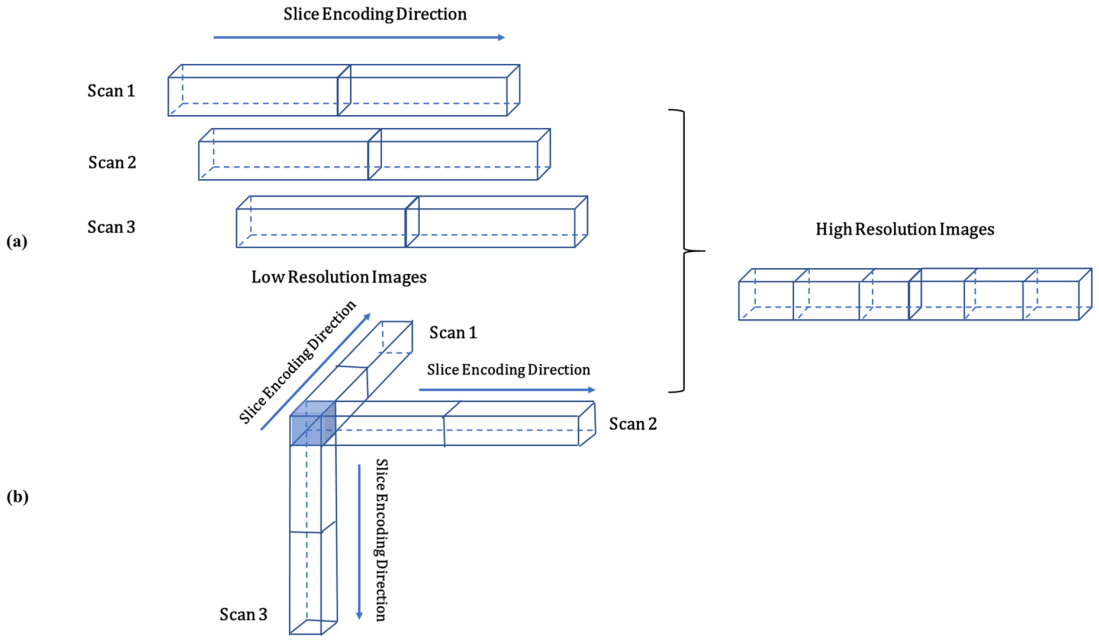

Figure 2.22: *Illustration of the (a) linear shifting and (b) orthogonal rotation experiment. For the linear shifting, each low-resolution scan is shifted by a known subpixel distance along the slice-encoding direction. For rotation, each of the low-resolution scans are rotated (90°) across the common encoding direction.*

- **Parallel stacks acquisition:** Several low-resolution images are acquired, shifted in the through-plane dimension by a known subpixel distance [15, 106]. In Figure 2.22a the

concept is shown for 6 low resolution images. To reach an isotropic resolution, a minimum of M low-resolution images is needed, whereby M is the ratio between the through-plane and in-plane resolution.

- **Multi-orientated acquisition:** Each acquired low-resolution image is rotated around one or multiple encoded axes [149, 159]. In Figure 2.22b scheme where low-resolution images are rotated about the phase encoding axis is shown. Rotation in image space results in rotation in the frequency domain. As such, acquiring the low-resolution images with different slice orientations ensures that each low-resolution image covers a different part of k-space. To ensure a short acquisition time, the minimal number of slice orientations that maximally cover the k-space by rotating about the center is chosen. Both parallel and rotated scan approaches have been shown to add information in the slice selection direction. However, acquiring the low-resolution images with rotational increments results in a more effective sampling of k-space than by shifting the low-resolution images by sub-pixel distances along the slice selection direction [148, 161]. It has been discussed by Van Reeth and Tham [146] that the orthogonal scan combination has the advantage of minimizing the redundancy between each acquired low-resolution image. Moreover, some artefacts only occur in the phase encoding direction. Thus by rotating the slice orientation around the phase encoding direction, rather than acquiring three orthogonal acquisition, the artefacts will be the same for each low-resolution image, and easier to correct. However, further quantitative research is needed to define the most efficient acquisition strategy

2.7.4 Applications

SRR has been successfully applied in anatomical [148, 159], functional [162] and diffusion brain MRI [163–165]. One of the biggest application domains of SRR is fetal brain imaging [165–169]. Typically, fetal brain images have a lower SNR than adult brain images because the signal strength received by the scanner is relatively weak due to the large distance between the fetal brain and the receiver coil. Furthermore, the fetus brain is much smaller than an adult brain. An additional challenge in fetal MRI is the elevated motion of the fetal brain. In qMRI, SRR reconstruction benefits from combining the parametric model with the SRR model. This has been shown in T_1 mapping [170] where the relaxation model was combined with the SRR model allowing the direct estimation of a high-resolution T_1 map from low-resolution images.

However, the acquisition of multiple LR images results in long scan times (TA $>$ 20 mins), hence limiting its use for clinical applications. The work in chapter 5 aims to explore the model-based reconstruction pertaining to SRR for accelerated T_2 mapping.

2.8 Image Quality Assessment

In order to assess the performance of the proposed method, the quality of reconstructed image is compared with the ground truth or the reference image. The assessment of image quality can be subjective or objective. The objective assessment can be done by comparing the test image to a reference image or by just testing the image quality on its own when reference is not present. There are so many image quality techniques largely used to evaluate and assess the quality of images such as MSE (Mean Square Error), PSNR (Peak Signal to Noise Ratio), SSIM (Structured Similarity Index Method) and FSIM (Feature Similarity Index Method) etc. The mean squared error (MSE) is the most widely used and also the simplest full reference metric which is calculated by the squared intensity differences of distorted and reference image pixels and averaging them with the peak signal-to-noise ratio (PSNR) of the related quantity [5]. RMSE is another type of error measuring technique used very commonly to evaluate the error magnitude. It is a perfect measure of accuracy which is used to perform the differences of forecasting errors from the different estimators for a definite variable [7] . RMSE is actually the square root of the Mean Square Error. Both of these metrics are a full reference metric and the values closer to zero are the better. Image quality assessment metrics such as MSE, PSNR are mostly applicable as they are simple to calculate, clear in physical meanings, and also convenient to implement mathematically in the optimization context. But they are sometimes very mismatched to perceive visual quality and also are not normalized in representation. With this view, researchers have taken-into account, two normalized reference methods to give structural and feature similarities. Structured similarity indexing method (SSIM) gives normalized mean value of structural similarity between the two images. The SSIM range from -1 to +1 with 0=no structural similarity and 1 for the identical image.

qMRI can produce highly valuable measures for applications in cancer diagnostics and treatment planning, clinical trials, and preclinical research. However, long acquisition times associated with qMRI decrease its utility. The potential to accelerate MRI acquisition with minimal effects on image quality is an exciting development for the future of radiology, and medicine as a whole. Thus, the aim of the thesis is to explore and optimize accelerated methods for qMRI,

which are discussed in Chapter 3, 4 and 5. This will transform the quantification of MR in terms of efficiency, cost-effectiveness and ultimately, clinical utility.

Chapter 3
Accelerating T_2^* Mapping with Maximum Likelihood Estimation (MLE) and Parallel Imaging (PI)

3.1 Introduction

The clinical utility of conventional parameter mapping is limited due to the lengthy acquisition times. The acquisition of undersampled data is a potential solution for faster parametric mapping. This can be achieved by either Parallel Imaging (PI) [8, 9] or by Compressed Sensing (CS) [13] or a combination of the two. Various applications of these methods to accelerate MRI have been discussed in Section 2.6.

In a typical quantitative MRI measurement, the tissue parameters of interest are obtained by acquiring several images at different values of acquisition parameters (e.g. TE, TR, flip angle) and performing a pixel wise model fitting. For this purpose, the magnitude of the acquired signal is typically used, and parameters are estimated using non linear Least Squares (LS). This approach assumes Additive White Gaussian Noise (AWGN) in the magnitude MR images. However, it has been shown in [171] that the noise probability density instead follows a Rician distribution which makes the conventional LS subjected to biased estimation. Two different approaches have been previously used to address this: the first approach justifies the use of LS as at high SNRs the Rician distribution approaches a Gaussian probability density function (PDF) [172] however, it can introduce bias at low SNRs. The second approach implemented a Maximum Likelihood Estimator (MLE) for retrieving relaxation parameters assuming Rician noise. Since the correct noise model is assumed, the proposed estimator is able to avoid the bias even at low SNRs [173]. In addition, the accurate estimation of relaxation properties using MLE for phased array coil configurations over a wide range of SNR has been demonstrated [174], albeit at the expense of increased computational time.

Multiple receiver coils have been used since the beginning of MRI [175], mostly for the benefit of increased SNR.

Over the years, a variety of methods for PI reconstruction has been developed (see section 2.6.2) to accelerate the MRI acquisitions. These methods differ by the way the sensitivity information is used. As discussed in Section 2.6.2.4, SPIRiT is based on the GRAPPA reconstruction but also draws its inspiration from SENSE in the sense that the reconstruction is formulated as an inverse problem in a very general way. The result is that reconstruction is the solution for least-squares optimization. This chapter presents a method based on MLE that can estimate the relaxation times in conjunction with SPIRiT. The approach is based on a high SNR assumption such that the noise can be modelled as Gaussian and estimates the parameters from the magnitude data. The method was tested on a multiecho gradient-echo (MEGE) T_2^* mapping experiment in a phantom and a human brain with retrospective undersampling. T_2^* maps were reconstructed up to an acceleration factor of 6 with a small error for the phantom and human brain.

3.2 Theory

3.2.1 The Pixelwise T_2^* Relaxation Model

Here we consider the MRI acquisition system using a Gradient Echo imaging sequence. A time-series of images which we denote in the vector format as $x_n \in \mathbb{C}^Q$, $(n = 1, .., N)$, represents the magnetization responses for Q pixels at the n^{th} time-frame. These magnetization images are related to the set of tissue parameter maps θ through a pixelwise separable nonlinear function, $f(\theta, t)$, in the following model equation:

$$x_n = f(\theta, t_n) + \epsilon_n \tag{3.1}$$

where t_n is the echo time (TE) in seconds and ϵ_n captures any deviation from the quantitative model due to noise and other non-idealizations. Considering the magnitude of the image and the selected sequence i.e., the response is sensitive to T_2^*) and independent of T_1, the set of parameter maps $\theta(\rho, T_2^*)$ consists of: the proton density map, $\rho \in \mathbb{R}^Q$; the $T_2^* \in \mathbb{R}^Q$ map representing the T_2^* spin-spin relaxation time per pixel.

These quantities control the exponential relaxation of the magnetization at each pixel, $x_n(q)$, via the following expression in which $f(\theta(q), t)$, with a slight change of notation should be

read as a pixelwise scalar nonlinear function:

$$x_n(q) = f(\theta(q), t_n) = \rho(q)\, e^{(-t_n/T2^*(q))} + \epsilon_n(q) \tag{3.2}$$

3.2.2 SPIRiT

In this work, SPIRiT [101] is used as the PI method (The code is available at `https://people.eecs.berkeley.edu/~mlustig/Software.html`). Assume, C coils are used for data acquisition. Redefine $x_{c,n}$ as the matrix of images from all coils and echoes and $y_{c,n}$ as the vector of acquired k-space data from all coils and echoes, G_c is the SPIRiT kernel as explained in Section 2.6.2.4, F^{-1} as the inverse Fourier transform applied individually to each coil and P as the undersampling operator. The SPIRiT operation can be expressed as:

$$\hat{x}_{c,n} = F^{-1}(G_c)x_{c,n} \tag{3.3}$$

where G_c is a series of convolution operators that convolve the entire k-space with the appropriate calibration kernels. The kernel is transformed into image space through Fourier operator before applying to the image series $x_{c,n}$. Applying the equation 3.3 on $x_{c,n}$ is the same as attempting to synthesize every point from its neighborhood as used in GRAPPA but in image space.

3.2.3 Pixelwise Maximum Likelihood Estimation (MLE)

Estimation theory indicates that ML estimate of parameters θ given the set of magnitude magnetization images $\{x_n\}_1^N$, consists of maximizing the following conditional probability distribution $P(\{x_n\}_1^N|\theta)$:

$$\hat{\theta} = \arg\max_{\theta}\{L(\theta|x_n)\} \tag{3.4}$$

where log-likelihood function is defined as :

$$\{L(\theta|x_n)\} := \log \prod_{n=1}^{N} P(x_n|\theta) \tag{3.5}$$

Modeling the deviations, ϵ_n, as complex independent and identically distributed Gaussian noise

for the N echoes, the optimization in equation 3.5 is equivalent to:

$$\arg\min_{\theta} \sum_{n=1}^{N} \|x_n - f(\theta, t_n)\|^2 \tag{3.6}$$

3.2.4 SPIRiT MLE

In addition to the convolution through SPIRiT and the parameter estimation with MLE, consistency with the data acquired is necessary. The data acquisition consistency is given by:

$$y_{c,n} = BF(x_{c,n}). \tag{3.7}$$

In Cartesian acquisitions, the sampling mask B selects only acquired k-space locations and is used to accelerate the image acquisition. In this case, B is fixed for all the coils and echos. Various different types of sampling pattern can be used, i.e. uniform, variable density, or pseudorandom patterns.

As described in section 2.5.2, the MEGE sequence is very susceptible to magnetic field inhomogeneity, that causes the phase of image $x_n \in \mathbb{C}^Q$ to have phase perturbations. In the case where the complex image is used to estimate θ, phase perturbations appear as an artefact on the estimated parameters. To mitigate this, the image was split into magnitude and phase, and ML estimation was performed on the magnitude image only. The phase was added back to make the image complex for data consistency step.

Since SPIRiT is a coil by coil autocalibrating operator it outputs the multicoil image $x_{c,n}$ that can be converted into single image using root sum of squares. In this work, the MLE operation is modified to output the image x_n to cater the multicoil nature of the image. The ML estimator uses the weighted LS that estimates proton density according to the sensitivity information of the coils. With the image $x_{c,n}$ as the input, replacing $f(\theta, t_n)$ with the monoexponetial decay from equation 3.2 our ML estimator from equation 3.6 takes the following form:

$$\theta = \arg\min_{\theta} \sum_{n}^{N} \sum_{c}^{C} \| |x|_{c,n} - \rho_c . exp(-t_{n.}/\mathrm{T}_2^*) \|^2 \tag{3.8}$$

where ρ_c is the PD, which is weighted according to coil sensitivities. The SPIRiT formulation presented in this work can be solved with alternating projection [176]. The proposed approach

applies PI and the MLE constraint iteratively with three sequential operations: (i) PI reconstruction, (ii) MLE operation (iii) Promoting consistency with the data acquisition. Details of the algorithm are as follows:

Algorithm 1: SPIRiT MLE

Data: k-space measurements $\{y_{c,n}\}$, $G_{c,n}$ (SPIRiT Operator)

Result: (ρ_c, T_2^*)

$x_{c,n}^0 = F^{-1} y_{c,n}$; ρ_c, T_2^* = randomly initialized ;

Optional Parameter: n-iter= Maximum number of iterations(default=25), Toll Diff=reconstruction difference between two iterations (default=10^{-04}) ;

while *l< n-iter and* $\|x^{(l)} - x^{(l-1)}\|_2 / \|x^0\|_2 >$ *Toll Diff* **do**

SPIRiT Operation: $x_{c,n}^{(l)} = F^{-1}(G_c) x_{c,n}^{(l-1)}$;

Split the $x_{c,n}$ *into magnitude* $|x|_{c,n}$ *and phase* $\phi_{c,n}$;

MLE: $\arg\min_\theta \sum_n^N \sum_c^C \| |x|_{c,n} - \rho_c . exp(-\, t_{n.}/T_2^*) \|^2$;

Insert the Phase back: $x_{c,n}^{(l)} = f(|\theta|, t_n) . * exp(li * \phi_{c,n})$;

Data Replacement: $x_{c,n}^{(l)} = F^{-1}[(1-B) F x_{c,n}^{(l)} + B y_{c,n}]$;

end

3.3 Methods

3.3.1 Image Acquisition

The proposed approach was demonstrated for T_2^* mapping in the custom made in-house phantom. The MRI phantom consisted of 9 sealed 10 ml BD syringes (http://www.bd.com) containing $MnCl_2$ solutions with linearly increasing amounts of manganese ions (Mn2+) as a MRI contrast agent. These $MnCl_2$ solutions were prepared by diluting 1 mol/l $MnCl_2$ stock solution (Sigma Aldrich, Gillingham, UK) with distilled water (Baxter, Thetford, UK) into 0.05, 0.07, ..., and 0.21 mmol/l $MnCl_2$ solutions which produced T_2^* relaxation rates in the range of normal appearing brain tissue [24]. The phantom was placed on the headrest of the scanner so that the syringes were oriented parallel to the main magnetic field. Before and between the

experiments, the phantom was stored in the scanner room with a temperature of 20.0 1.5 °C to reduce temperature-induced changes of the $MnCl_2$ solution relaxation rates [24]. All measurements were performed on a 1.5T clinical scanner (GE Healthcare, Waukesha, WI, USA) using a 3D-enhanced fast gradient-recalled echo sequence with the following parameters (16 echoes, TR = 87 ms, FOV = 256mm, 256x256 matrix, readout bandwidth=31.56 KHz, flip angle 15°, 2mm slice thickness). The total acquisition time for acquiring 32 slices was approximately 18 minutes. Poisson disk undersampling mask was used as the sequence had two phase-encodings to allow the 3D acquisition. Poisson-Disk sampling pattern provides even, but random distribution of samples and is suited for CS & PI type reconstructions [177]. The dataset was retrospectively undersampled by acceleration factors (R) of 2, 3, 4, 5, and 6 (see section 2.6.2.1). The sampling mask consisted of an autocalibration region of 24 x 24 in the k_y–k_z plane (Figure3.1).

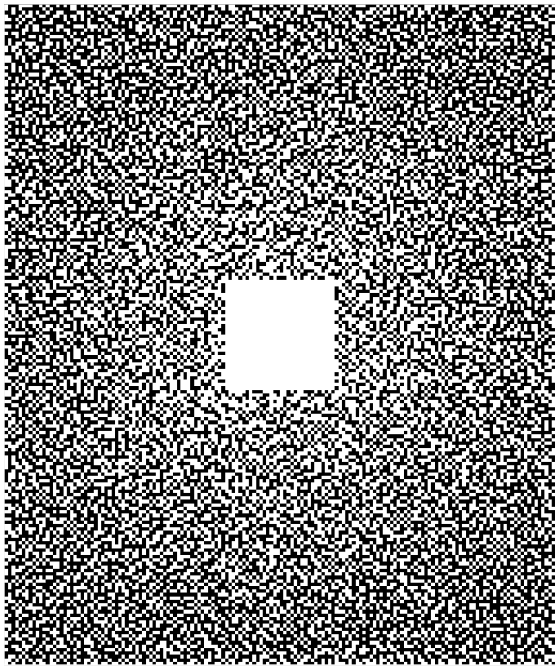

Figure 3.1: *Poisson disk undersampling mask for R=2. The white voxels indicate sampled k-space location and black non-sampled locations. Sampling according to a Poisson-disc distribution provides a high degree of incoherence and at the same time uniform distance between samples.*

3.3.2 Image Reconstruction and Analysis

All algorithms were implemented in Matlab and reconstructions were conducted on a standard laptop with 4GB RAM and dual-core 2.60GHz CPU. A 7x7 SPIRiT kernel was calibrated from the autocalibration region. The fully sampled dataset was multiplied by the mask to acquire the undersampled k-space. The undersampled k-space was inverse Fourier transformed along the readout direction to get the initial estimate image $x_{i,n}^0$. Following the SPIRiT operation, T_2^* estimation was performed on a pixel-wise basis using the monoexponential decay signal. To determine the error of the estimated T_2^* maps, the root mean square error (RMSE) was calculated between the fully sampled and undersampled dataset. In addition, an ROI analysis was performed for different compartments of phantoms, and T_2^* values were compared between fully sampled and accelerated datasets.

3.4 Results

T_2^* maps estimated from the fully sampled, and undersampled dataset of the phantom reconstructed using the proposed approach is shown in Figure 3.2. With the increase in the acceleration factor, the error increased (bottom row) primarily for the compartments with the longer T_2^* values. For the compartments with the short to intermediate T_2^* values, the error is substantially low for acceleration factors of 2,3 and 4. For the compartments with the longer T_2^* values, the error is higher even for R=2. This can be attributed to the fact that the T_2^* values were high as compared to the TR used (87 ms). The RMSE values also increased with the increase in the acceleration factor with acceleration factor R=6 exhibiting the highest RMSE of 14.2 ms.

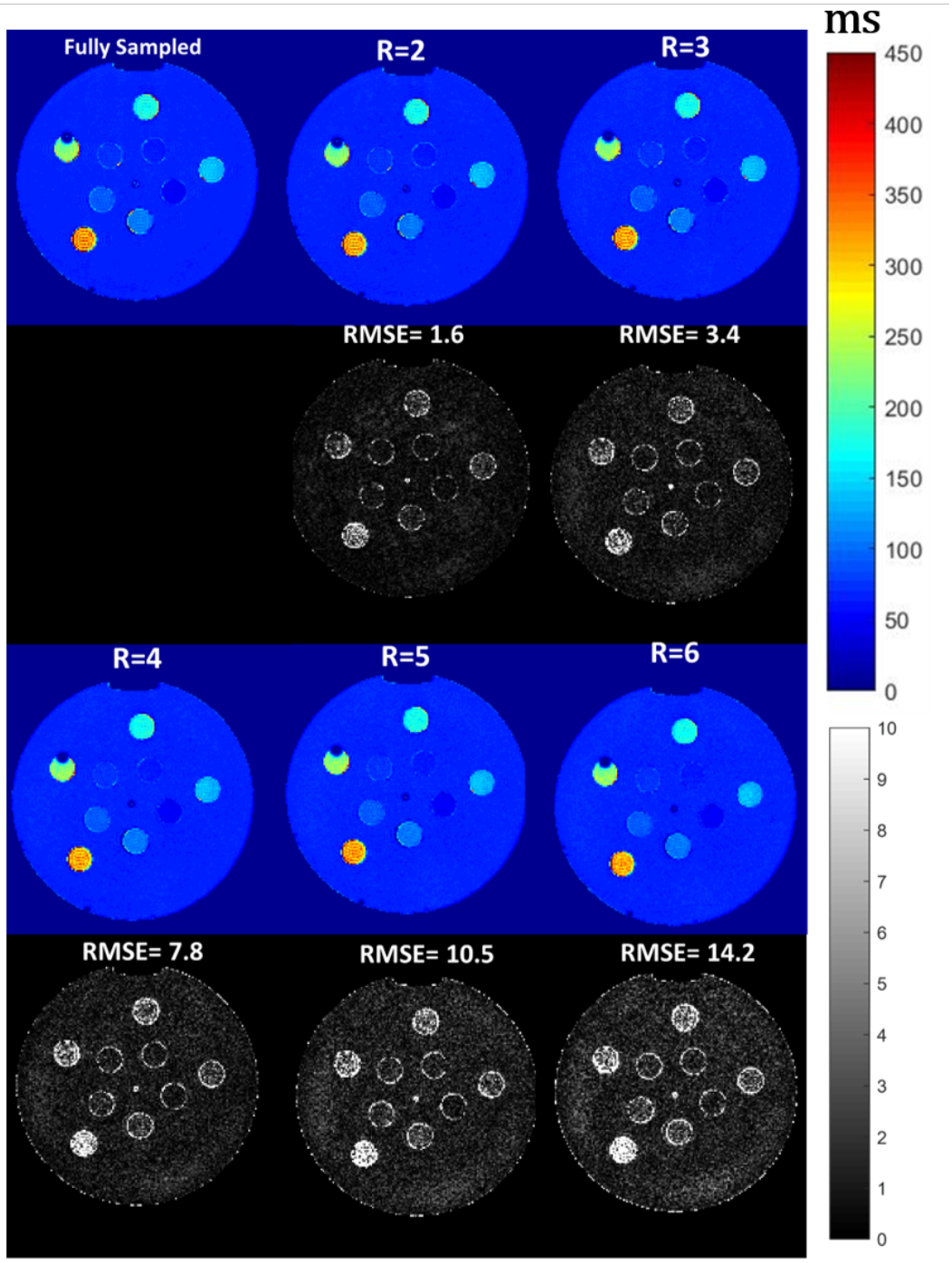

Figure 3.2: *MEGE T_2^* mapping with SPIRiT MLE. T_2^* maps of the fully sampled dataset and from reconstructions with R=2,3,4,5 and 6. The corresponding difference of the T_2^* maps between fully sampled dataset and reconstructions are shown below the maps. The RMSE of each reconstruction is listed under each T_2^* map.*

The ROI analysis of the phantom compartments revealed that at shorter T_2^*, the accelerated data were comparable with the fully sampled dataset (Figure 3.3). For compartments, 1 to 6 which have shorter T_2^* values, the fully sampled and accelerated datasets show very similar values. For compartment 7, the error increased with the R=4, 5 and 6 demonstrating a relative error of 3-5%. For compartment 8, the error is more pronounced with R=6 demonstrating a relative error of 7% (mean T_2^* value for R=6 was 94 ms as compared to fully sampled 101 ms). For compartment 9, similar results are seen where the mean T_2^* for fully sampled is 116 ms and 111 ms for R=6.

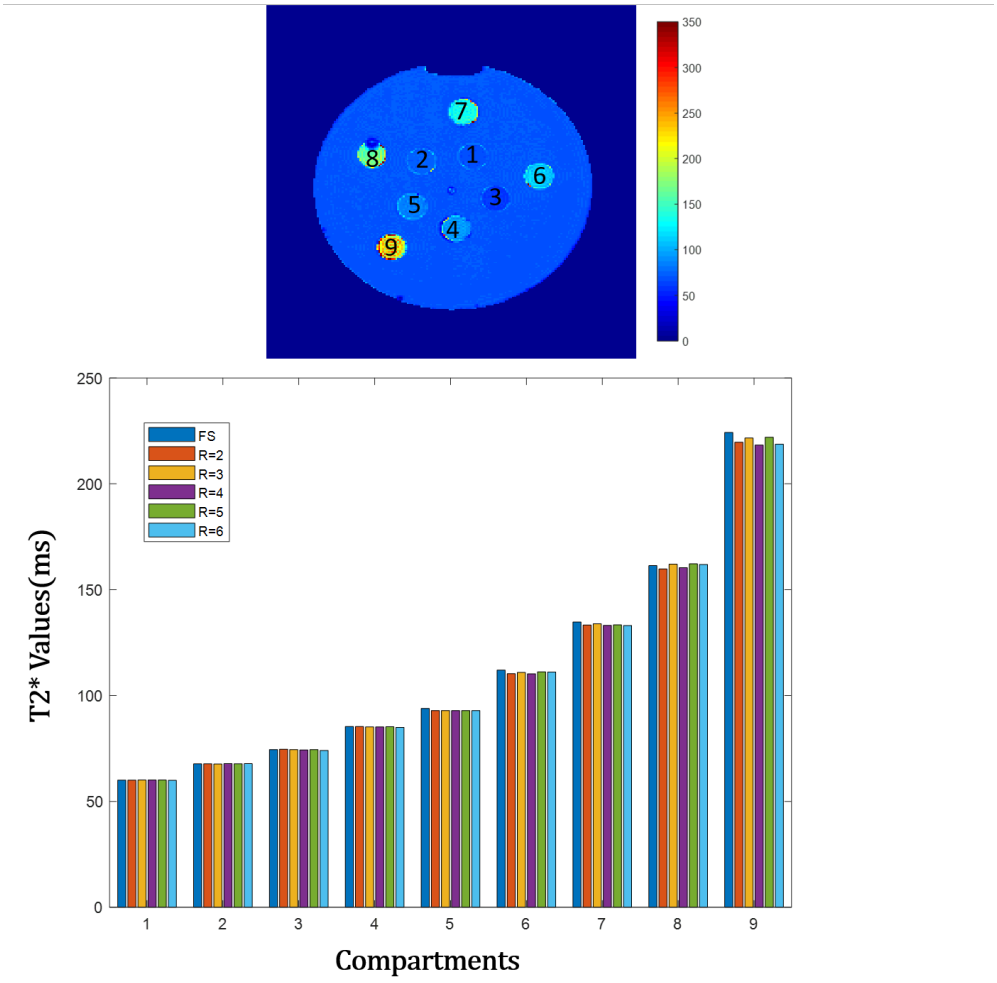

Figure 3.3: *ROI analysis of the phantom to compare T_2^* values of a fully sampled and under-sampled dataset from different compartments. (Top) T_2^* map with different labeled compartments (Bottom) Bar chart showing mean T_2^* values of different compartments for different acceleration factors.*

The above findings were also confirmed for in-vivo conditions. Figure 5.2 shows an axial slice of the T_2^* from the fully sampled datasets and reconstructions with different acceleration factors. Again, the undersampled datasets demonstrate increasing error with the increase in the acceleration factor. Overall, the error is higher around the skull boundary and the CSF. The acceleration factor 2 demonstrated the least error with an RMSE of 3.1 ms, for R=3, the RMSE was 6.01 ms with R=6 showing the highest error (RMSE=25 ms).

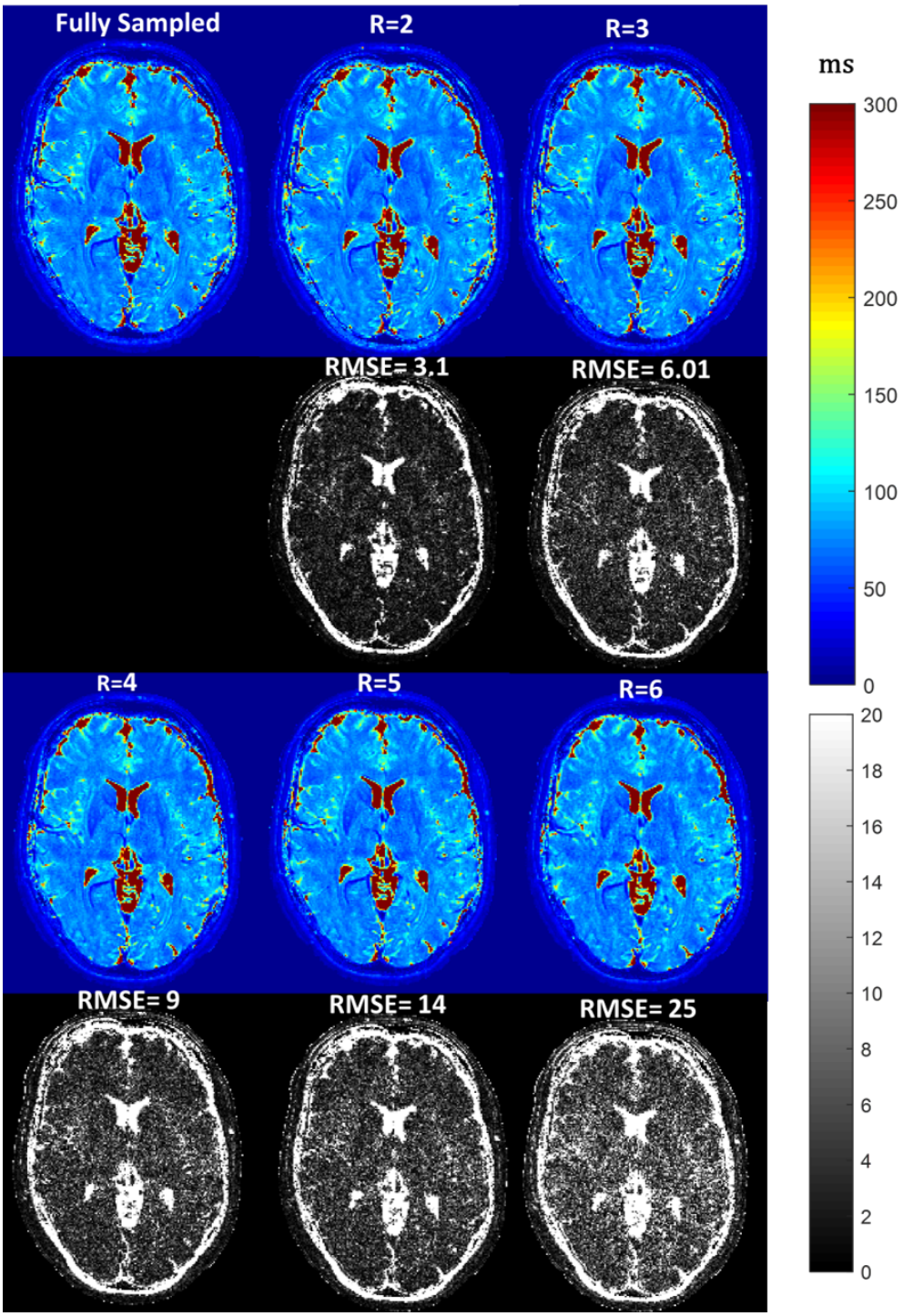

Figure 3.4: *MEGE T_2^* mapping with SPIRiT MLE. T_2^* maps of the fully sampled dataset and from reconstructions with R=2,3,4,5 and six shown. The corresponding difference of the T_2^* maps between fully sampled dataset and reconstructions are shown below the maps. The RMSE of each reconstruction is listed under each T_2^* map.*

3.5 Discussion

We have presented a fast T_2^* mapping method with MLE and the PI. The performance of the proposed method was evaluated in the retrospective undersampling and comparison was made with the fully sampled reference scan. A 6-fold reduction in imaging time can be achieved for in-vivo T_2^* mapping (TA=3 minutes).

Phase variations are always present in the images because of hardware imperfection, susceptibility, and motion. Since phase is an essential component of the MRI signal, correct reconstruction of the phase values is critical for the convergence and accuracy of image reconstruction. While it is mathematically possible to estimate both phase and magnitude information using the model-based CS method [12], additional constraints from pre-estimated phase maps can reduce the degree of freedom in parameter estimation and improve the accuracy. A previous study used fully sampled centre PE lines to generate a low-resolution phase map for the reconstruction [40]. However, spatial nonuniformity of the phase maps precludes from using low-resolution phase images to constrain the reconstruction.

As mentioned above, due to the nature of the phase perturbations in the MEGE data, the T_2^* maps can be prone to artefacts if the phase is not accounted for. Figure 3.5 showed the impact of phase perturbations when the image was not split into the magnitude and phase before pixel wise non-linear least squares.

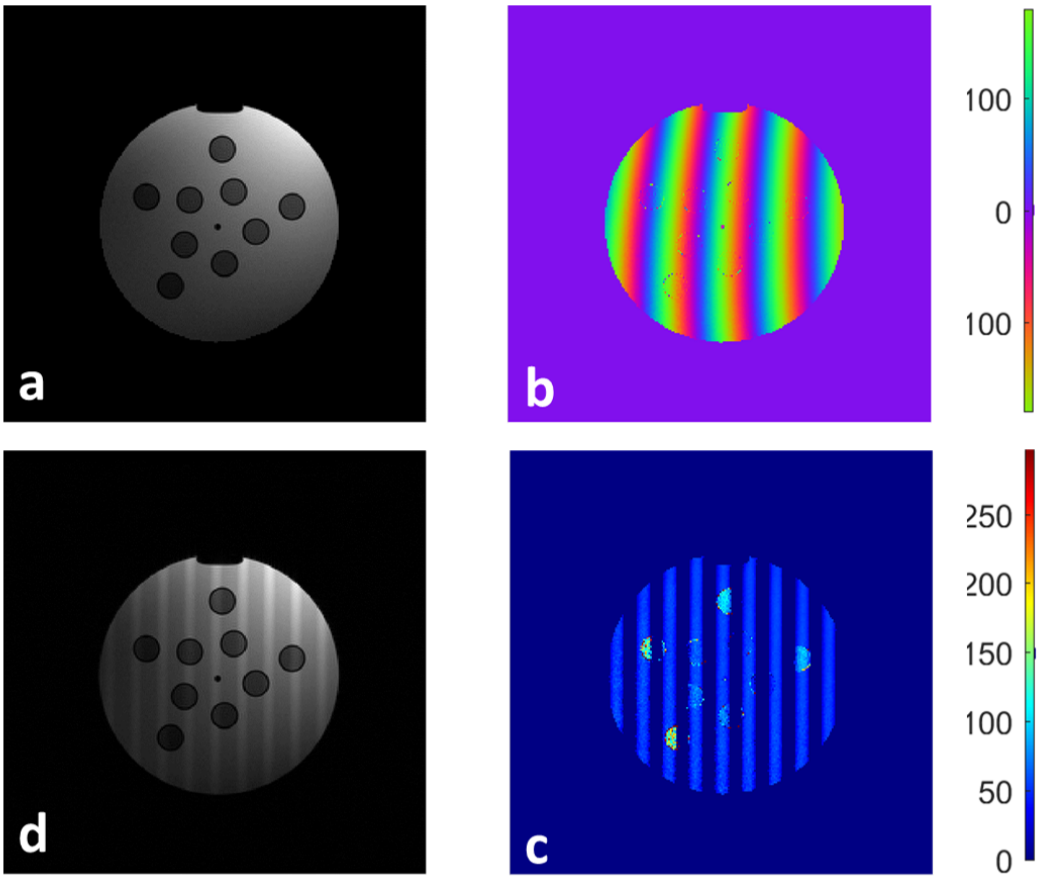

Figure 3.5: *(a) Fully Sampled magnitude image from a MEGE acquisition (b) Phase image with different phase perturbations (c) Reconstructed T_2^* map (d) PD when the image is not split into magnitude and phase.*

As mentioned before, this proof-of-concept study aimed to evaluate the proposed algorithm in the context of T_2^* with retrospective undersampling. However, determining the accuracy of the technique in this context is a difficult task due to various reasons. Firstly, the unavailability of the reliable ground truth for the phantom as the values change over the course of time and with the temperature. This can be mitigated by the use of standardized phantoms (such as NIST phantom [178]) or using the numerical phantoms. For that reason, the numerical phantom which can provide ground truth will be used in the next chapter. Secondly, even if there is a ground truth available there is no set standard of the accepted deviation from the ground truth. To date, the work done in the realm of compressed sensing for MRI has evaluated the methods based on different image quality metrics (see section 2.8) which is subjective. In addition, there

is no literature indicating the acceptable range of the quantitative parameters in normal and disease states. So, deriving a solid conclusion is not possible without involving the diagnostic assessment from the radiologists that can determine the optimum image quality. However, this still is not the very objective way to determine the accuracy and is an area that needs to be explored further.

In this Chapter, the only magnitude of the image was used to estimate the parametric maps. Chapter 4 will assess the importance of phase as a function of the degree of freedom in improving the accuracy of the current method. In addition, prospective undersampling will be employed to ascertain the performance of the approach in real clinical settings. The proposed method can also be combined with an additional image sparsity constraint commonly used in compressed sensing reconstructions [179]. However, tuning reconstruction parameters with multiple constraints needs to be further studied. The benefits of joint reconstruction using multiple constraints also need to be investigated.

3.6 Conclusion

The aim of this proof-of-concept was to have an initial investigation of the role of PI acceleration in qMRI. The method allows a significant reduction of the required data without compromising the quality of the parameter maps. However, the potential of PI in exploring the complex information in a coherent way need to be explored to improve the accuracy of the proposed method.

Chapter 4

Improved Accuracy of Accelerated 3D T_2^* Mapping with Coherent Parallel Maximum Likelihood Estimation

4.1 Introduction

Conventional sensitivity encoding (SENSE) reconstruction is based on equations in the complex domain. These equations typically operate on complex numbers, and the reconstruction yields an estimate of the underlying image in a minimum least-squares sense. In some MR applications, only the magnitude of an image is of concern and the phase is discarded. However, using this coherent information (magnitude and phase) can still be useful in the cases of undersampled acquisitions when the number of unknowns is higher than the measurements.

In the context of parametric estimation, various studies have focused on using the phase information in reconstruction for various applications. These include correction of magnetic field inhomogeneities for robust T_2^* mapping with joint iterative reconstructions for fully sampled acquisitions [180–182]. The coherent fitting has also been shown to be useful in water and fat separation [142]. Moreover, the emerging Magnetic Resonance Fingerprinting (MRF) is shown to greatly benefit from incorporating complex signal models [137]. However, its value has not been explored to benefit accelerated acquisitions [9]. In this Chapter, we explore the benefits of a reconstruction that utilizes the coherent information in both the PI and the MLE for accelerated T_2^* mapping via k-space subsampling. Due to undersampling, the ratio of the number of measurements to the number of independent unknowns plays a crucial role in the performance of the algorithm being used to solve this non-convex problem. The purpose of this work is, therefore, to investigate the acceleration achievable by exploiting the complex model to improve this ratio. On a number of synthetic and real-world data sets, we show that using both phase and the magnitude for parametric estimation can improve the reconstruction. This can be seen as a refinement of Chapter 3 by properly incorporating coherent information while dealing with the phase sensitivity issues previously highlighted.

4.2 Theory

4.2.1 The Modified Pixelwise T_2^* Relaxation Model

As discussed in Chapter 3, the MRI acquisition system using a Gradient Echo imaging sequence is considered here. A time-series of images which we denote in the vector format as $x_n \in \mathbb{C}^Q$, $(n = 1, .., N)$, represents the magnetization responses for Q pixels at the n^{th} time-frame. Here we are considering both the magnitude and the phase of the image, so the equation 3.1 will be modified to take into account the phase terms resulting into the following pixelwise exponential relaxation expression for image $x_n(q)$:

$$x_n(q) = f(\theta(q), t_n) = \rho(q)\, e^{(-t_n/T2^*(q)) + j(\varphi(q) + 2\pi\omega(q)t_n)} + \epsilon_n(q) \tag{4.1}$$

where t_n is the echo time (TE) in seconds and ϵ_n captures any deviation from the quantitative model due to noise and other non-idealizations. The set of parameter maps $\theta(\rho, T_2^*, \varphi, \omega)$ consists of: the proton density map, $\rho \in \mathbb{R}^Q$; the $T_2^* \in \mathbb{R}^Q$ map representing the T_2^* spin-spin relaxation time per pixel; the unknown constant phase map, $\varphi \in \mathbb{R}^Q$, associated with the coil measurements (often absorbed into the proton density); and $\omega \in \mathbb{R}^Q$, the off-resonance frequency map, caused by the field inhomogeneities which can be related to the system (eddy currents) or biological effects (for example at the tissue-air interface). This off-resonance frequency term ω is crucial in this context as it avoids the imaging issues observed when considering a phase in Chapter 3.

4.2.2 Parallel Imaging Acquisition Model

As discussed in section 2.6.2, the acquisition model for multichannel coils can be expressed as:

$$y_{c,n} = E_c x_n + \eta_{c,n} \quad for\ c = 1, 2, ...C \tag{4.2}$$

where,

$$E = \begin{pmatrix} BFS_1 \\ \vdots \\ BFS_C \end{pmatrix}$$

The acquired k-space data is recorded in the C m-dimensional vectors, $y_{c,n} \in \mathbb{C}^m$, where $\eta_{c,n} \in \mathbb{C}^m$ is the receiver channel noise. This noise is assumed to be additive, zero mean and uncorrelated i.e. AWGN. Here E is the encoding operator that includes the Fourier transform matrix F, the subsampling masks B and the sensitivity maps S_c.

4.2.3 Coherent or Magnitude: Number of Degrees of Freedom

In order to exploit both the parallel imaging and the relaxation model we need to jointly reconstruct the complex image sequence and the parameter maps, and the number of measurements required to estimate these quantities should depend on the number of unknown parameters. While at first glance it might appear that imposing a magnitude only model for the relaxation will result in fewer unknowns - we do not need to calculate $\phi(q)$ and $\omega(q)$ in equation 4.1-it turns out that using the full complex relaxation model results in fewer *independent* degrees of freedom. This can be explained with a dimension counting argument in the image space assuming the idealized case of no noise and the exact T_2^* relaxation model constraint (equation 4.1).

- For magnitude only joint estimation: given the parameter maps $(\rho, T_2^*) \in \mathbb{R}^{2Q}$ the image sequence, $x \in \mathbb{C}^{QN}$ is fully defined up to the phase of the complex image per echo time. Thus the total number of *independent* unknowns is $2Q+QN$ for the combined parameter maps and phases.
- For complex joint estimation: for the complex estimation case four parametric maps $(\rho, T_2^*, \phi, \omega) \in \mathbb{R}^{4Q}$ have to be estimated. However, now, the complex image sequence is fully defined by the parametric model. Thus the total number of independent degrees of freedom is $4Q$, which is smaller than the magnitude-only model as long as the number of echo times is greater than two.

4.2.4 Pixelwise Maximum Likelihood Estimation (MLE)

As discussed in Chapter 3, the ML estimate of parameters θ (that takes into account the phase), given the set of magnetization images $\{x_n\}_1^N$, consists of maximizing the following conditional probability distribution $P(\{x_n\}_1^N|\theta)$:

$$\hat{\theta} = \arg\max_{\theta}\{L(\theta|x_n)\} \tag{4.3}$$

where log-likelihood function is defined as :

$$\{L(\theta|x_n)\} := \log \prod_{n=1}^{N} P(x_n|\theta) \tag{4.4}$$

Modeling the deviations, ϵ_n, as complex independent and identically distributed Gaussian noise for the N echoes, the optimization in equation 4.4 is equivalent to:

$$\arg\min_{\theta} \sum_{n=1}^{N} \|x_n - f(\theta, t_n)\|^2 \tag{4.5}$$

4.2.5 Coherent Parallel MLE

Given the above data model equation 4.2 and equation 4.5 and by assuming AWGN on the measurements, the reconstruction problem can be formulated as the joint penalized MLE estimation for the parameter maps, θ and the set of magnetization images $\{x_n\}_1^N$:

$$\arg\min_{x,\theta} \sum_{i=1}^{C} \sum_{n=1}^{N} \|y_{c,n} - E_c x_n\|^2 + \lambda_1 \|x_n - f(\theta, t_n)\|^2 + \lambda_2 \|x_n\|_{TV} \tag{4.6}$$

The first term defines the data fidelity, the second term is the deviation of the estimated set of images from the quantitative model and the third term is the spatial regularization on the image series $\{x_n\}_1^N$. λ_1 is the regularization parameter which weights the model-consistency terms and plays a key role to stabilize the solution of potentially ill-posed equations and λ_2 is the weight of the spatial regularization. For spatial regularization, Total Variation (TV) is used here, though other choices are possible.

Our approach combines the traditional multichannel model (see section 2.6.2.1) with an MLE approach that imposes both the exponential relaxation model and the multichannel model jointly in the complex signal domain. This joint coherent MLE approach imposes additional phase restrictions in the quantitative model that are ignored when using a magnitude-only estimate, e.g.Block et al. [183]. This reduces the underlying number of degrees of freedom in the model and hence, can improve reconstruction performance.

We solve full non-convex optimization equation 4.6 by using an alternating minimization approach. Let θ^l denote the estimated parameter maps at iteration l. By fixing θ, solving equation

4.6 with respect to x_n at iteration l reads:

$$x_n^l = \arg\min_x \sum_{c=1}^{C}\sum_{n=1}^{N} \|y_{c,n} - E_c x_n\|^2 + \lambda_1 \|x_n - f(\theta, x_n)\|^2 + \lambda_2 \|x_n\|_{TV} \tag{4.7}$$

For this step, Fast Iterative Shrinkage-Thresholding Algorithm (FISTA) [184] is used with the TV regularization [185]. On the other hand, holding x_n fixed allows equation 4.6 to be written as a pixelwise separable nonlinear least squares problem with respect to θ. This can then be solved using Matlab's nonlinear least squares (NLS) fitting package on each pixel sequence in turn. Initialization plays an important role in solving such non-convex optimization problems, hence conventional SENSE [8] was used to obtain the initial estimate of x_n, while θ was initialized randomly. Subsequently, the θ values obtained at the previous iteration were used to initialize the Matlab NLS for the next iteration. The steps of the algorithm are as follows:

Algorithm 2: Coherent Parallel MLE

Data: k-space measurements $\{y_{c,n}\}$, Encoding Operator (E)

Result: $\theta = \mathrm{T}_2^*, \rho, \varphi, \omega$

x_n^l=Initialize by SENSE ; θ^0= randomly initialized ;

Optional Parameter: n-iter= Maximum number of iterations (default=25);

for *l=1:n-iter* **do**

Step1: Using current estimate of x_n^l, update θ;

$\theta^{l+1} = \arg\min_\theta \|x_n^l - f(\theta^l, t_n))\|^2$;

Step2: Using current estimate of θ^{l+1}, update x_n ;

$x_n^l = \arg\min_x \sum_{c=1}^{C}\sum_{n=1}^{N} \|y_{c,n} - E_c x_n\|^2 + \lambda_1 \|x_n - f(\theta, x_n)\|^2 + \lambda_2 \|x_n\|_{TV}$;

end

4.3 Materials and Methods

4.3.1 Numerical Phantom

The proposed approach was tested on a digital anatomical brain phantom available from the BrainWeb Simulated Brain Database [2]. This dataset by default is segmented into 6 material classes, i.e. Background, Grey Matter (GM), White Matter (WM), and Cerebrospinal Fluid (CSF), Adipose, Skin/muscle. The original slice was re-sized to a matrix size of 256 x 256. Quantitative maps were then obtained by replacing the tissue labels with their corresponding

T_2^* values. T_2^* values of the components are mentioned in Table 4.1 as reported in [51]. Since we are using the constant T_2^* values, the model is somewhat idealized and does not address inaccuracies associated with partial volume effects or many of the other issues with real MRI. However, it serves as a useful test bed to provide good proof of concept. A quadratic phase term was added that is zero in the centre of the image and $\pi/4$ at the corners (Figure 4.1). Coil sensitivities were simulated using the Noisy Parallel MRI data toolbox [186]. The dataset was retrospectively undersampled by acceleration factors (R= 2,3,4,5,6) with variable density Poisson disk patterns [113] including an autocalibration region of 32×32 in the k_y-k_z plane.

Tissue	Index	Proton Density	T_2^*(ms)
Background	0	0	-
CSF	1	100	2000
Grey Matter	2	100	65
White Matter	3	80	77
Adipose	4	80	60
Skin/Muscle	5/6	80	56

Table 4.1: *Tissue types used from MNI segmented brain phantom. Each tissue type was indexed and then T_2^* values were assigned to them. Note that the values are for 1.5T.*

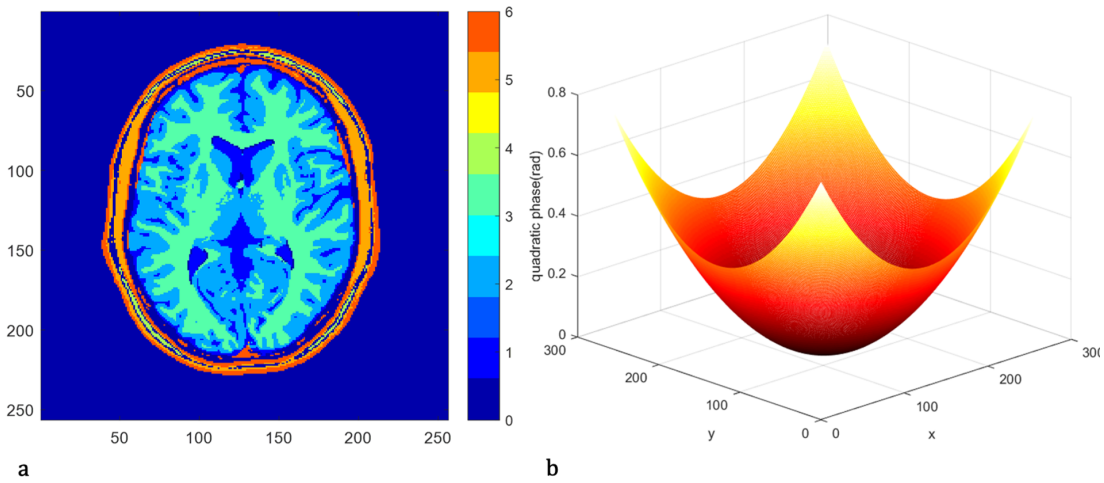

Figure 4.1: *(a) The segmented anatomical brain phantom [2] colored by index: 0 = background, 1 = CSF, 2 = grey matter, 3 = white matter, 4 = adipose, 5 = skin/muscle, 6 = skin.(b) The density map with a quadratic phase that is zero at the center of the image and $\pi/4$ at the corners.*

4.3.2 In-vivo Data

The in-vivo data were acquired from a healthy human brain on a 1.5T clinical scanner (GE Healthcare, Waukesha, WI, USA). Permission from the ethical review committee was obtained for all the in-vivo imaging studies, and written informed consent for the study and its publication was obtained from all participants prior to the procedure. For the proof of concept, a fully sampled data set was acquired with an 8 channel head coil using a 3D-enhanced fast gradient-recalled echo sequence with monopolar gradients and the following parameters: 16 echoes, TR = 87 ms, FOV = 256mm, 256x256 matrix, readout bandwidth=31.56 KHz, flip angle 15°, 2mm slice thickness. The total acquisition time for acquiring 32 slices was approximately 18 min. The dataset was retrospectively undersampled by acceleration factors (R= 2,3,4,5,6) using the undersampling mask described above.

Later, prospectively undersampled data was acquired so that the utility of the proposed method could be tested in a more realistic scenario. Five volunteers (age 30 $\pm$ 3 years, 3 males and 2 females) were scanned. The sequence programming was done previously as a part of the project [187] to acquire prospectively undersampled data. As a part of this thesis, protocol optimisation was done to cater the sequence requirements. For this purpose, a 3D dataset was acquired using the same sequence and the following parameters (8 echoes, TR=57 ms, FOV= 256 mm, 160 slices, 192x192 matrix, readout Bandwidth= 13.56 KHz, flip angle 15°, 1.3 mm slice thickness). Due to the time constraint and the data storage limitation of the scanner, only eight echoes were acquired. The scanner by default reduced the scan time by acquiring an elliptical region of k-space, resulting in 136 actual phase-encodings instead of 192. Thus the actual acquisition time of the fully sampled scan was 136x160x57ms= 21 minutes. Accelerated datasets were acquired for different acceleration factors (R= 2,3,4,5,6) using this modified sampling mask, which is shown in Figure 4.2.

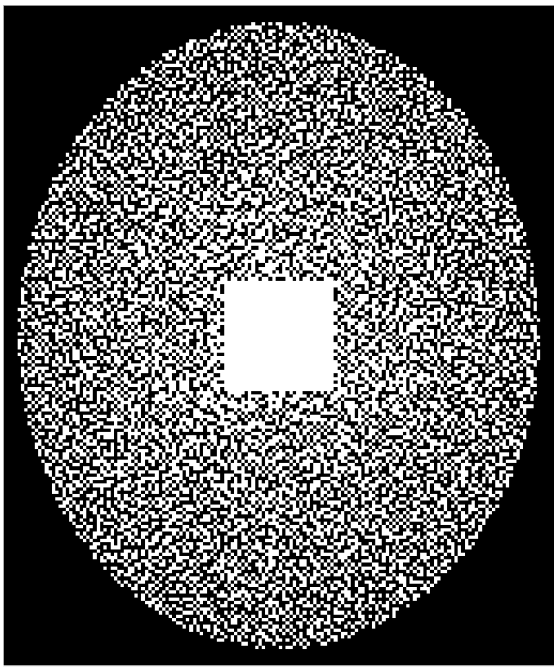

Figure 4.2: *(a) 2 times undersampled Poisson Disk Mask with the elliptical k-space sampling*

4.3.3 Image Reconstruction and Analysis

All algorithms were implemented in Matlab and reconstructions were conducted on a standard laptop with 4GB RAM and dual-core 2.60GHz CPU. The coil sensitivity maps were self-calibrated by averaging zero filled undersampled images over time and computed using the method described in [188]. The schematic diagram of the reconstruction pipeline is shown in Figure 4.3.

For retrospectively undersampled data, fully sampled data was multiplied by the binary masks with different accelerations. For prospectively undersampled data, co-registration and reslicing were applied using Statistical Parametric Mapping (spm-ttp://www.fil.ion.ucl.ac.uk/spm) to account for motion between the scans. As described before, a conventional SENSE was used to initialize the algorithm. Different values of parameters λ_1 and λ_2 were explored to find the optimum values. For this purpose, different values of λ_1 and λ_2 were tested, and the optimum values were selected. The value used for λ_1 was 0.5 and for λ_2 was 0.25.

To demonstrate that the coherent fitting improves the accuracy of the reconstruction, the proposed approach was compared to the magnitude-only fitting. To this end, the complex image was split into magnitude and phase, and Step (1) was updated from the magnitude image, and

later the phase was put back before Step (2) as used in Chapter 3. Root Mean Squared Error (RMSE) and Structural Similarity Index (SSIM) [189] was calculated between fully sampled and undersampled datasets for both coherent and magnitude-only fitting. The SSIM is considered a good approximation of perceived image quality and will provide an additional metric to evaluate the proposed method (see section 2.8).

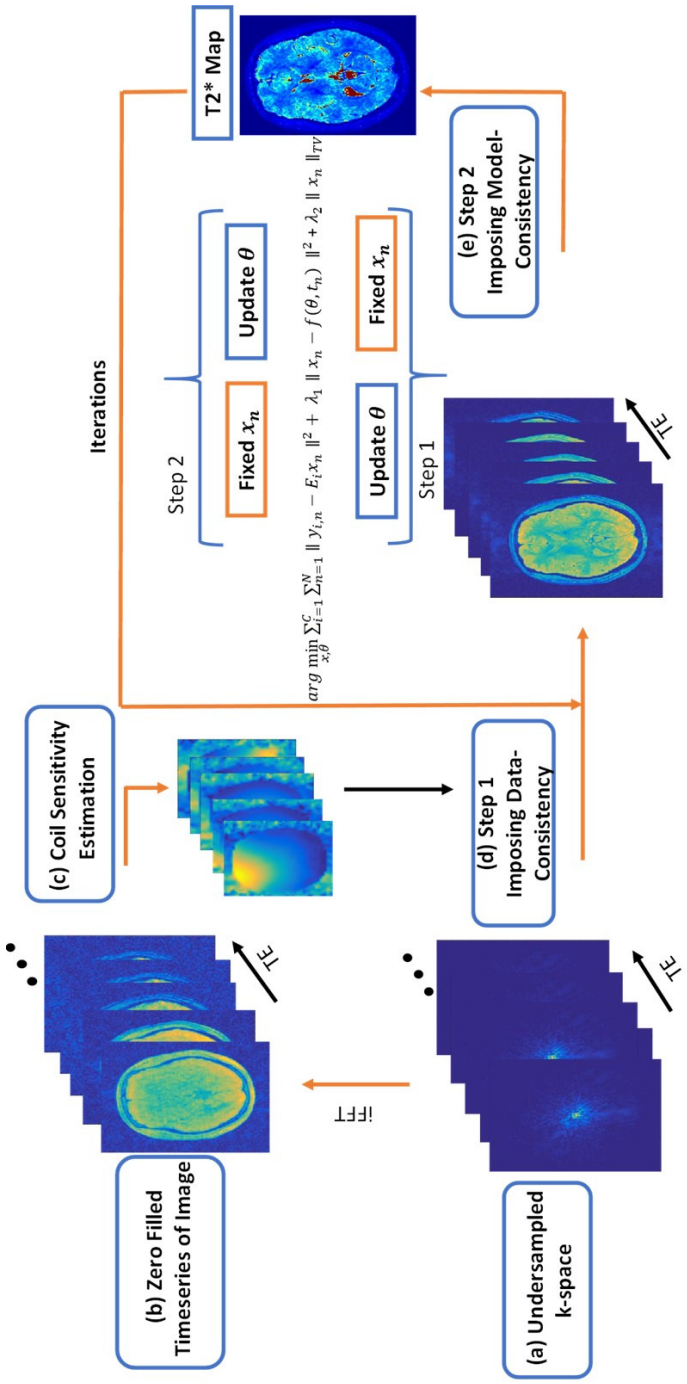

Figure 4.3: *The schematic flowchart of image reconstruction method a) undersampled k space data b) Zero filled image using inverse FFT c) Sensitivity Maps are estimated d) Using the sensitivity maps images the MLE based cost function is minimized by Alternating Minimization e) T_2^* maps (alongside other parameters in θ) are reconstructed, and the output is used for the Step 1 in an iterative manner.*

The proposed approach was compared with conventional PI reconstruction and alternative forms of regularization (e.g., l_1) for numerical phantom and in-vivo data. For this purpose, the proposed approach was compared with the SENSE reconstruction followed by NLS fitting. In addition,T_2^* maps were reconstructed by incorporating TV regularization with SENSE followed by NLS fitting.

ROI analysis was done on the fully sampled and the prospectively undersampled human datasets. ROIs were drawn in the frontal white matter, deep gray matter (Putamen), thalamus and corpus callosum. Mean and standard deviation of T_2^* values in the undersampled data were compared with the T_2^* values obtained from the conventional NLS fitting of the fully sampled data. To evaluate the consistency of T_2^* values across different datasets, ROI analysis was performed and the T_2^* values were compared across all the volunteers.

4.4 Results

Comparison between the coherent MLE (Figure 4.4) and magnitude-only (Figure 4.5) approaches for the numerical phantom with the T_2^* maps and the difference maps and RMSE are shown. For both the methods, the error increased smoothly with the increase in the acceleration factor. For R=2, the error is primarily in the CSF and around the edges of the skull-tissue interface. For higher acceleration factors, there is an overall increase in the error across the brain, which is reflected in higher RMSEs. However, for the magnitude-only approach, RMSE is greater compared with coherent MLE.

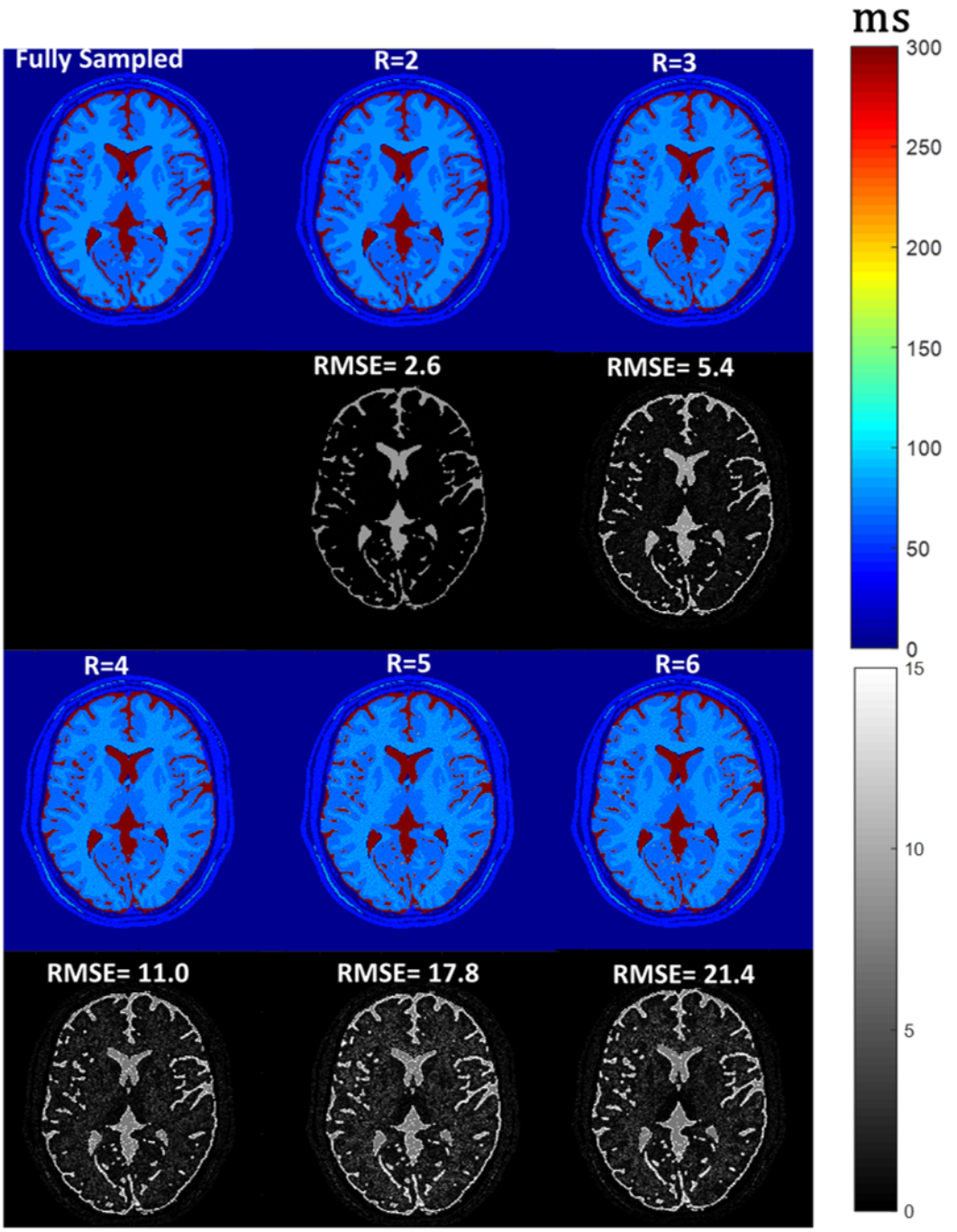

Figure 4.4: *T_2^* maps of the fully sampled and undersampled datasets of the brain numerical phantom reconstructed using coherent MLE are shown in the colored top rows. The corresponding difference of the T_2^* maps between fully sampled and the reconstructed maps from undersampled data are shown in the bottom rows with the RMSE. The colorbar represents T_2^* maps (top) and error (bottom) in ms.*

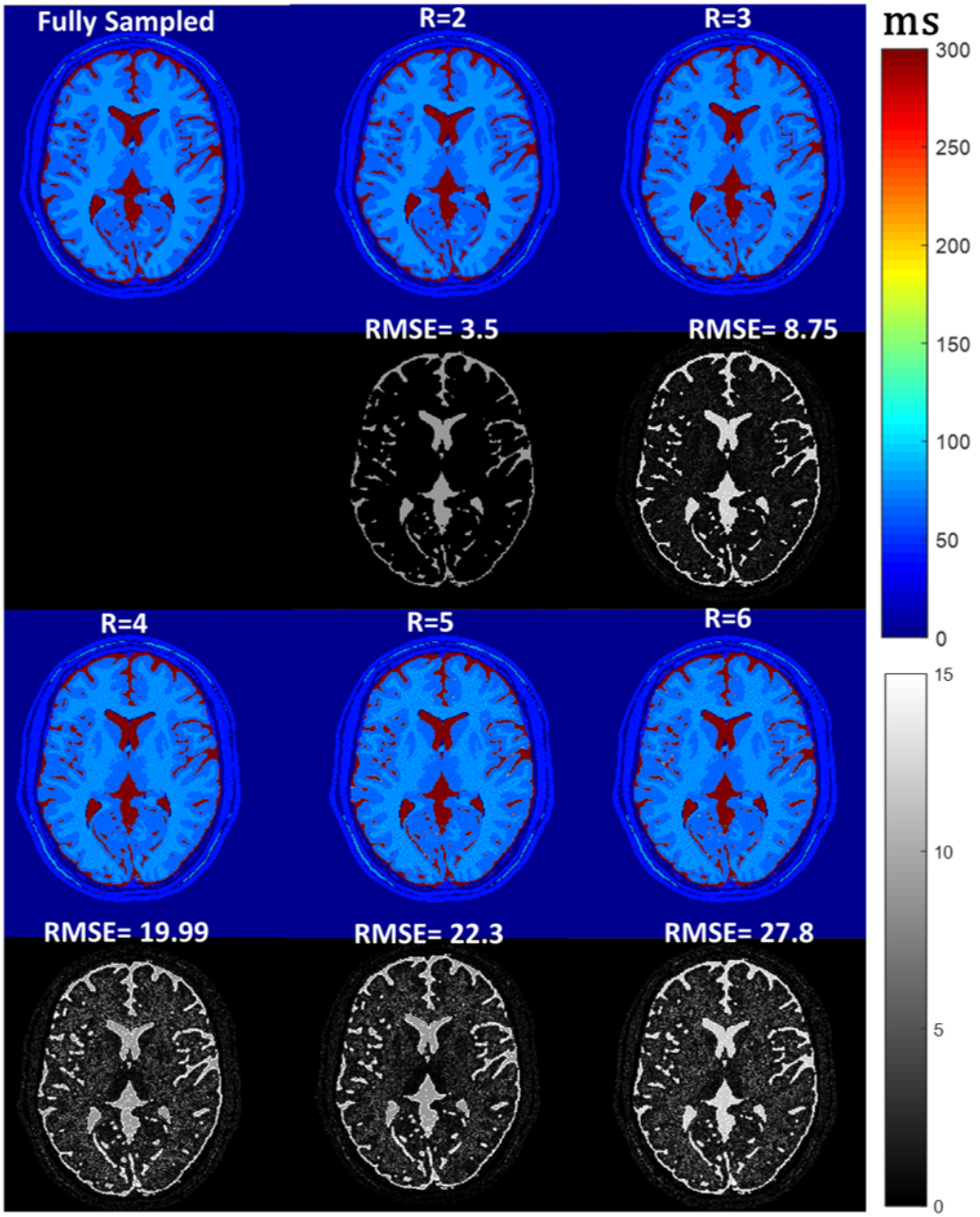

Figure 4.5: *T_2^* maps of the fully sampled and undersampled datasets of the brain numerical phantom reconstructed using magnitude-only and are shown in the colored top rows. The corresponding difference of the T_2^* maps between fully sampled and the reconstructed maps from undersampled data are shown in the bottom rows with the RMSE. The colorbar represents T_2^* maps (top) and error (bottom) in ms.*

As seen in the numerical phantom, errors are observed in CSF and skull in retrospective undersampling Figure 4.6 and 4.7 as well. However, magnitude-only shows much greater error even for the lowest acceleration factor when compared with the coherent MLE. In general, the accelerated images with coherent MLE have fewer artefacts than magnitude-only reconstruction, which is reflected in the respective RMSEs as well.

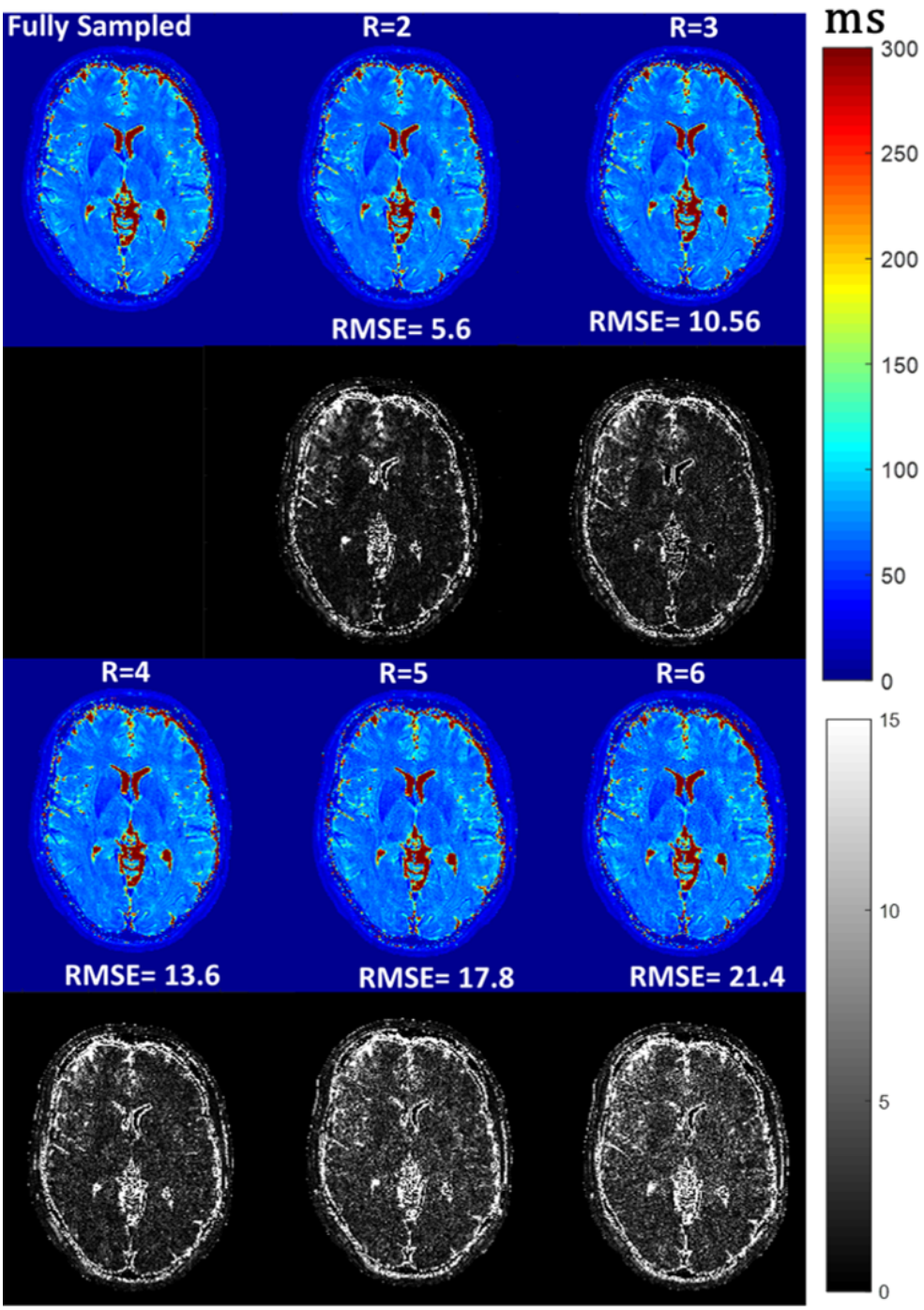

Figure 4.6: *Coherent MLE: T_2^* maps of the fully sampled and undersampled datasets of healthy volunteer with retrospective undersampling (Top row). The corresponding difference of the T_2^* maps between fully sampled and the reconstructed maps from undersampled data are shown in the bottom rows with the RMSE. The colorbar represents T_2^* maps (top) and error (bottom) in ms.*

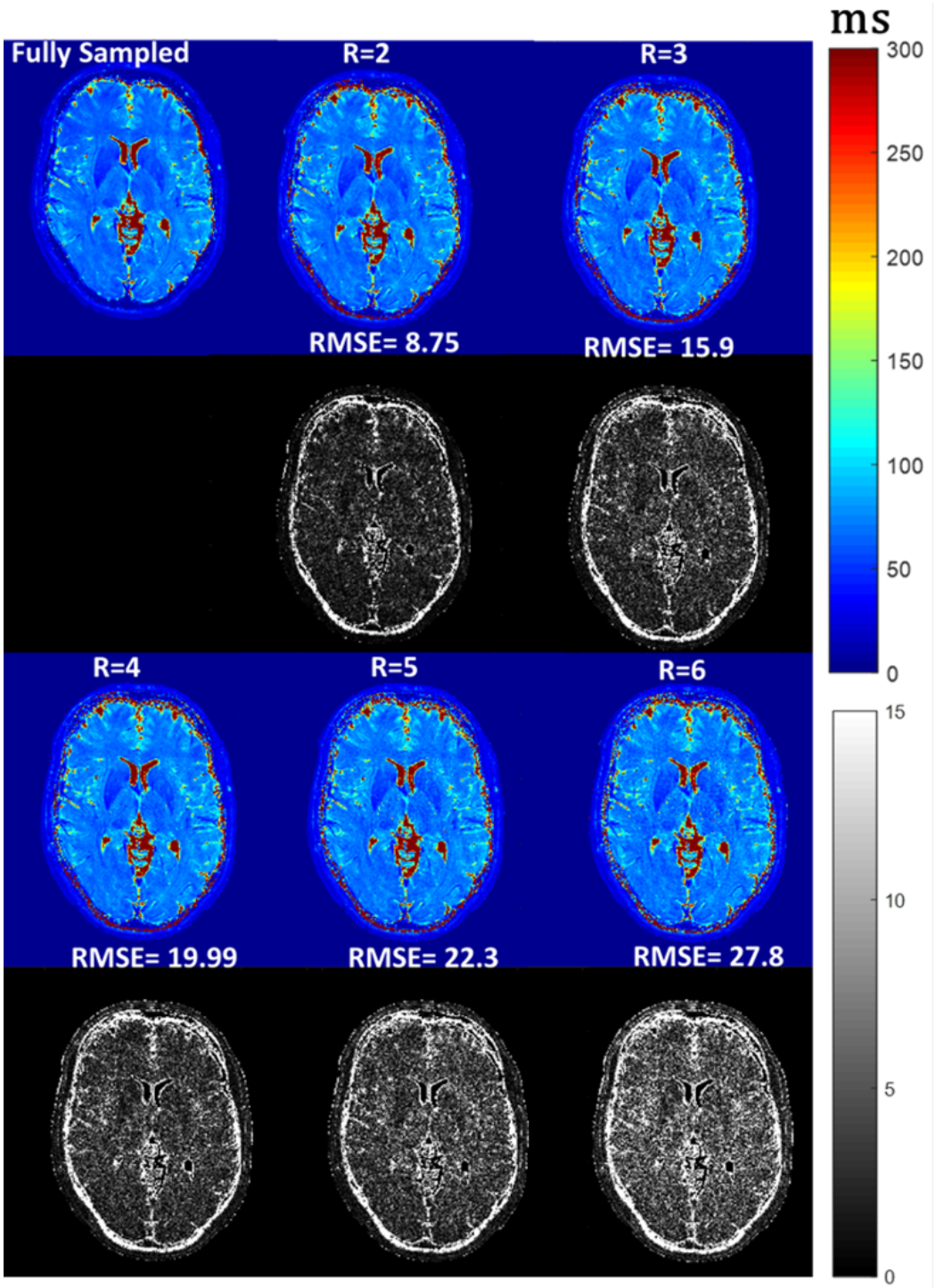

Figure 4.7: *Magnitude-ony: T_2^* maps of the fully sampled and undersampled datasets of healthy volunteer with retrospective undersampling (Top row). The corresponding difference of the T_2^* maps between fully sampled and the reconstructed maps from undersampled data are shown in the bottom rows with the RMSE. The colorbar represents T_2^* maps (top) and error (bottom) in ms.*

For prospective undersampling, slight motion artifacts are visible in some accelerated images as seen in Figure (4.8,4.9). As observed before, the coherent MLE approach shows less error when compared with the magnitude-only reconstruction. Overall for all the datasets, the coherent MLE gave better T_2^* maps with less error (approx 20 % better) than the magnitude-only reconstruction.

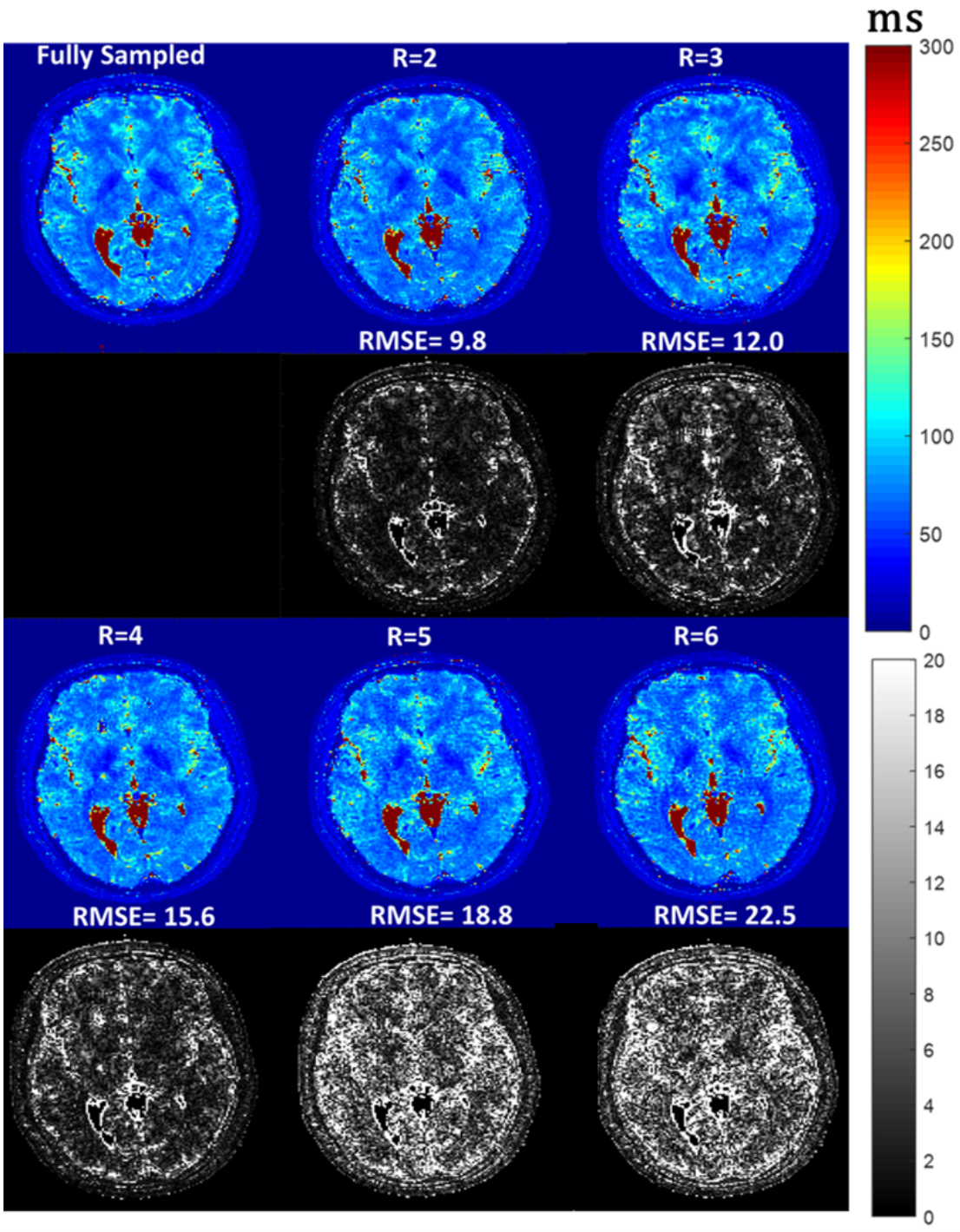

Figure 4.8: *Coherent MLE reconstruction from the fully sampled dataset of healthy volunteer with prospective undersampling. T_2^* maps reconstructed from coherent MLE demonstrated less error as seen in the difference image. Whereas, the magnitude-only reconstruction showed increased over-all error with higher RMSEs as well. The colorbar for T_2^* maps (top) and error (bottom) in ms.*

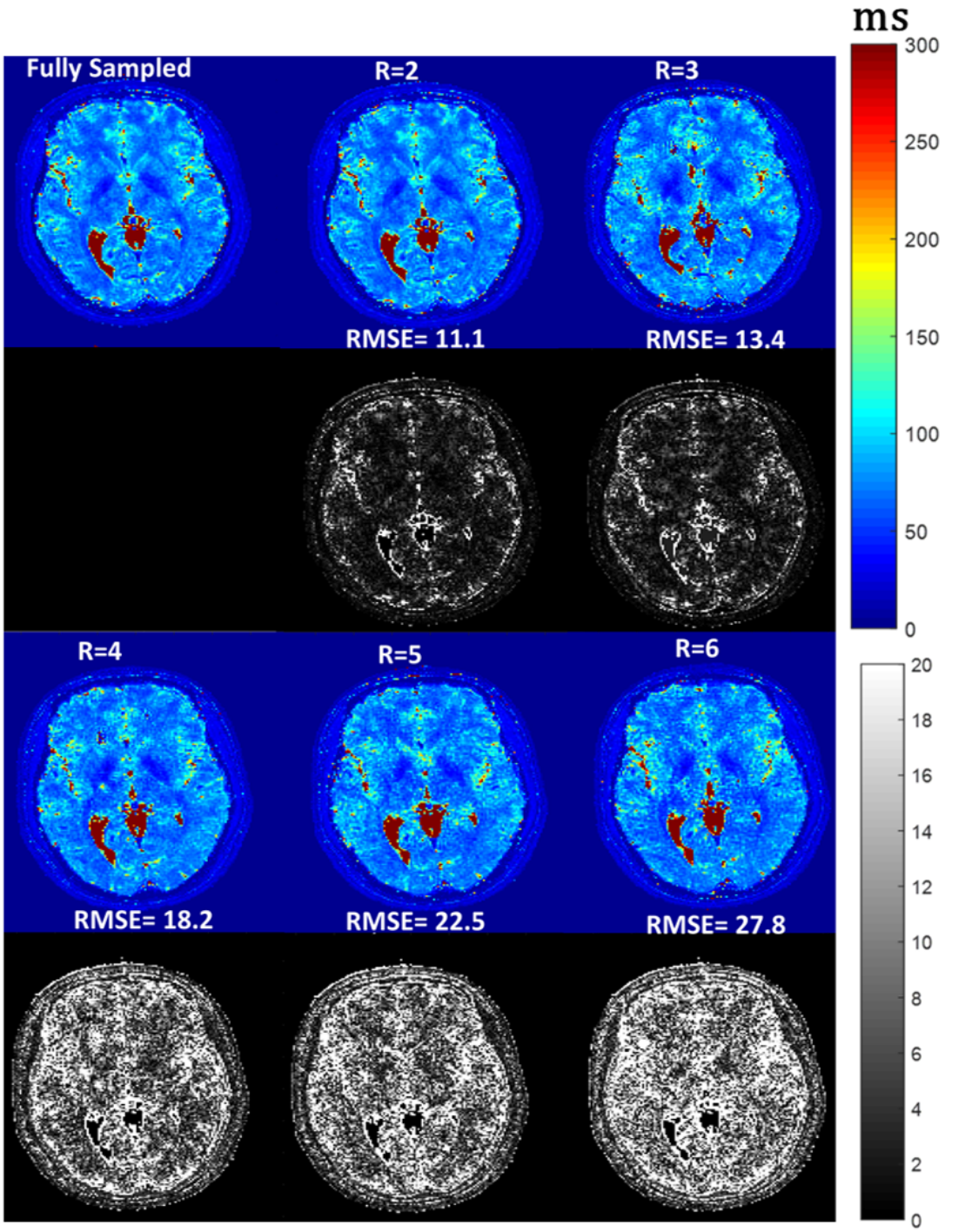

Figure 4.9: *Magnitude-only reconstruction from the fully sampled dataset of healthy volunteer with prospective undersampling. T_2^* maps reconstructed from coherent MLE demonstrated less error as seen in the difference image. Whereas, the magnitude-only reconstruction showed increased over-all error with higher RMSEs as well. The colorbar for T_2^* maps (top) and error (bottom) in ms.*

In addition to the RMSEs, the SSIM also indicates that the coherent MLE approach is more accurate in parameter estimation as compared to magnitude-only approach. As expected, for all the three cases, the SSIM decreases as the acceleration factor increases. However, for the prospective undersampling, the SSIM decreased substantially for the acceleration factor of 5 (approx 0.6) and 6 (approx. 0.5). The SSIM for different acceleration factors and different set of data is show in Figure 4.10 and Table 4.2.

	SSIM				
	2	3	4	5	6
Numerical Phantom					
Magnitude	0.87	0.84	0.80	0.78	0.75
Complex	0.85	0.82	0.79	0.77	0.73
Retrospectively Undersampled					
Magnitude	0.95	0.93	0.91	0.87	0.83
Complex	0.93	0.92	0.87	0.84	0.82
Prospectively Undersampled					
Magnitude	0.87	0.82	0.74	0.62	0.55
Complex	0.85	0.79	0.73	0.60	0.52

Table 4.2: *SSIM values for different acceleration factors*

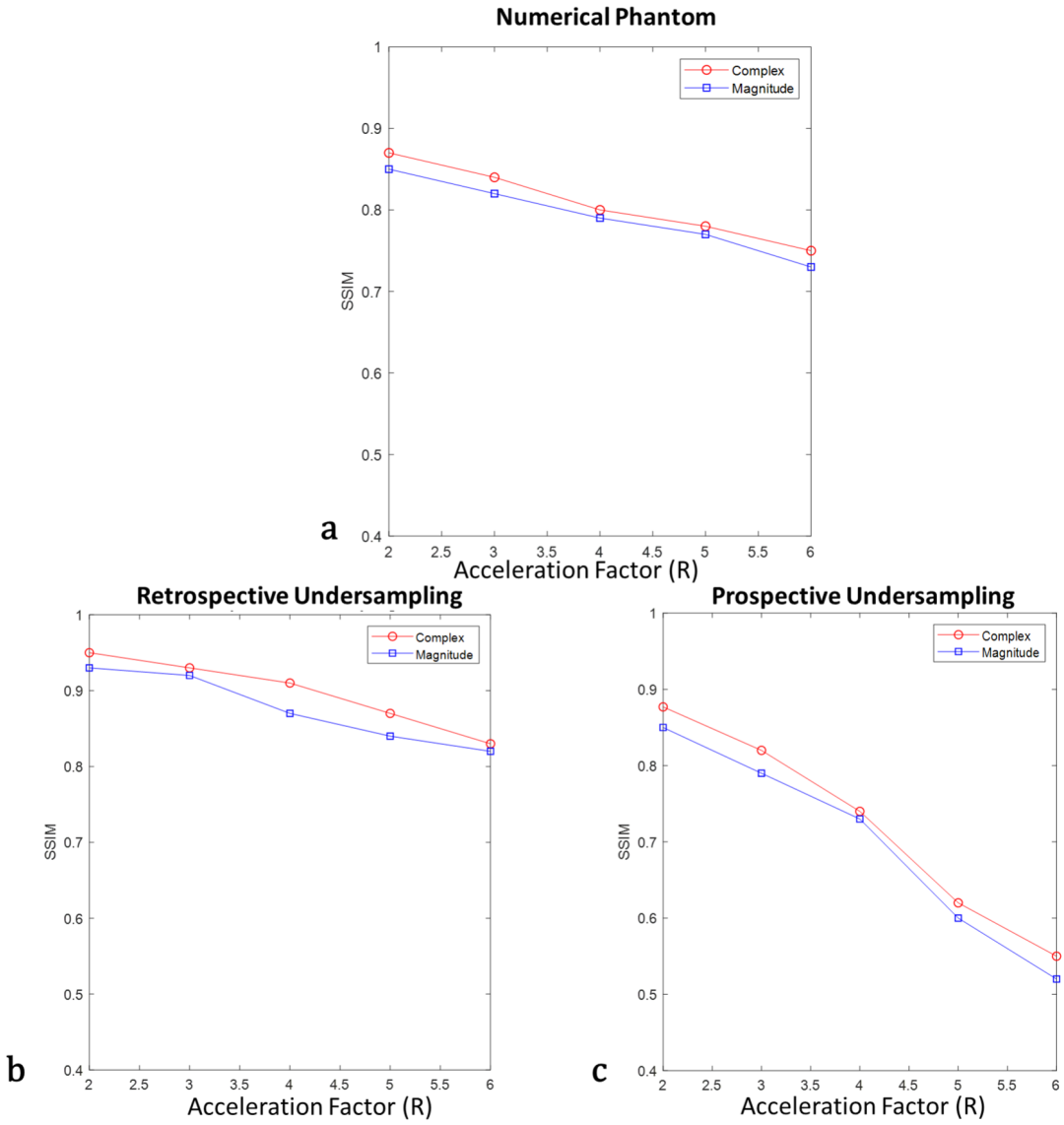

Figure 4.10: *Graph demonstrating the SSIM for coherent MLE and magnitude only-reconstruction for different acceleration factors R (a) Numerical Phantom (b) Retrospective Undersampling (c) Prospective Undersampling. For all the datasets, coherent MLE showed better SSIM as compared to magnitude only.*

As described before, the coherent MLE estimates four parameters. The parameters estimated from in-vivo human data are shown in Figure 4.11 for an acceleration factor of 2. The figure demonstrates the Proton Density (ρ), coil phase (φ) and the frequency map (ω). Qualitatively, the T_2^* map shows no undersampling artifacts and the T_2^* values are in agreement with the known T_2^* values of brain as per literature the [51]. The field map shows the variation in the precessional frequency, which appears to be variable in the frontal and lateral sides of the brain.

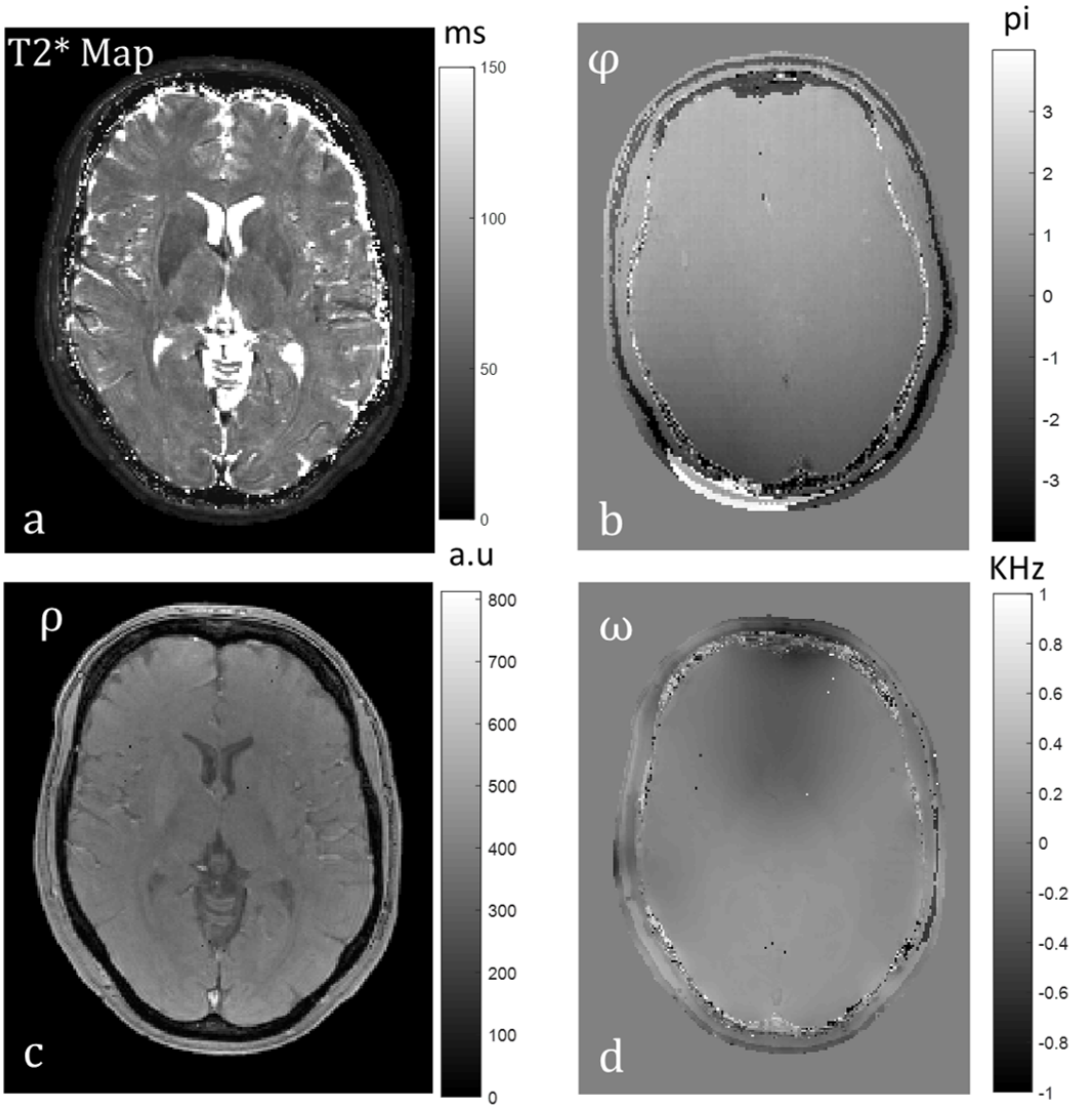

Figure 4.11: *Reconstructed parameters using coherent phase-fitting approach for R=2: a) T_2^* Map b) Constant phase from coil sensitivities c) Proton density ρ d) Frequency map*

Comparison between the proposed approach, SENSE only and SENSE + TV reconstruction showed that incorporating the model information in the reconstruction aided in improving the reconstruction (Figure 4.12). SENSE only reconstruction showed visible artefacts due to the undersampling as no prior information from the model was incorporated. For SENSE + TV reconstruction, the undersampling artefacts are eradicated. However, there is residual noise present with some overestimation of T_2^* values in the healthy brain. Nevertheless, the proposed approach results in improved reconstruction as compared to the other methods.

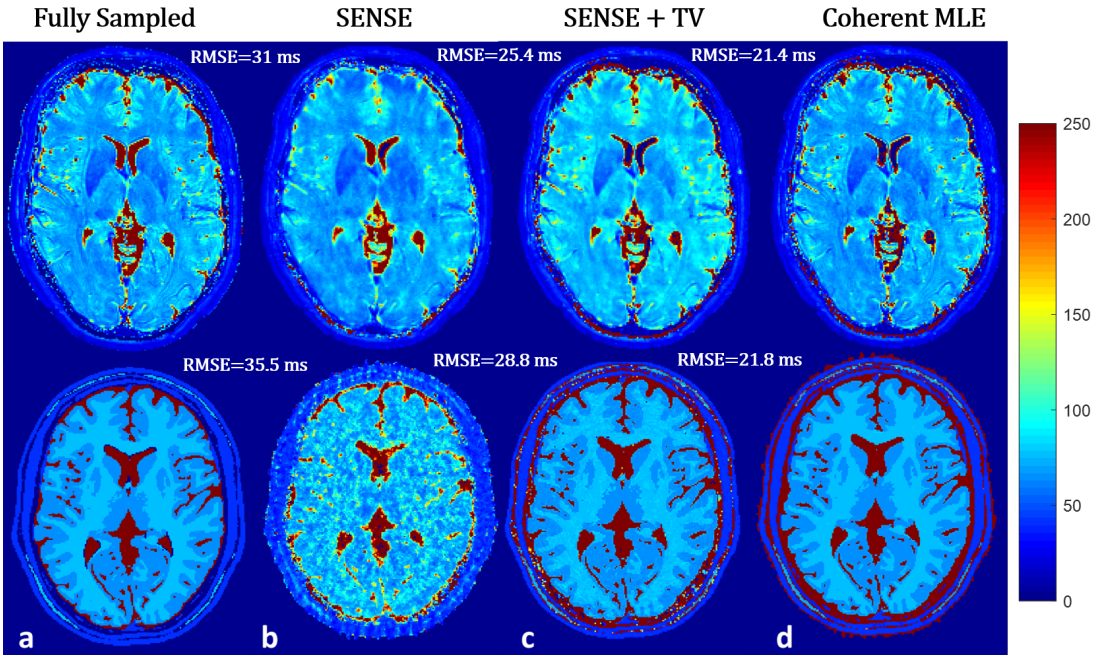

Figure 4.12: *Reconstructed T_2^* maps from healthy volunteer (upper row) and numerical phantom (bottom row) for (a) fully sampled dataset and undersampled dataset (R=6) reconstructed with (b) SENSE (c) SENSE + TV (d) Coherent Parallel MLE.*

Registration of the fully sampled and the undersampled data helped in reducing the error further for both approaches. With the registration, brain structures were more discernible (Figure 4.13a) and also reduced the error (Figure 4.13b) that may have occurred due to the motion between scans.

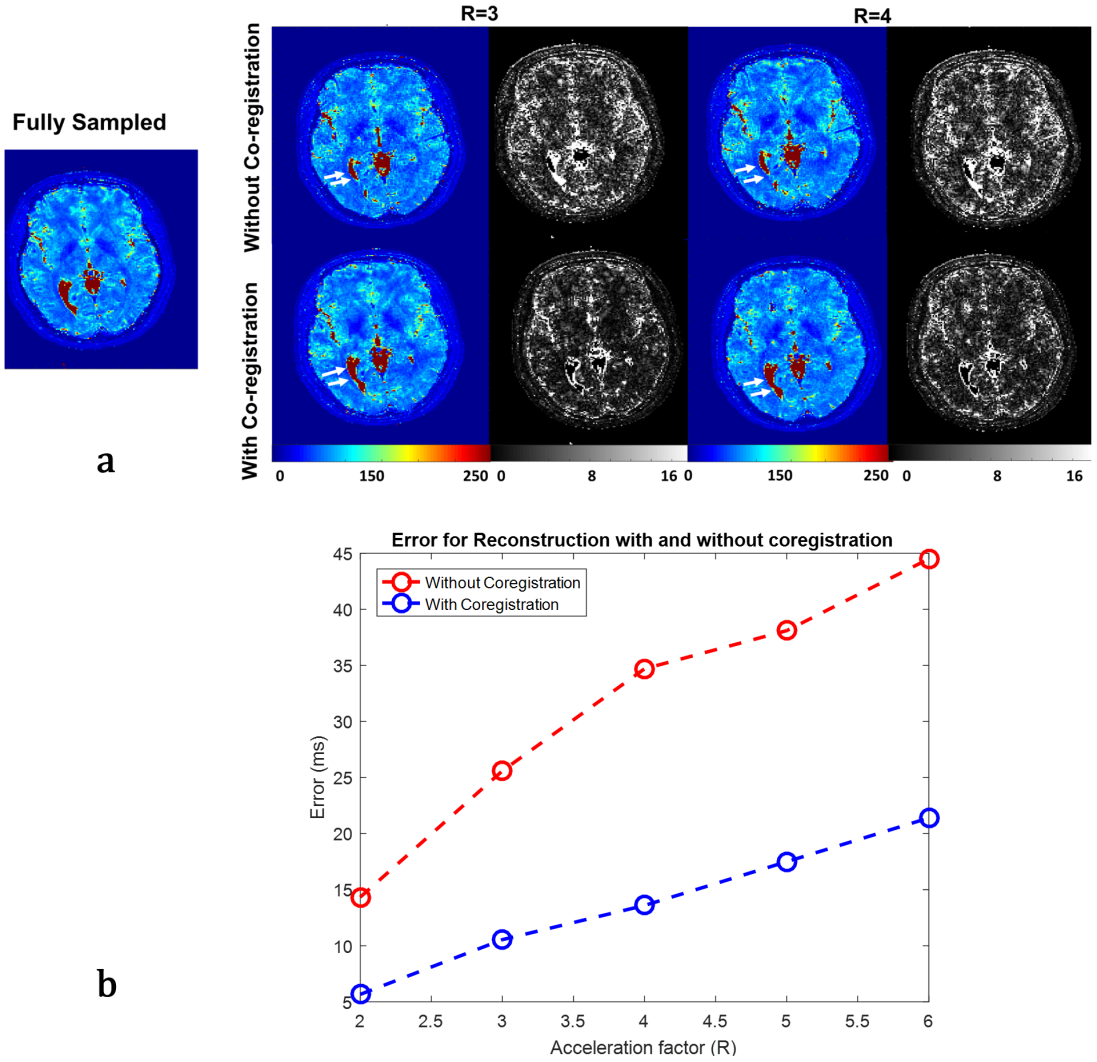

Figure 4.13: *(a) Reconstructed T_2^* maps of the fully sampled dataset of a healthy volunteer with prospective undersampling (R=3 and 4) reconstructed with and without co-registration. The corresponding difference images are shown with the maps. The movement between the scans is evident from the position of the ventricle (black arrow). (b) The graph shows the RMSEs between fully sampled and the under-sampled T_2^* maps with co-registration and without co-registration. The error is reduced significantly by co-registration resulting in better delineation of grey and white matter.*

One volunteer dataset out of five was excluded from the analysis due to severe motion artifacts. ROI analysis across four volunteers for the prospective undersampling demonstrated that in-

creasing the acceleration factor leads to higher standard deviation Table 4.3. An example of a 3D T_2^* volume reconstructed with the proposed approach is shown in (Figure 4.14a). The 3D volume helped in drawing the ROI in all three slice orientations, and the T_2^* values across all the volunteers is shown in (Figure 4.14b). The T_2^* values found in the four regions were consistent across subjects, showed low variability, and were consistent with the literature values.

Regions	**Fully Sampled**	**Undersampling Factor**				
		R=2	**R=3**	**R=4**	**R=5**	**R=6**
Frontal White Matter	64± 3	64 ± 7	65 ± 9	65 ± 8.9	64.5 ± 9.3	66 ± 11
Thalamus	64 ± 6	64± 7	65 ± 8	65 ± 8.9	66.5 ± 7.3	70 ± 8.0
Deep Gray Matter	42 ± 7.8	42 ± 8.4	43 ± 9.4	44 ± 9.1	45 ± 10.0	45 ± 13.2
Corpus Callosum	69 ± 10	66 ± 11	65 ± 13	67 ± 15	68 ± 13	68 ± 18

Table 4.3: *Mean and standard deviation of the T_2^* values (ms) in four regions of a healthy volunteer for fully sampled and undersampled data with prospective undersampling.*

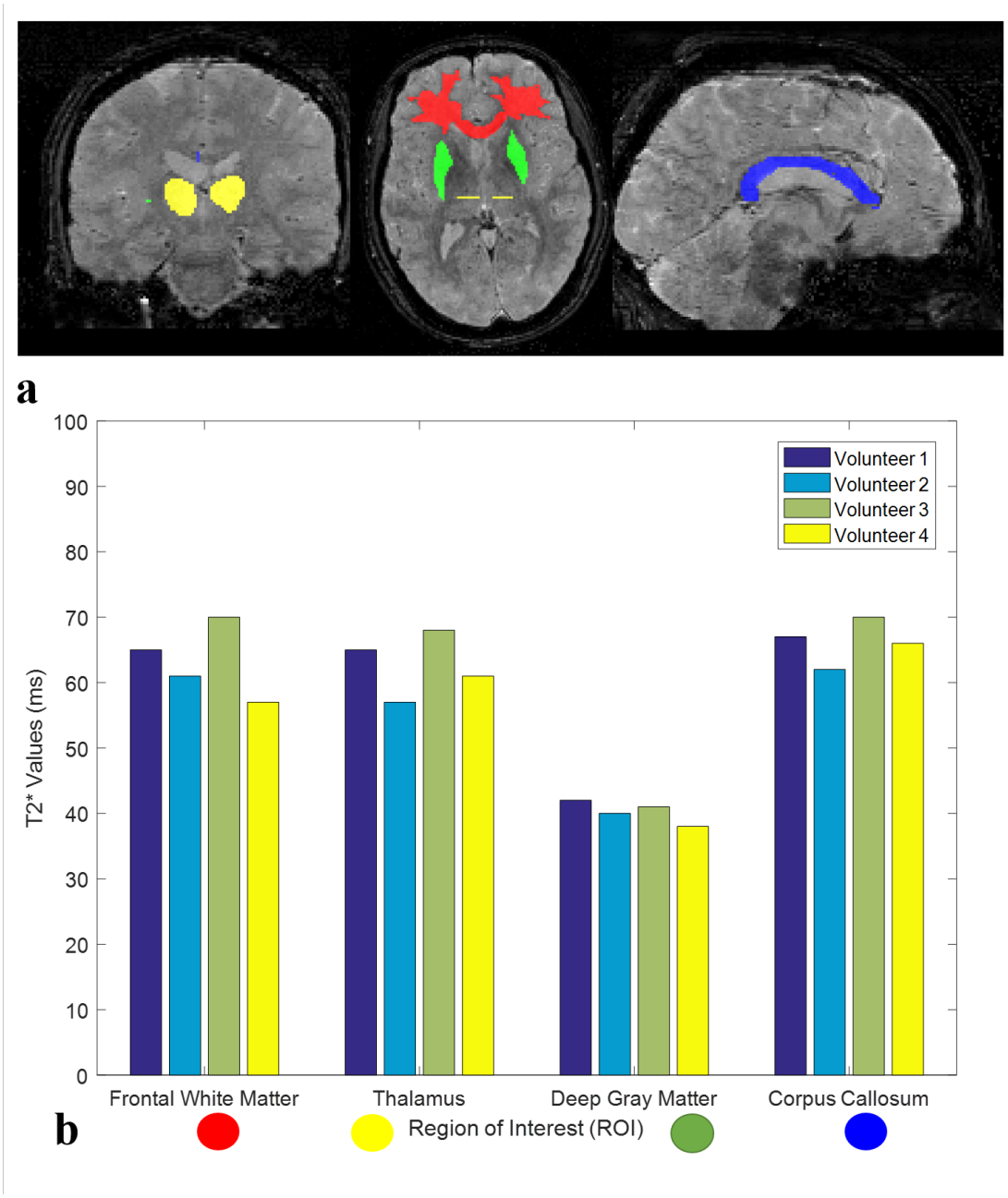

.

Figure 4.14: *(a) 3D volume reconstruction of a volunteer with different ROIs drawn across the volume. (b) The bar graph shows the estimated T_2^* values from all the ROIs across four volunteers for R=4*

4.5 Discussion

The quantification of tissue parameters from MRI datasets is emerging as a powerful tool for tissue characterization. However, the long scan times associated with the parametric mapping reduces its utility for clinical applications. A common approach to reducing the scan time is to limit the number of weighted images from which the parameters are estimated. However, this approach precludes the use of multi-exponential fitting, limits the solution accuracy, and restricts the dynamic range of estimated tissue parameters. In addition, exponential fitting in the magnitude image poses a bias in the estimation due to the incorrect noise model. While previous works have addressed this issue by correcting for the noise model or by performing fitting in the complex domain, no previous work has explored the potential in undersampled acquisitions. Our approach addresses these issues in an undersampled case and demonstrates that incorporating the complex data can result in better denoising and reduced error.

In contrast to other models presented in the literature, we propose to work directly with complex-valued images. As demonstrated in the numerical phantom and the in-vivo brain datasets, the coherent MLE results in less error across different acceleration factors. Although the number of estimated parameters is increased in coherent fitting, it outperforms the magnitude-only approach. In general, for both approaches, the CSF was a source of overall increased error. This can be attributed to the fact that CSF has a higher T_2^* value (approx 2000ms) and the acquisition protocol does not account for very high T_2^* values.

As an additional benefit, the proposed approach estimates the parameters that are related to the magnetic field inhomogeneity. The parameter ω in equation 4.1 is the change in precessional frequency, which occurs as a result of the magnetic field inhomogeneity. A field map can be extracted from this parameter according to the relation [51]

$$\Delta\omega = \gamma \Delta B_0 \tag{4.8}$$

where γ is the gyromagnetic ratio and ΔB_0 is the magnetic field inhomogeneity. A magnetic field map along with the T_2^* mapping can be useful in quantitative susceptibility studies that subsequently have application in studying brain iron concentration [190].

With the real time undersampling and the healthy volunteers' study, the feasibility of the approach in a realistic setting was evaluated as well. SSIM indicated that the T_2^* maps for the acceleration factors greater than four had very suboptimal quality. The scan time for this was

seven minutes, which is suitable for clinical studies. Since the individual scan times for all the undersampled datasets were long, the motion of the subject during a scan is a possibility. It is important to mention two significant works for model-based reconstruction of the related T_2 mapping from undersampled data by Block et al. [183] and MARTINI by Sumpf et al. [66]. Both approaches use real-valued data and hence are not directly applicable in our context. It might be possible to modify their approaches and map the off-resonance by replacing the relaxivity with a complex-valued parameter and adjusting the gradient of the cost function accordingly. This would provide an alternative approach to optimizing equation 4.6. However, we leave this for future study.

For the retrospectively undersampled data, additional noise was not introduced. When data is retrospectively undersampled without adding noise, the noise that was in the original data becomes part of the 'true' signal and this might not reveal issues related to poor conditioning of the inverse problem. The prospectively undersampled data doesnot have this problem which was included in the present work and showed similar results. The regularizer plays an important role in minimization of the cost function for the proposed method. A small value of λ_1 makes the model-consistency less effective, whereas a higher value can bias the solution away from the data fidelity. Similarly, a high value of spatial regularizer λ_2 can overly smooth the image and obscure the small details. In this work, both regularizers were chosen empirically and were fixed for all the undersampled datasets. The choice of the regularizer values can be made automatic and robust using methods like the L-curve method [191]. Estimating two additional parameters from the complex-valued signal increased the complexity of the model which subsequently led to the longer computational time. For the current study, the mono-exponential model was chosen for the optimization whereas realistically the images may follow a multi-exponential decay. Future studies can be extended to encompass multi-exponential models.

4.6 Conclusions

This Chapter was an extension to the Chapter 3 which proposed a method for accelerating T_2^* mapping based on the magnitude image. However, the method had certain limitations that were addressed in the current work. The proposed method in this Chapter allowed the reconstruction of the T_2^* maps from undersampled data by combining the multicoil information with coherent phase fitting. This approach extends the acceleration attained in PI to parameter estimation by imposing the exponential relaxation directly in the complex signal domain. When compared to

magnitude-only fitting, the coherent MLE resulted in less error. The results were consistent in both retrospective and prospective undersampled data sets as well as across different subjects. The implementation of this approach on the scanner will make it feasible for clinical scenarios.

Chapter 5
High-resolution Isotropic Whole Brain T_2 Mapping with Model-based Super-resolution Reconstruction

5.1 Introduction

Conventionally, T_2 is measured by sequentially acquiring several spin-echo (SE) images, each with different echo time (TE) and subsequently fitting a mono-exponential decay. This is commonly acknowledged as a gold standard despite residual diffusion effects affecting the T_2 quantification. Nonetheless, the long acquisition time is impractical for most clinical applications. As an alternative approach, the multiple-echo spin-echo (MESE) sequence in the Carr-Purcell-Meiboom-Gill (CPMG) condition [65] uses multiple refocusing pulses to acquire multiple echoes for each excitation, reducing the total acquisition length. However, the quantitative accuracy of the sequence is compromised by imperfect refocusing. The imperfect refocusing results in the formation of stimulated (secondary) echoes that disrupt the T_2 decay of the spin (primary) echoes [192]. The effect of the stimulated echoes can be reduced by ignoring the first echo while fitting the relaxation curve [66]. However, it has been shown that skipping echo approaches still yield highly variable results that depend on flip angle, T_2, and echo train length [193]. Therefore, more complex signal models are required to accurately estimate T_2 [192].

The ability to accurately and precisely map T_2 at high-resolution (e.g. 1-mm^3 isotropic voxel size) in large volumes may help to improve the quantification of small focal changes such as multiple sclerosis lesions or brain areas causing focal seizure onset in epilepsy. However, using thin-slices in a 2-D MESE acquisition is challenging due to the reduced SNR. Furthermore, RF pulses with long duration are required to excite thin slices leading to longer echo-times spacing ($\triangle$TE) [148]. The increased change in TEs makes accurate quantification of short T_2 values difficult. In addition, true T_2-weighting is difficult to obtain in reasonable acquisition times with 3-D acquisition methods since a long TR is required to fully recover the magnetization to

equilibrium between excitations. Since all the spins are excited by every pulse, the recovery time cannot be used for interleaved slice sampling, rendering the sequence less efficient [15]. Furthermore, a 3D acquisition is also limited by the SAR safety constraints. A large amount of power is deposited if multiple non-selective 180° pulses are used which can easily exceed the SAR limits [81].

A fundamental consideration in any MRI experiment is to optimally balance image resolution, SNR and acquisition time. Various methods have been published to accelerate quantitative mapping methods, for example using model-based reconstruction [66, 105, 131, 137], low-rank approaches [125, 194] or sparsity constraints [124, 179] from highly undersampled acquisitions. However, these methods experience a low SNR and use the low spatial resolution to counteract this effect. It has been shown that super-resolution reconstruction (SRR) provides a better trade-off between acquisition time, spatial resolution and SNR [15, 148] (also see section 2.7.2). SR was initially proposed in structural and diffusion MRI where high resolution images were reconstructed from a set of low-resolution (LR) images [195]. The resolution is enhanced by acquiring multiple low-resolution images with a shift of the field of view (FOV) in the slice direction [15], three orthogonal slice orientations [163] or rotated slice orientations [196] and subsequently combining the images by solving a non-linear inverse problem. The acquisition methods have been discussed in detail in section 2.7.3. In quantitative MRI, SR reconstruction benefits from combining the parametric model with the SR model. This has been shown in T_1 mapping [170] where the relaxation model was combined with the SR model allowing the direct estimation of a high-resolution T_1 map from low-resolution images. However, the acquisition of multiple LR images results in long scan times (TA $>$ 20 mins), hence limiting its use for clinical applications.

Both the SR and model-based reconstructions are based on solving an inverse problem using iterative optimization methods. This Chapter investigates the combination of SR and model-based reconstruction to exploit the respective advantages (i.e., high resolution and fast acquisition time) in the application of quantitative T_2 mapping. The proposed method is based on multiple 2-D MESE acquisitions, which were highly undersampled to compensate for prolonged scan time. The method was tested on a phantom and four healthy volunteers. An early version of this framework was presented at the Annual Meeting & Exhibition of the ISMRM in 2017 and 2019 [197, 198]. A full journal version has been accepted in MRM and that the experimental part of this work was done during a research visit to Siemens Healthineers, EPFL.

5.2 Theory

SR reconstruction is a method to obtain a high-resolution (HR) image from a series of LR images, where each LR image is acquired with a different FOV or orientation. Each FOV or orientation can be expressed as a different geometric transform T_j (with $j = 1, \ldots, J$, and J the number of transformations) from the HR image to the LR image. The different FOV or orientation can be expressed as a geometric transformation T from the HR image to the LR image. The resolution is enhanced since the different FOV or orientations contain complementary resolution information. The reconstructed HR image benefits from the high SNR of the LR images, which are typically acquired with a high in-plane resolution and a low through-plane resolution, i.e. thick slices. Let x_n (with $n = 1, \ldots, N$, and N the number of spin-echoes) represent a HR T2-weighted series of vectorized images and $y_{j,n,c}$ (with $c = 1, \ldots, C$, and C the number of coils) be the undersampled LR k-space measurements acquired with a MESE sequence. The acquisition of the undersampled LR $y_{j,n,c}$, can be modelled by:

$$y_{j,n,c} = PF\{S_{j,c} \downarrow T_j x_n\} + \eta_{j,n,c}, \tag{5.1}$$

where Tj is the geometric transformation representing a rotation or translation of the FOV (Figure 1), $\downarrow$ is a down-sampling operator that maps the resolution to LR grid, $S_{j,c}$ complex coil sensitivities calculated separately for each transformations, F the forward discrete Fourier operator and P is a binary under-sampling mask. According to [171] the noise $\eta_{j,n,c}$ in MRI can be assumed to be additive, white and Gaussian when the SNR > 3, and this is what we assume here. The high-resolution image x_n can be estimated by solving the inverse problem of equation 5.1:

$$\arg\min_x \sum_n^N \sum_c^C \sum_j^J \|PF\{S_{j,c} \downarrow T_j x_n\} - y_{j,n,c}\|^2, \tag{5.2}$$

where the choice of the least squares criterion is motivated by the assumption that the noise is Gaussian distributed. The greater number of acquisitions, J, with complementary information of the same object that are acquired the better conditioned the problem becomes. The problem stated in equation 5.2 is ill-posed due to the down sampling operator, because several different combinations of intensities in the high-resolution image can lead to the same intensity in the low-resolution image. In order to better condition the problem, more J sets of LR k-space measurements are required using either a different FOV or orientation with the corresponding spatial mapping T_j to the high-resolution image x_n. To further improve the conditioning of

the problem, we can incorporate a signal model into the cost function. Given the task of T_2 quantification, it is natural to use the physical constraints imposed across the sequence of images, x_n to further regularize the optimization. The signal model with the echo time (t_n) is typically described with a mono-exponential decay depending on the relaxation time T_2 and proton density ρ:

$$x_n = \rho.exp(-t_n./T_2), \tag{5.3}$$

where the above equation represents the pixel-wise scalar non-linear function for PD and T_2 and t_n being the echo time, even with ignoring the first echo, the standard exponential fitting will result in an overestimation of T_2 [193]. However, to accurately fit the data requires a more complex model that includes effects such as the $B1^+$ field, slice profiles, multiple T_2 compartments, diffusion and magnetization transfer. Since the present work aims at a proof of concept for super-resolution for T_2 mapping, the common approach of ignoring the first echo is used because of its simplicity and easy implementation.

The most intuitive step might be to substitute the HR image x_n in equation 5.2 with the signal-model equation 5.3 and solving directly for PD and T_2, resulting in the following cost-function:

$$\underset{T_2,\rho}{\arg\min} \sum_{n}^{N} \sum_{c}^{C} \sum_{j}^{J} \|PF\{S_{j,c} \downarrow T_j(\rho.exp(-t_n/T_2))\} - y_{j,n,c}\|^2, \tag{5.4}$$

However, minimizing equation 5.4 often requires special techniques such as gradient scaling and repeated restarts of the optimization algorithm to achieve a fast convergence [66, 69]. Therefore, in this work, we rather formulate the minimization problem as:

$$\underset{T_2,\rho,x_n}{\arg\min} \sum_{n}^{N} \sum_{c}^{C} \sum_{j}^{J} \|PF\{S_{j,c} \downarrow T_j x_n\} - y_{j,n,c}\|^2 + \lambda \|x_n - \rho.exp(-t_n./T_2)\|^2, \tag{5.5}$$

Where the first term ensures data-consistency of the HR image with the acquired data as in equation 5.1 and an additional term that ensures model-consistency i.e. forces the signal intensities to decay exponentially across the different echoes N. The slice profile has not been incorporated in the data-consistency term as it lead to a non-convex optimization and highly depends on the choice of deconvolution kernel in the inverse operation. Furthermore, the CPMG sequence employs different RF-pulses (90° and 180°) with different slice profiles. Therefore, the profile cannot be simply approximated by a Gaussian function. In order to balance between

the data- and model-consistency a regularization parameter λ is introduced. The above cost function in equation 5.5 can be minimized using a split algorithm that estimates quantitative T_2 by minimizing data- and model- consistency terms alternately [199]. By fixing T_2 and ρ, solving equation 5.5 with respect to x_n amounts to a standard linear least squares problem with a closed form solution. On the other hand, for solving equation 5.5 fixing variable x_n corresponds to fitting a mono-exponential decay onto x_n using Matlab's NLS solver, intrinsically estimating T_2 and ρ.

5.3 Methods

5.3.1 Numerical Simulation

Numerical noiseless T_2 and PD maps were generated from segmentation of grey matter, white matter and cerebrospinal fluid (CSF) in a single axial slice (1x1 mm^2 resolution) of a numerical phantom [200]. For the three main tissues the following T_2, values were used: 0.1 s for grey matter, 0.06 s for white matter and 2 s for CSF [51]. From these maps, T_2-weighted HR images x_n were simulated, each with equidistant TEs [TE=10...,160 ms]. The T_2-weighted images were down sampled to the desired low-resolution using equation 5.1 and different transformations T_j. Complex coil sensitivities for each of these transformations were simulated using the Parallel MRI noisy phantom simulator [186]. Assuming that our reconstruction problem is split into multiple 2D problems, a single axial slice of the phantom was suitable for simulation purposes. Therefore, for the phantom, we can assume a sagittal acquisition with phase-encoding in Anterior-Posterior and slice-encoding in Left-Right. Three different types of transformations were tested: linear (where the images were shifted along the slice direction), orthogonal (images were rotated to two orthogonal rotations 0 degree and 90 °) and diagonal (two orthogonal rotations plus two rotations at 45 ° and -45°). An illustration of the different transformations is shown in Figure 5.1. The images were transformed to k-space and then undersampled by a factor of 10 with a mixed parallel imaging and block undersampling pattern described in [3]. The HR images were reconstructed with the proposed SR model-based reconstruction.

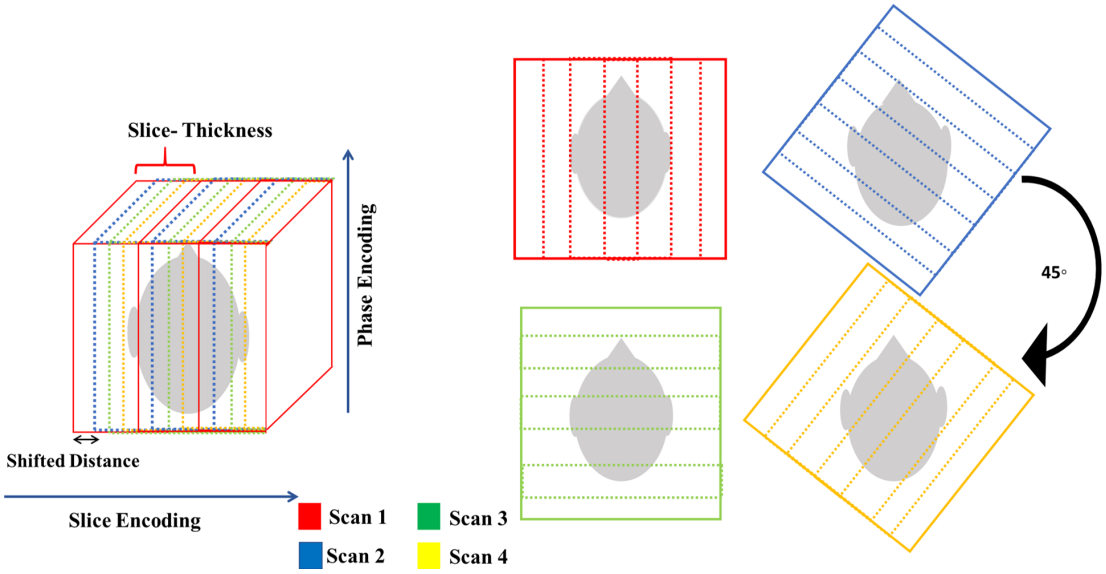

Figure 5.1: *Illustration of the linear shifting (Left) and rotation (Right) experiment. The dashed lines within the boxes indicate the slice encoding direction; the frequency encoding direction is from head to toe. For the linear shifting, each low-resolution scan (colours) is shifted by a known subpixel distance along the slice encoding direction (which in this case is sagittal). For illustration purposes, the shifting of the FOV (coloured boxes) has been exaggerated. For rotation, each of the low-resolution scans is rotated (45°) across the common encoding direction. The red box represents the sagittal section; green box represents the coronal section, the blue and yellow box represent diagonal sections.*

In principle, we assume that adding more rotations (e.g. two rotations with orthogonal versus four rotations with diagonal) will increase the accuracy of the SR reconstruction but at the expense of increased acquisition time. To that end, various numbers of rotations (two, four and five) were tested in combination with different acceleration factors (6-fold, 10-fold, 14-fold) to determine a trade-off between accuracy and acquisition time. The RMSE between the ground truth and the estimated T_2 map was calculated to quantify the reconstruction quality.

5.3.2 Image Acquisition

The proposed approach was tested on a multipurpose phantom and four healthy subjects. Permission from the Institutional Review Board was obtained for all the in-vivo imaging studies

and written informed consent for the study, and its publication was obtained from all participants prior to the experiments.

5.3.2.1 GRAPPATINI Sequence

The datasets were acquired with a standard 20-channel head/neck coil using a 10-fold undersampled GRAPPATINI [3] prototype sequence at 3T (MAGNETOM Skyra, Siemens Healthcare, Erlangen, Germany). This is basically a CPMG sequence with a block schemed (MARTINI) [66] k-space sampling pattern. This pattern fully samples segments (blocks) of k-space, shifting the k-space position of subsequent sampling blocks in the echo dimension by one block width. Figure 5.2a shows the MARTINI undersampling scheme for different undersampling factors. The following considerations have to be taken into account with the GRAPPATINI sequence:

- **Blockwidth**: The block width is defined by the number of phase-encoding steps divided by the MARTINI acceleration factor (AF). For example, for 60 phase encodings and AF of 5, the sequence will acquire a block of 12 phase encodings.
- **Number of Echoes**: The number of echoes should be divisible by the AF. For example, if the AF is 5, the number of echoes should be 15+1 (considering that the first echo is ignored). This way, all the echoes are sampled with the block of k-space.

In addition to the block k-space sampling, a classic parallel imaging scheme with 2-fold acceleration is used, i.e., only every other (phase-encoding) line inside a block is acquired. Since the first echo is not used in the reconstruction to mitigate stimulated echo effects, the reference lines necessary for GRAPPA are obtained by filling a central part of k-space with the first spin echo of each phase-encoding step. Therefore, in this implementation, no additional scan time is required to acquire a calibration dataset for the GRAPPA reconstruction. Notably, the number of reference lines results from the number of repetitions acquired in the sequence, i.e., the total number of phase-encoding lines divided by AF (which in this case is MARTINI AF $\times$ Parallel Imaging AF). An example GRAPPATINI sampling scheme is shown in Figure 5.2 (reference lines marked in green).

5.3.2.2 SR Image Acquisition

For the implementation of SR, the following datasets were acquired: for the first dataset, 50 sagittal slices with 4 mm thickness and 1x1 mm^2 in-plane resolution were acquired. The FOV was moved by 1 mm in the slice-encoding direction with four shifts implementing the linear transformation. The total time of acquisition for this dataset was 16 minutes. For the second dataset, 60 slices each in two orthogonal orientations (sagittal and coronal) and two diagonal orientations (Sagittal $>$ Coronal 45 $^\circ$ and -45°) with the same slice thickness and in-plane resolution were acquired. The acquisition time for this dataset was 18 minutes. In addition, the same dataset (i.e. orthogonal and diagonal) was acquired with a 14-fold acceleration, which reduced the acquisition time to 11 minutes. Of note, the dataset with orthogonal orientation was not acquired separately but rather the two diagonal orientations were removed during reconstruction to make a third dataset. Spectral fat suppression was enabled to suppress the fat signals from the fat around the skull. For reference T_2 values, a fully sampled MESE dataset with 16 echoes and 29 slices and a resolution of 1.1 x 1.1 x 4 mm^3 was acquired. In addition, for the phantom, a conventional single-slice single-echo SE sequence with three TEs (12, 50, 100 ms) was acquired. A detailed overview of the acquisition parameters of these datasets can be found in Table 1.

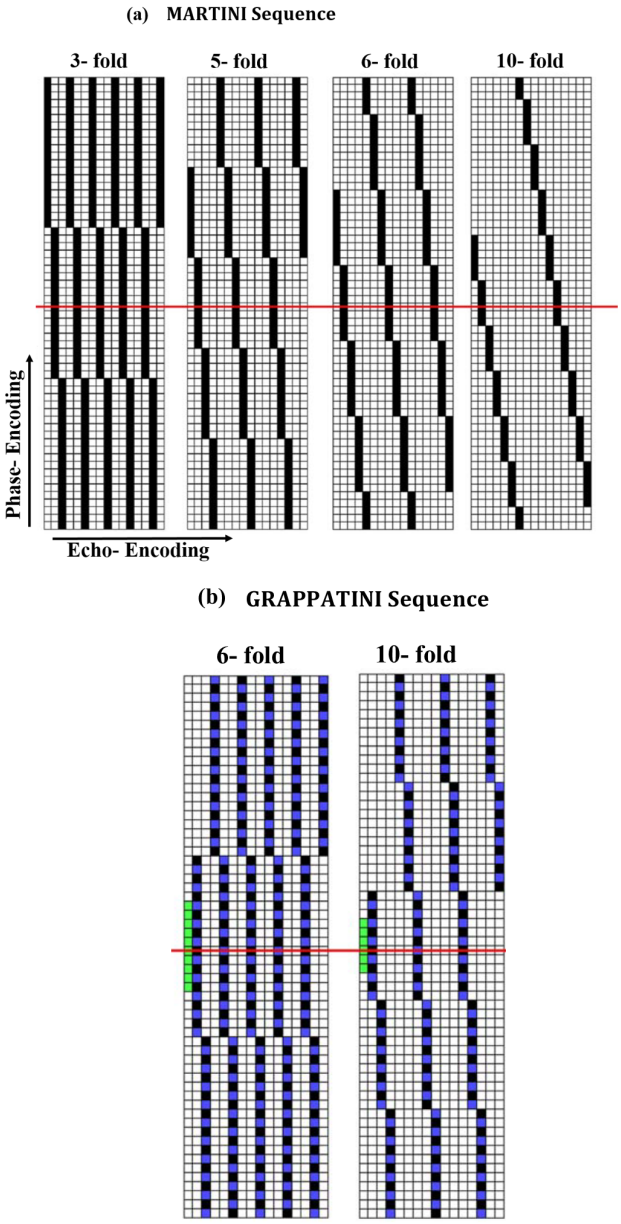

Figure 5.2: *(a) MARTINI sampling pattern and (b) the proposed GRAPPATINI sampling pattern with black squares indicating sampled and white squares nonsampled data for an example image matrix with 60 phase-encoding lines and 16 echoes. The readout dimension is orthogonal to the shown k-space plane. The red line indicates the k-space centre with zero phase-encoding. The green samples in the GRAPPATINI pattern indicate the sampled first echo lines used for GRAPPA calibration. The blue squares indicate nonsampled k-space lines that are reconstructed using GRAPPA only [3].*

Dataset	In-plane resolution (mm^2)	Slice thickness (mm)	Acquisition Matrix	Slices	TR(s)	No. of shifts/ rotations	Acceleration	No of echoes	Scan time (mins)
Linear	1 x 1	4	240 x 256	50	4.4	4	10	16	16
Orthogonal	1 x 1	4	240 x 256	60	5.3	2	10	16	08
Diagonal	1 x 1	4	240 x 256	60	5.3	4	10	16	18
Diagonal Fast	1 x 1	4	224 x 240	56	4.7	4	14	15	11
MESE- Fully Sampled	1.1 x 1.1	4	192 x 160	29	5	-	-	16	14
SE- Fully Sampled	0.9 x 0.9	4	224 x 256	1	2.5	-	-	3	21

Table 5.1: *Overview of the relevant acquisition parameters of the data sets.*

5.3.3 Image Reconstruction

The algorithm was implemented using Matlab (MATLAB2017a, The Mathworks Inc., Na-tick, USA). First, a GRAPPA [9] reconstruction was used to fill the missing lines in each block of the acquired k-space according to [3]. Using the central k-space samples available at different echo times, composite fully sampled images were reconstructed and up-sampled to the HR grid. Subsequently, an initial guess of a T_2 and ρ map were estimated from these up-sampled images by non-linear least square fitting of the magnitude HR images. This estimate of the maps was then used in the algorithm for SR T_2 estimation by alternately solving equation 5.5 as described in the theory section by fixing T_2 and ρ first. Complex coil sensitivities were approximated for each of the transformations by summing k-spaces across echoes. The k-space is then transformed into coil images by inverse Fourier transform and then these individual images are divided by the sum of squares of images to obtain coil sensitivities [8]. The regularization parameter was heuristically selected as $\lambda = 1$ aiming at equal contributions from model- and data-consistency to the cost function. The reconstruction was performed iteratively until the error was less than $\varepsilon = 1e^{-}04$:

$$\frac{\| X^{(i)} - X^{(i-1)} \|}{\| X^{(i)} \|} < \varepsilon \tag{5.6}$$

where $X^{(i)}$ was the reconstructed signal series at i^{th} iteration. In addition, the maximum number of iterations was fixed to 30 after it was experimentally tested at what iteration the algorithm typically convergences (see Appendix). The reconstruction scheme is illustrated in Figure 5.3.

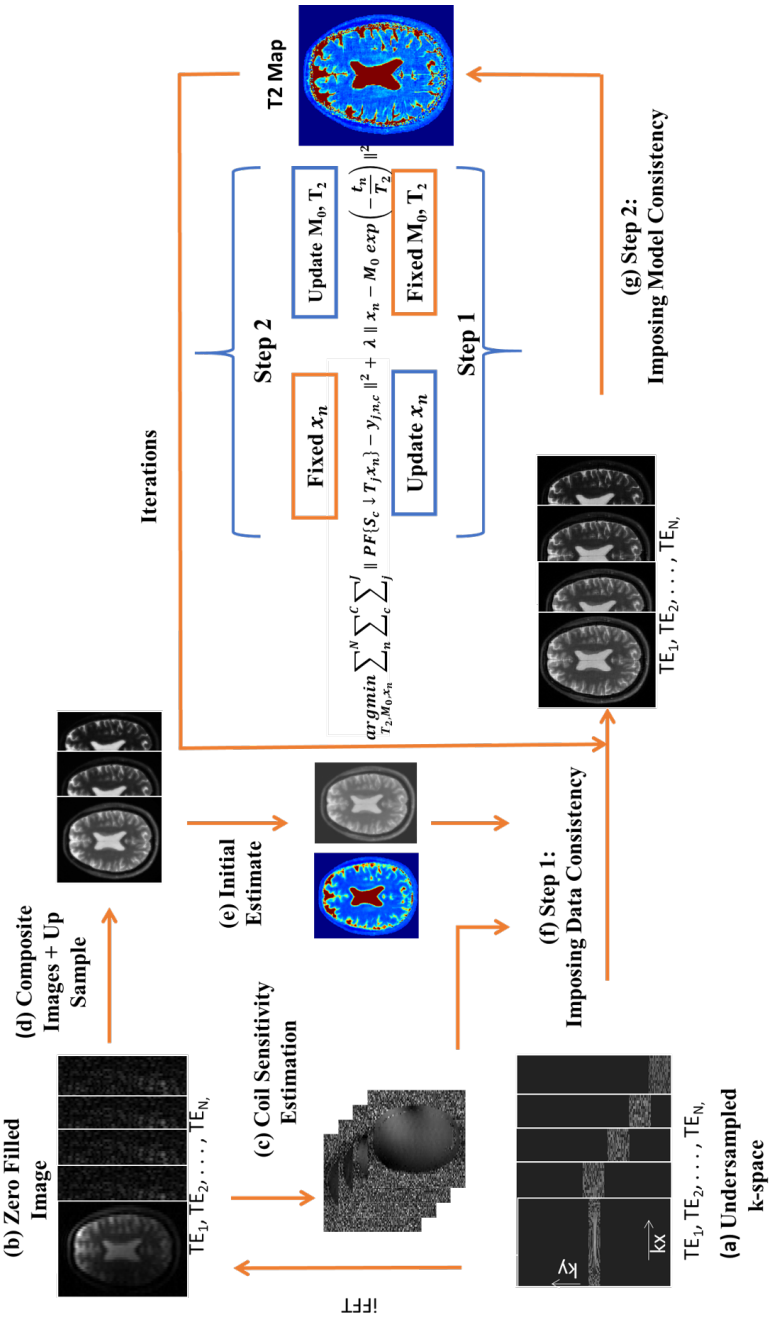

Figure 5.3: *The schematic flowchart for model-based SR reconstruction: a) k-space data with block undersampling; b) Zero-filled image using the inverse FFT in the phase-encoding direction; c) Sensitivity maps estimation; d) Composite images are formed and up-sampled to HR grid; f) Data consistency is imposed as a first step of alternating minimization; g) T_2 maps estimated by imposing model consistency in the second step. With the new estimate of T_2, step 1 and step 2 are repeated iteratively. SR- super-resolution, FFT – Fast Fourier Transform, HR – High Resolution.*

5.3.4 Validation

To evaluate the performance of the proposed SR model-based method, T2 maps were visually compared to T_2 maps from two other methods using the numerical phantom and one in-vivo dataset. The first reference approach is LR model based + SR reconstruction where LR T_2 maps were first reconstructed from individual LR orientations using model-based reconstruction followed by an SR algorithm to up-sample to an HR T_2 map. The second reference approach is the SR reconstruction only without the model consistency term.

To ascertain the accuracy of the calculated T_2 values, an ROI analysis was performed on the phantom and in vivo T_2 maps for both accelerated and fully sampled datasets. T_2 values from different compartments of the phantom were compared with the T_2 values obtained from the conventional non-linear least squares fitting of the fully sampled MESE and SE data. Ground truth values provided by the manufacturer will be unreliable owing to the degradation of phantom material with the time so SE data values will be considered as a pseudo gold-standard. The same comparison was made for the healthy brain where ROIs were drawn in the frontal white, deep grey matter (putamen and caudate nucleus) and corpus callosum. ROI labelling and segmentation were performed using ITK-SNAP (31) (`www.itksnap.org`). The segmentation was performed in the native space of the fully sampled T_2w images. Subsequently, the fully sampled T_2w image was pairwise rigid-registered onto the T_2 maps of the other datasets using Elastix [201]. The resulting transformation was then applied to the label map of the ROIs to provide a similar segmentation among datasets. The four healthy volunteers who were scanned with both a 10 and 14-fold accelerated acquisition with diagonal orientations and a fully sampled MESE were used in an ROI analysis as well. The T_2 values from four ROIs were compared across all the volunteers to ascertain the consistency of T_2 values across subjects.

5.4 Results

5.4.1 Numerical Phantom

T_2 maps and images using SR model-based reconstruction in the numerical phantom using different orientations (linear, orthogonal, and diagonal) are shown in Figure 5.4 in comparison to the ground truth. The T_2 map reconstructed with diagonal rotation shows improved resolution in comparison to the linear and orthogonal datasets. The comparison between the three orientations in reconstructed T_2w images also shows sharper edges in the high-resolution image when

using the diagonal orientation. This can be better appreciated in the zoomed images of the same area that demonstrates the diagonal rotation results in better delineation of the small structures in the brain.

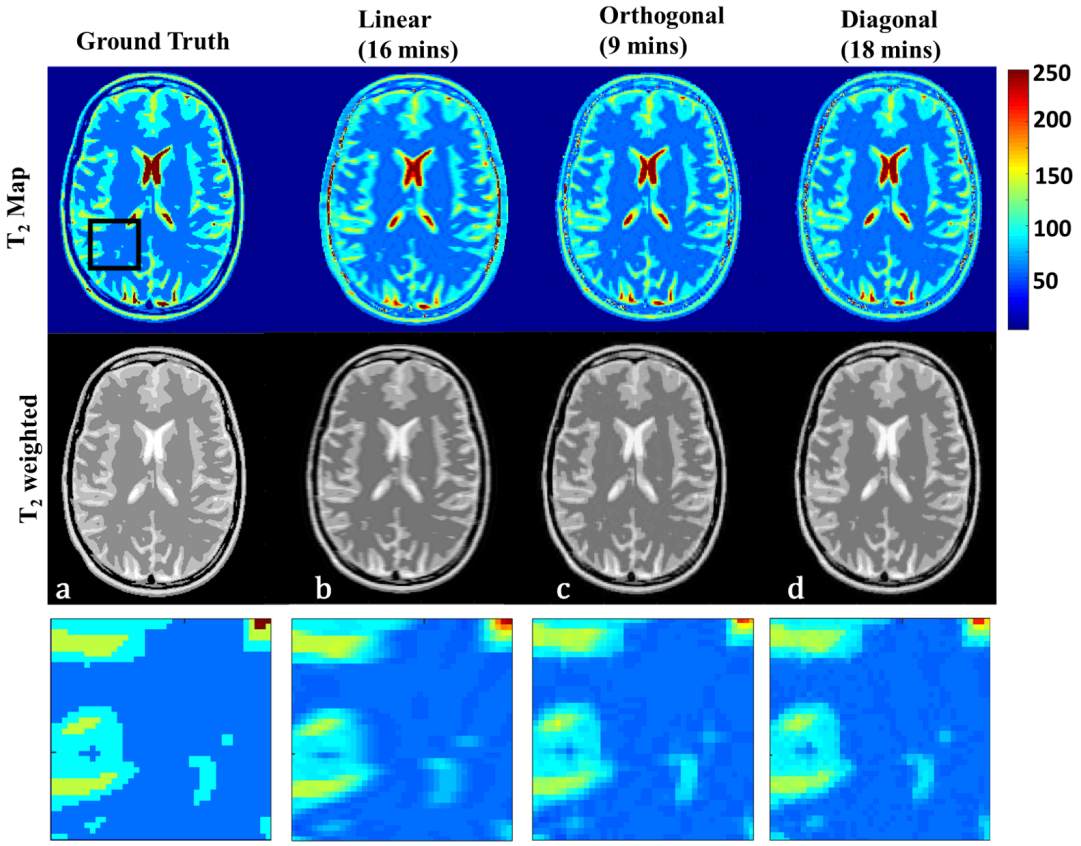

Figure 5.4: *Numerical Phantom: Super-resolution T_2 Maps (upper row), reconstructed T_2-weighted images (middle row) and the zoomed-in images (bottom row) for three different orientations. a) Ground Truth (b) linear shifting (c) orthogonal rotation (d) diagonal rotation.*

The difference images between the ground truth and reconstructed T_2 maps along with the RMSE is shown in Figure 5.5. The highest error is demonstrated by the linear shifting which is also indicated by the respective RMSE. For orthogonal rotation, the difference image exhibits less error with improved resolution in left-right direction. The diagonal rotation demonstrated the least RMSE with improved resolution in both left-right and top-bottom direction.

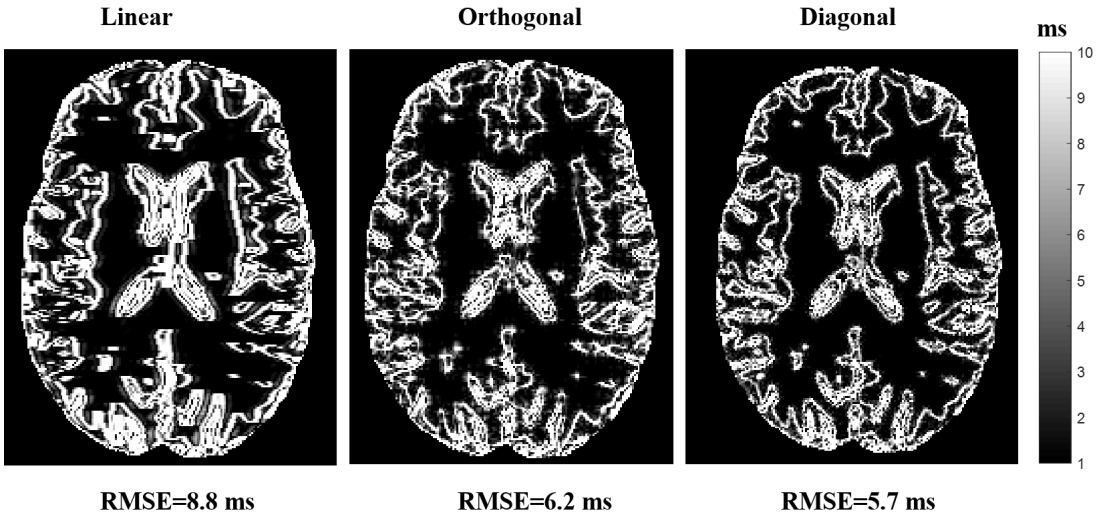

Figure 5.5: *Difference images of the ground truth and the reconstructed T_2 maps of numerical phantom for the linear, rotation and diagonal orientations with the respective RMSEs.*

The trade-off between the number of rotations and the acceleration is demonstrated in Figure 5.6. The numerical simulation demonstrated that adding more rotation results in reduced error around the edges for all the acceleration factors (from left to right). At the same time, an increased acceleration factor has the effect of an overall reduction in image quality, i.e. an increased difference of the T_2 values from the ground truth (top to bottom). Considering the prolonged acquisition time with the number of rotations, the best trade-off is 10-fold acceleration with four rotations (RMSE=7.8 ms, TA=18 mins). Five rotations and 6-fold acceleration showed the least error (RMSE=3.2 ms) but required an acquisition time of 37 minutes. 14-fold acceleration with five rotations had an acquisition time of 14 minutes but an RMSE of 12.5 ms. The details of the RMSE for all the accelerations and rotations are provided in Table 5.2.

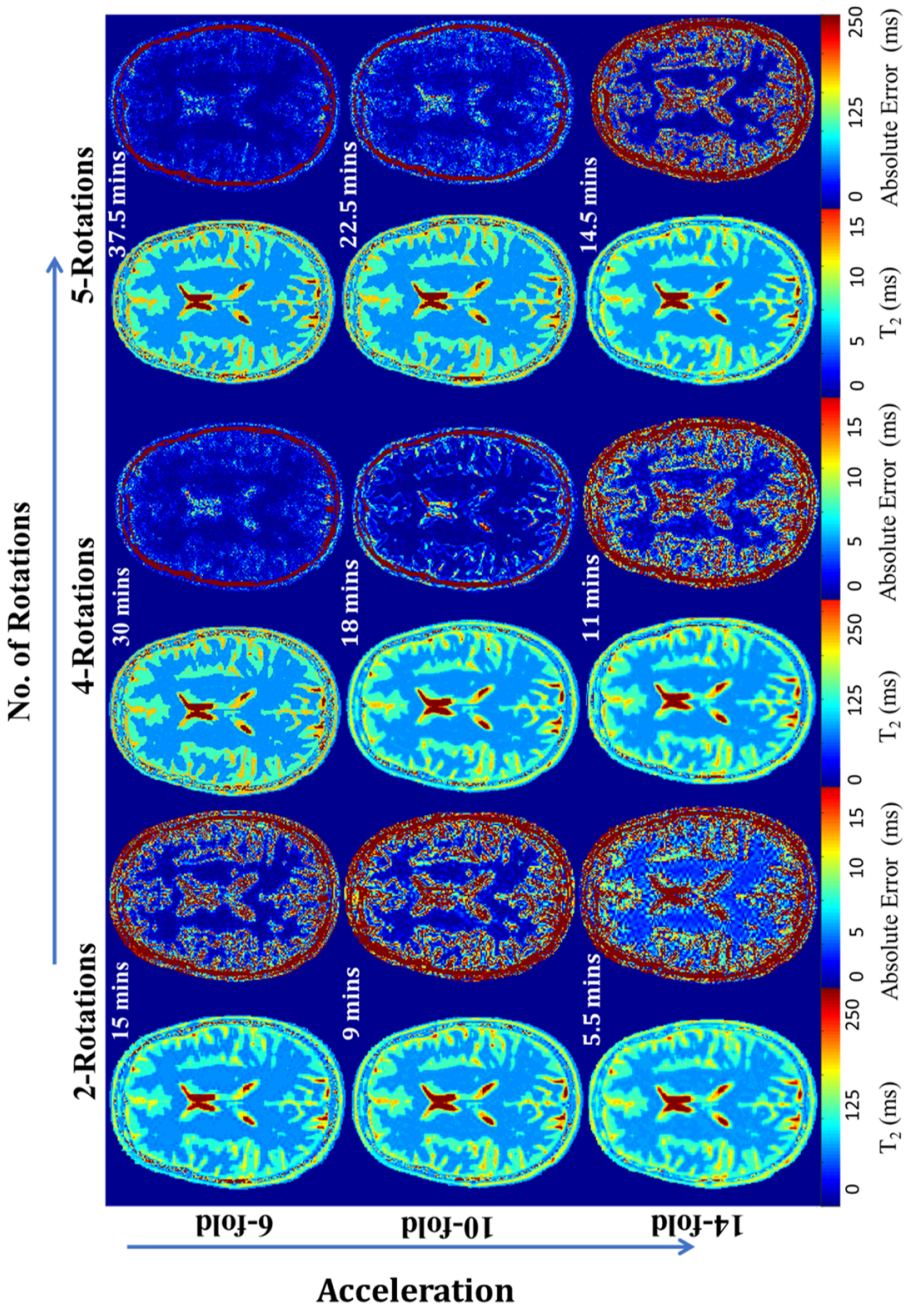

Figure 5.6: *The gain in the quality of super-resolution (SR) -T_2 reconstruction as a function of number of rotations and acquisition time in a numerical phantom. The corresponding acquisition times are mentioned with the T_2 maps. Adding more rotations results in reduced error around the edges for all acceleration factors (from left to right). At the same time, the acceleration factor affects the quality of the reconstruction (top to bottom), especially for high T_2 values in the cerebral spinal fluid. Considering the increase in acquisition time with the number of rotations, it can be deduced that the optimal configuration is 10-fold with four rotations.*

	Rotations			
Acceleration		**2**	**4**	**5**
	3	13.8	5.6	3.2
	5	15.2	7.8	8.8
	7	17.1	9.82	12.3

Table 5.2: *Table showing the RMSE (ms) calculated for different rotations (Right to Left) and accelerations (Top to Bottom).*

5.4.2 Phantom and in-vivo Data

Figure 5.7 shows the reconstructed T_2 maps and PD images from one LR acquisition, and the SR model-based reconstructed maps for linear, orthogonal, and diagonal orientations for the phantom. The LR T_2 maps and PD (Figure 5.7a) show partial volume effects within the compartments of the phantom. For a fair comparison, the LR T_2 maps and M_0 with interpolation to HR grid are also shown which also exhibit the blurring of the compartment edges and brain structures 5.7b. T_2 maps with SR model-based reconstruction enhance the spatial resolution, reducing the partial volume effect. However, with linear shifting, there is still blurring of the edges around the compartments of the phantom. For orthogonal rotations, the compartment edges in the phantoms appear sharper in both orthogonal directions (Figure 5.7d, white arrows) whereas the diagonal orientation improves the sharpness further, especially in the diagonal direction (Figure 5.7e, black arrows). The same can be observed for the human brain where diagonal rotation improved the spatial resolution and delineation of the brain structures (Figure 5.8 and 5.9).

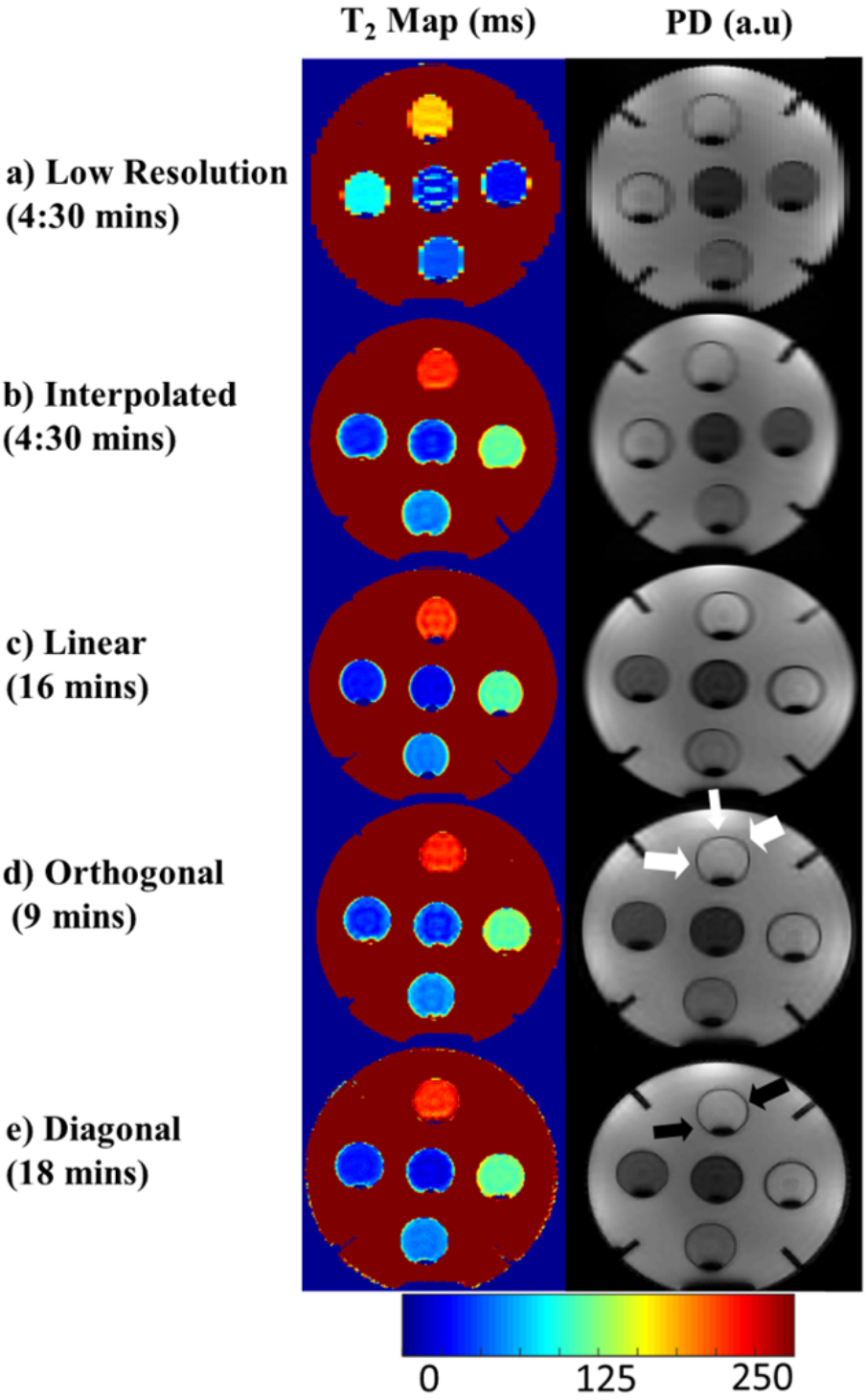

Figure 5.7: *Reconstructed T_2 maps and PD for phantom (a) low-resolution, (b) interpolated to HR grid, (c) linear, (d) orthogonal, and (e) diagonal datasets with respective acquisition times. The orthogonal rotation improved the resolution as can be seen around the edges of the compartments in two directions (white arrows) whereas diagonal orientation improved the resolution in four directions (black arrows).*

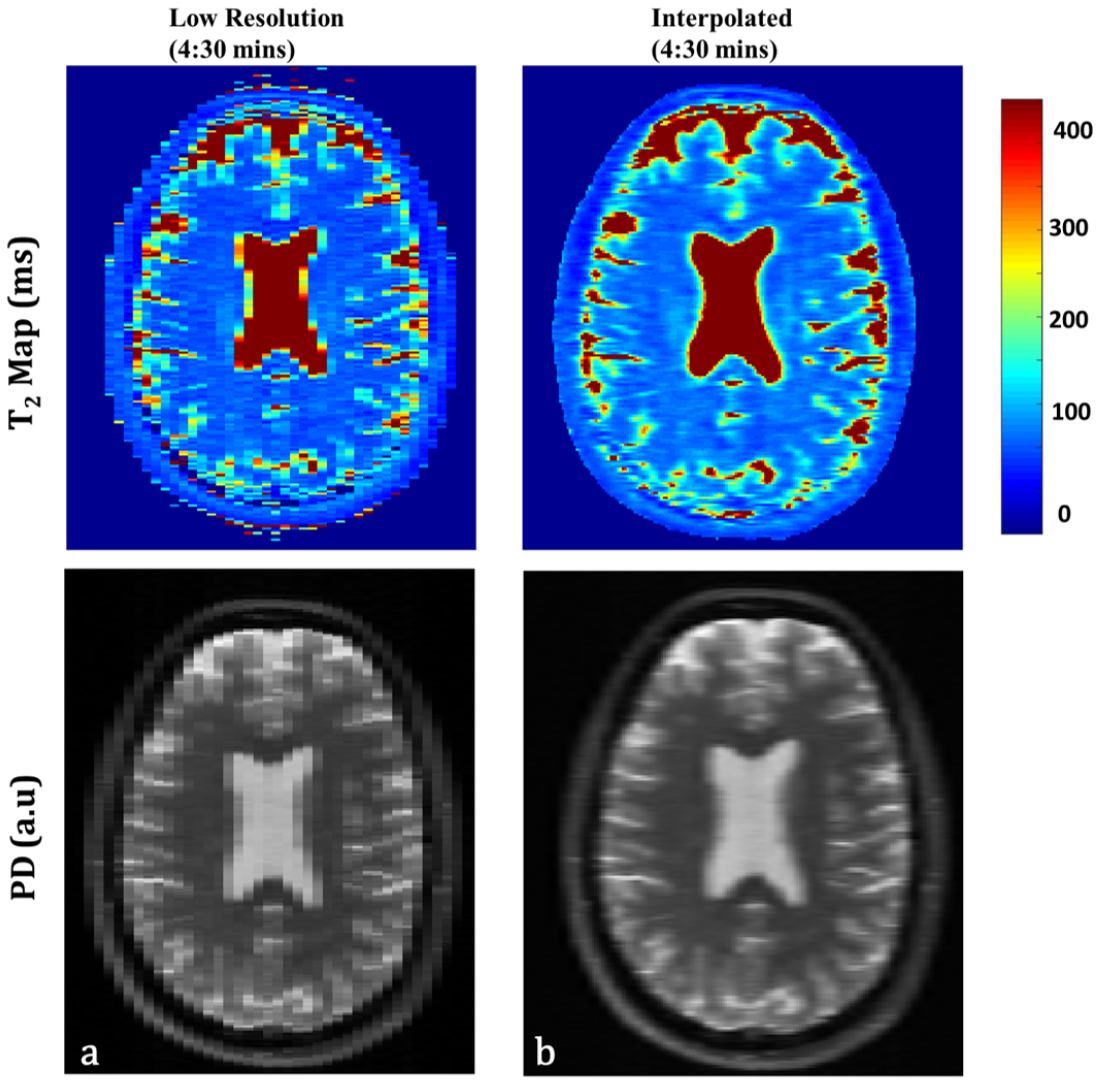

Figure 5.8: *Reconstructed T_2 maps and M_0 human brain from (a) low-resolution, (b) interpolated to HR grid. Simple interpolation to the higher resolution grid does not help in improving the resolution.*

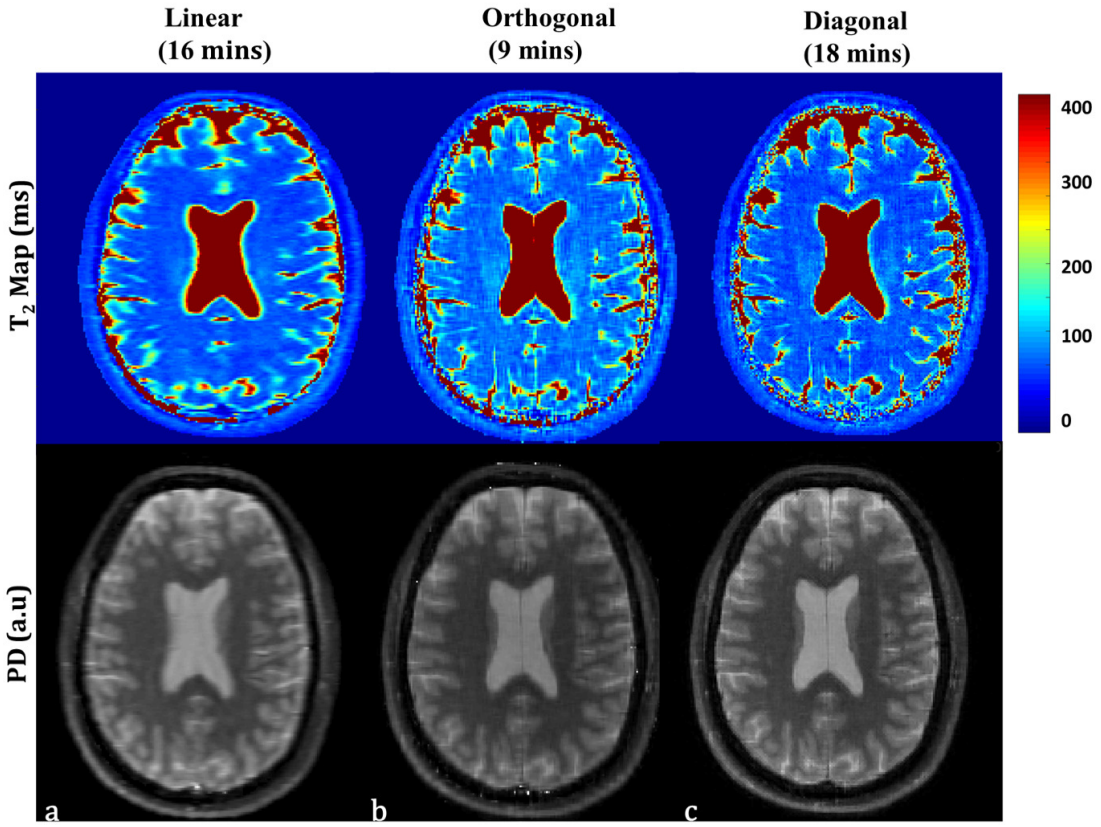

Figure 5.9: *Reconstructed T_2 maps and M_0 human brain from (a) low-resolution, linear, (b) orthogonal, and (c) diagonal datasets with respective acquisition times. As can be seen in the phantom, the diagonal orientation demonstrated better resolution in brain structures as compared to orthogonal rotation and linear shift.*

Figure 5.10 shows the axial and coronal views of the reconstructed T_2-weighted images from a 10-fold accelerated LR dataset with diagonal orientations and fully sampled MESE data. It is evident that the SR-T_2 mapping allows satisfactory 3D visualization due to isotropic resolution as compared to conventional MESE, which inherently has a low through-plane resolution. This can be appreciated even more from the zooms shown in Figure 5.10. A transversal zoom on the caudate nucleus head and the putamen is shown where the interface between different structures is well delineated in both SR-T_2-weighted and MESE-T_2-weighted images. However, for the coronal zoom, the interface between grey and white matter is better defined for the SR-T_2-weighted image.

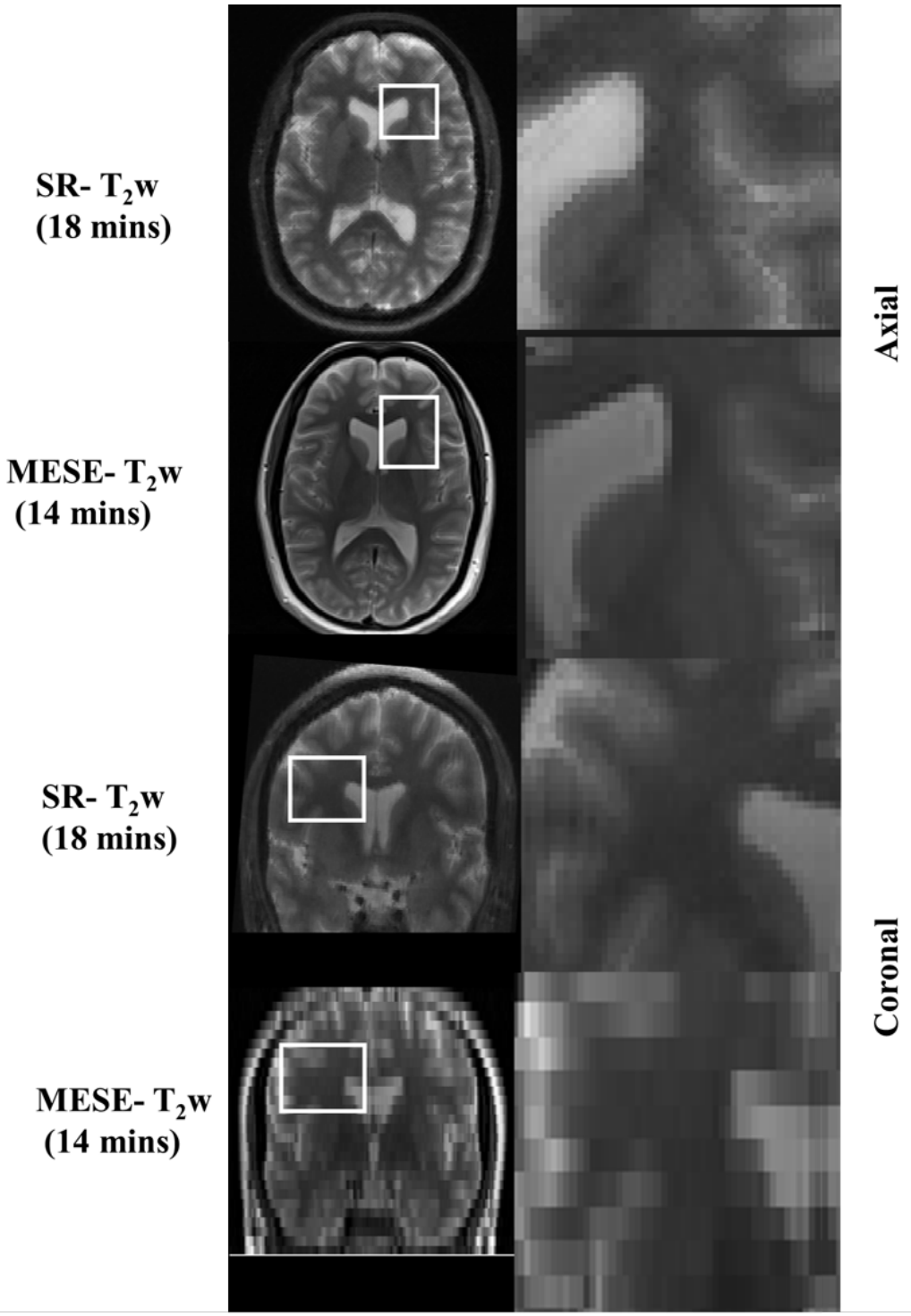

Figure 5.10: *Axial and coronal views of T_2-weighted images reconstructed with super-resolution (SR)-T_2 mapping (left) and single echo T_2-weighted image from fully sampled MESE. The zoom depicts the improved resolution in both planes for SR compared to the conventional sequence.*

5.4.3 Validation

A comparison between the SR model-based reconstruction and the SR only and LR model-based + SR reconstruction is shown in Figure 5.11. The figure shows the T_2 maps and the difference map for the numerical phantom. The SR only reconstruction showed visible artefacts due to the undersampling as no prior information from the signal model (mono-exponential decay) was incorporated in the reconstruction. The LR model-based + SR re-construction showed improvement in the reconstruction; however, blurring around the edges is evident in the difference map. In comparison, SR model-based reconstruction demonstrated that integrating SR and model knowledge jointly in one cost function improves the reconstruction.

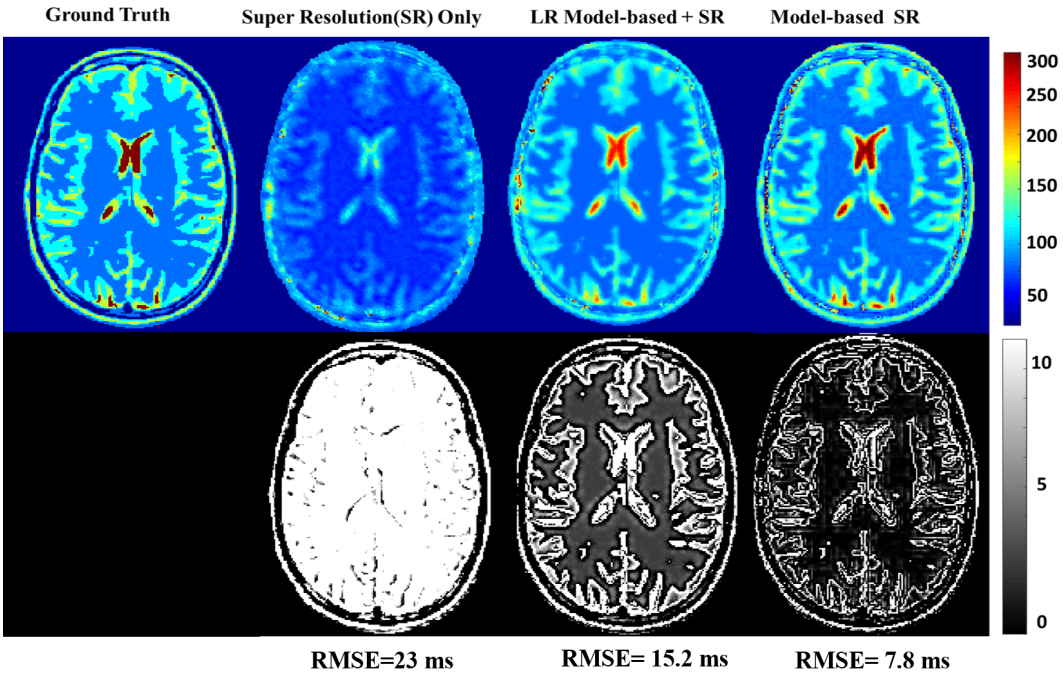

Figure 5.11: *T_2 maps reconstructed Images from the numerical phantom along with the difference image. The maps are shown from (a) Ground Truth, (b) SR reconstruction only, (c) LR model-based followed by SR reconstruction, and (d) proposed SR model-based reconstruction.*

Similar results were seen in the in-vivo data, but due to the absence of ground truth, no quantitative comparison could be made. However, visually, the proposed approach outperforms the other two methods in delineating brain structures, as seen in Figure 5.12.

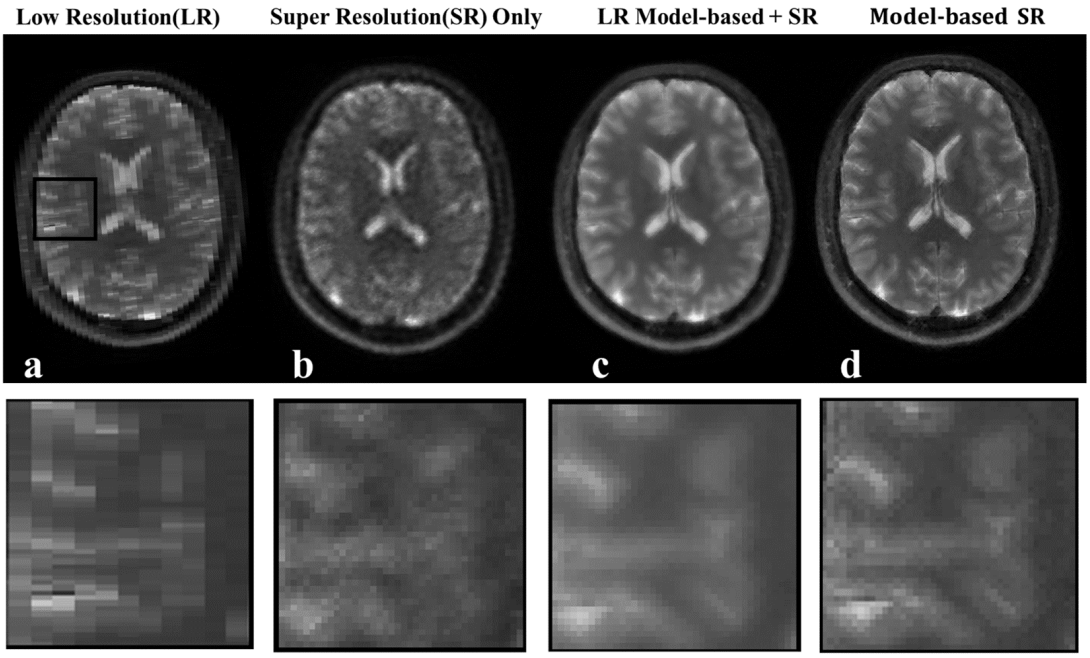

Figure 5.12: *Reconstructed T_2w images from in-vivo data. The images are shown from (a) a low-resolution dataset, (b) SR reconstruction only, (c) LR model-based followed by SR reconstruction, and (d) proposed SR model-based reconstruction. The SR only reconstruction showed increased noise due to the undersampling as no prior information from the signal model (mono-exponential decay) was incorporated in the reconstruction. The LR model-based + SR reconstruction showed improvement in the reconstruction; however, blurring around the edges is evident.*

5.4.4 ROI Analysis

The ROI analysis of the phantom compartments revealed that at shorter T_2, 10-fold accelerated data were comparable with the fully sampled MESE (Figure 5.13). For compartment 1, the mean T_2 value for 10-fold accelerated data was 28.0 $\pm$ 1.8 ms, for 14-fold it was 32.8 $\pm$ 1.4 ms, whereas the T_2 value for the MESE was 29.6 $\pm$ 0.9 ms and for SE was 16.4 $\pm$ 0.5 ms. For compartment 2, the mean T_2 value for 10-fold, 14-fold, MESE and the SE was 31.5 $\pm$ 1.4 ms, 34.0 $\pm$ 1.8 ms, 32.3 $\pm$ 1.2 ms and 22.9 $\pm$ 0.9 ms respectively. However, the error increased with higher T_2 values, with compartments 3 and 4 showing a relative difference of 10-12%. For compartment 3, the mean T_2 values for 10-fold was 50.0 $\pm$ 2 ms, for 14-fold was 49.2 $\pm$ 1.5 ms, for MESE was 55.5 $\pm$ 0.5 and for SE was 41 $\pm$ 0.3 ms. The mean T_2 values for compartment 4 for 10-fold, 14-fold, MESE and SE were 100 $\pm$ 0.4, 88.49 $\pm$ 0.6, 103.9 $\pm$ 0.5

and 81 $\pm$ 0.1 ms respectively. For compartment 5, a greater difference ($> 15\%$) was observed with mean T_2 values of 180.6 $\pm$ 4.5 ms, 175.5 $\pm$ 5.4 ms, 192.3 $\pm$ 3.4 ms and 156 $\pm$ 2.5 ms for 10-fold, 14-fold, MESE and SE respectively. All values derived with a MESE sequence were overestimated in comparison to T_2 values derived from a SE sequence. This overestimation is well known and caused by the stimulated echoes formed in the MESE sequence [192].

For the in-vivo data, the T_2 values in different regions of the brain showed good agreement with the fully sampled MESE acquisition (Figure 5.14b). For frontal white matter, the mean T_2 value for 10-fold acceleration was 80 $\pm$ 1.3 ms, for 14-fold was 76.5 $\pm$ 5.1 and for MESE fully sampled was 83 $\pm$ 2.08 ms. For putamen, the mean T2 value for 10-fold, 14-fold, and MESE fully sampled was 69.8 $\pm$ 1.2, 66.22 $\pm$ 1.32 and 73 $\pm$ 3.09 ms respectively. In the corpus callosum (MESE T_2 = 94 $\pm$ 2 ms), the 14-fold acceleration showed increased difference (80 $\pm$ 2.4 ms) as compared to 10-fold (87 $\pm$ 1.8 ms). The T_2 value for the caudate nucleus with the 10-fold acceleration (74.8 $\pm$ 2 ms) was closest to the MESE acquisition (75 $\pm$ 1.8), whereas the T_2 at 14-fold acceleration was 67 $\pm$ 2.8 ms. Comparing the mean T_2 values for 10-fold accelerated data from all the four ROIs across volunteers demonstrated consistent values with some natural variation (Figure 5.14c). The average T_2 value across all volunteers were 70.8 $\pm$ 8.5 ms for the frontal white matter, 81.3 $\pm$ 10.5 ms for the putamen, 79.8 $\pm$ 9.5 ms for the corpus callosum and 79.66 $\pm$ 13.6 ms for the caudate nucleus.

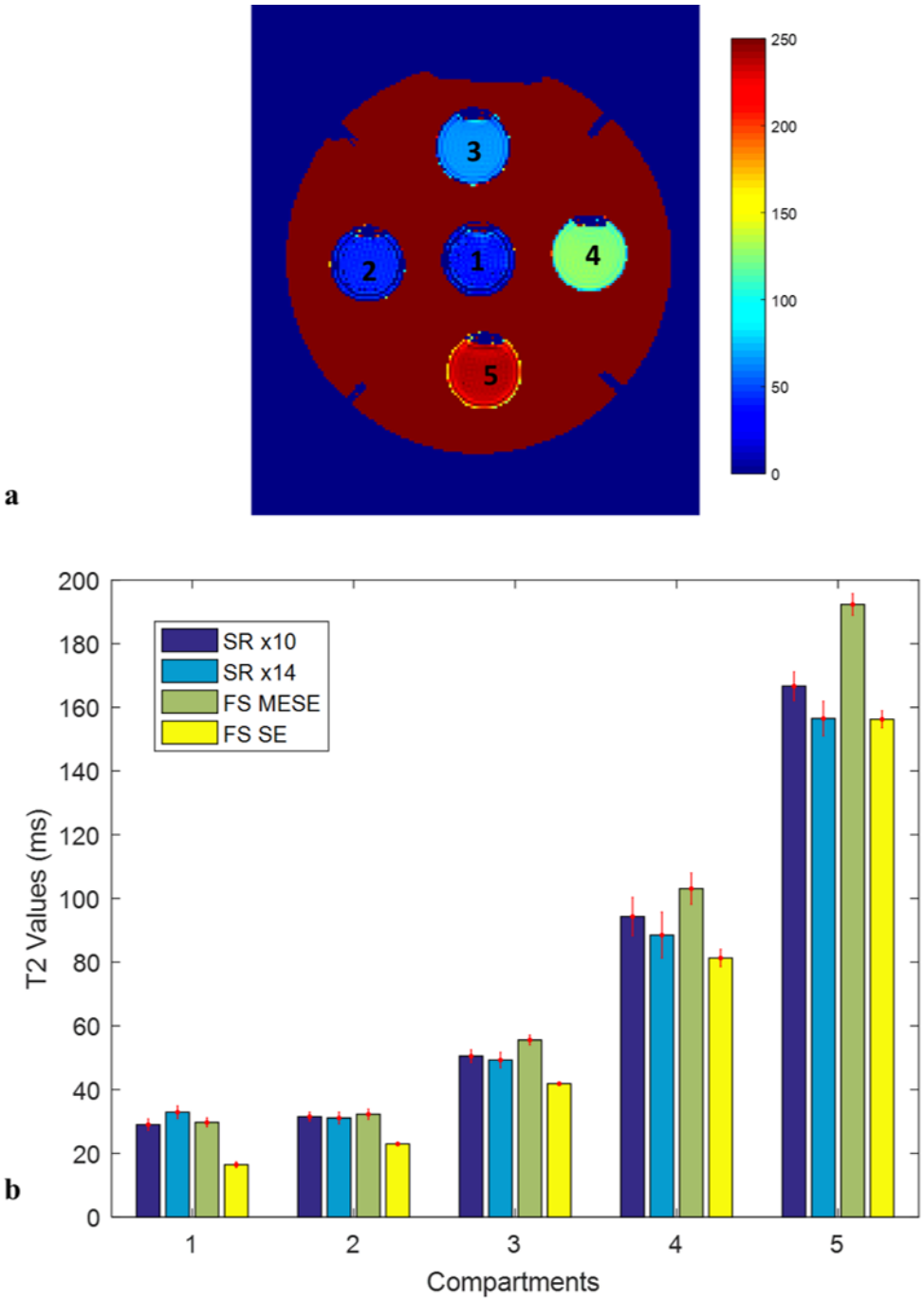

Figure 5.13: *ROI Analysis for the accuracy of T_2 estimation for different datasets in different compartments of the phantom. a) T_2 map of the phantom with different compartment labels. b) The bar chart represents the mean of the T_2 values of the ROI, and the error represents the standard deviation for 10-fold, 14-fold and fully sampled MESE and SE T_2 values.*

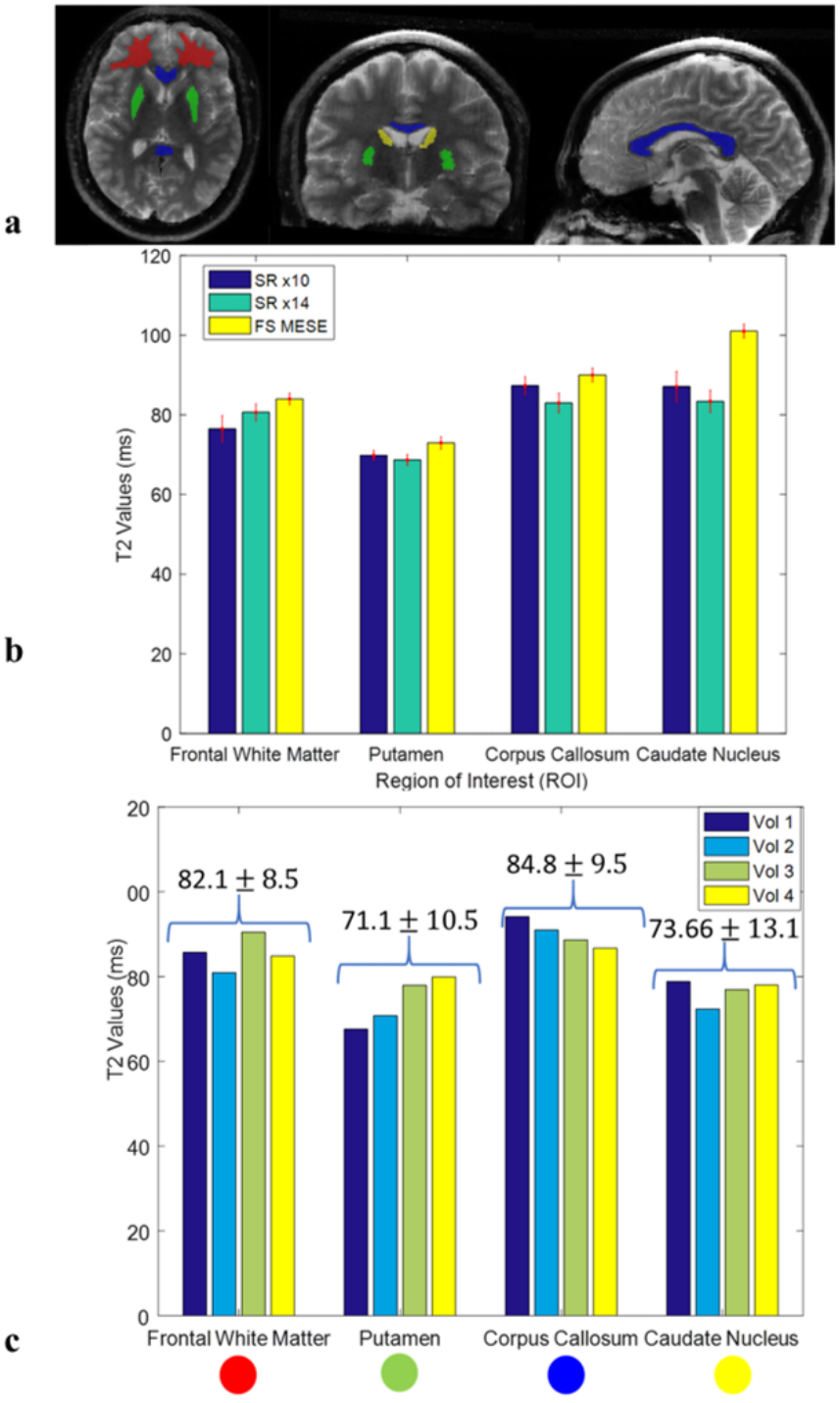

Figure 5.14: *a) Different ROIs drawn in axial, coronal and sagittal section of one volunteer b) The bar chart represents the mean T_2 values and standard deviation for accelerated and fully sampled datasets in four different regions of brain. c) The mean and standard deviation T_2 values found in all subjects grouped by brain structures, each bar representing a subject.*

5.5 Discussion

The widely used MESE sequence for T_2 mapping has a typical trade-off between SNR, resolution and scan time. To improve this trade-off, we proposed an SR acquisition and reconstruction method specific for quantitative T_2 mapping. The reconstruction method combines SR and model-based reconstruction for T_2 estimation into one integrated approach, enabling the direct estimation of an isotropic high-resolution T_2 map from a set of anisotropic, undersampled, low resolution k-spaces.

Numerical simulations demonstrated that rotating the slice orientations around the phase encoding direction results in better image quality of the SR reconstruction than linear sub-pixel shifts in the slice encoding direction. These results were confirmed by the phantom and the in-vivo acquisitions where the rotation resulted in much sharper images. Low resolution images with different slice orientations appear to better sample different spatial information than shifting the low-resolution images by subpixel distances along the slice selection direction [148]. The optimal number of slice orientations ensures that enough spatial information is contained in the LR images to reconstruct the high-resolution image without extensively prolonging the acquisition time. The comparison between number of rotations versus acceleration factor showed that four slice orientations (0 °,90°,45°, -45°) with 10-fold acceleration was the optimum in this application with an acquisition time of 18 minutes.

The advantage of combining SR with model-based reconstruction has already been demonstrated for T_1 mapping [170]. This work was done in the image domain without k-space undersampling, whereas the proposed approach addresses a more complex problem by reconstructing quantitative maps from undersampled k-space data. It is important to ascertain whether model-based SR-T_2 mapping performs better than the sequential application of model-based and SR reconstructions. The comparison of the proposed approach to the SR reconstruction without prior model and to the LR model-based reconstruction followed by SR reconstruction demonstrated that incorporating the model information in the reconstruction yielded improved results.

Comparing a T_2 map estimated with model-based SR to a T_2 map estimated with a conventional non-linear least square fitting on a fully sampled MESE dataset proved that T_2 values are comparable between the two methods. For the phantom, the compartments with longer T_2 had a higher bias as compared to short T_2, which may be attributed to an inaccurate signal model. For example, as already reported in the literature [192], T_2 values derived from MESE-type

acquisitions are overestimated in comparison to single-echo SE acquisitions due to stimulated echo signal contributions which mostly stem from an imperfect slice profile of the refocusing pulses. This can be addressed by using a different signal model which accounts for the slice profile and B1 inhomogeneity e.g. by using an analytical [69, 192] or numerical [67, 70] signal model. The current model of the proposed method does not account for the slice profile. It is assumed that incorporating the slice profile in the reconstruction will not only allow addressing stimulated echoes issues but also lead to a more realistic downsampling/upsampling operator between HR and LR images. Since this more accurate model will potentially further improve the spatial resolution, the slice profile is subject of future investigations.

An alternative formulation of the reconstruction problem proposed here can be as follows: the signal in a LR voxel may consist of different types of tissue, e.g. at a WM and GM boundary. Therefore, the signal can be seen as a multi-exponential decay (neglecting micro-structural T_2 components). The fitting of a mono-exponential decay in a high-resolution voxel corresponds to a multi-exponential fitting in the space of the LR image due to the downsampling operator. This ill-posed problem becomes better conditioned through incorporating various orientations since each orientation consists of LR voxels with ideally different combinations of multiple decays.

With respect to the acquisition time, the 10-fold accelerated acquisition lasts 18 minutes. Despite the high acceleration, the acquisition time is too long to be accepted for clinical routine or clinical studies. A higher acceleration factor (14-fold) was tested, which reduced the acquisition time to 11 minutes but decreased the sharpness of brain structures. Various other techniques can be applied to further accelerate the acquisition time, such as simultaneous multi-slice [202, 203]. Moreover, the same sampling pattern was used in each slice and orientation. Varying the sampling across slices and orientations may improve the reconstructed T_2 maps and will be further investigated. SR approaches require different acquisitions with different orientations, and the reconstruction method assumes that each voxel corresponds to the same anatomical location in all the orientations. Subject motion and image distortions (e.g. due to imperfect gradient performance) violate this assumption and may not perfectly align the multiple orientations for model fitting. This model violation will lead to image artifacts, and the wrong T_2 values and pose a significant limitation on the proposed method. In the frame of this study, motion correction schemes were not explored but could be used to facilitate a better alignment of different orientations and improve the reconstruction. The area of motion correc-

tion and compensation has been well studied specifically for the SR reconstruction in foetal imaging [204, 205]. Future work will aim to incorporate these strategies to further improve the robustness of the SR-T_2 mapping. In addition, incorporating a spatial regularization of the T_2 maps will potentially further improve the reconstruction.

5.6 Conclusion

We have proposed a technique that uses four 10-fold undersampled LR MESE 2-D acquisitions to iteratively reconstruct a HR T_2 map. The proposed technique enables HR 1 mm^3 isotropic whole-brain T_2 mapping in 18 min. The proposed technique may allow the assessment of T_2 values in small brain structures valuable in the search of imaging biomarkers in the future.

Chapter 6
Conclusion

6.1 Summary

In this dissertation, reconstruction methods for accelerated quantitative MRI were proposed. These methods combine model-based reconstruction with the estimation of qMRI parameters, such as the spin-spin relaxation (including T_2 and T_2^* relaxation).

The problem in estimating the parameters with the incorrect noise assumption has been discussed in Chapter 3. Based on the Gaussian assumption of noise, the method was presented that use alternating projection algorithm to combine MLE and PI. The reconstruction problem is split into three steps: First, the SPIRiT kernel is used to implement the PI to acquire a series of images. Then MLE step is implemented on the magnitude of the image to estimate the T_2^* and PD maps. Subsequently, data consistency is applied to the acquired data. The algorithm was implemented for an accelerated T_2^* mapping experiment with retrospective undersampling in a phantom and human brain and. The method allows significant reduction (R=6) of the required data without compromising the quality of the parameter maps.

In Chapter 4, the importance of coherent phase information in improving the accuracy of the accelerated T_2^* mapping was investigated as compared to the magnitude-only fitting. Our approach extends the acceleration attained in PI to a MLE approach based on complex exponential model fitting, which avoids phase information loss in recovering T_2^* relaxation times. In addition, spatial regularisation in the form of TV was also implemented to improve the reconstruction. The method was tested on a MEGE T_2^* mapping experiment in a numerical phantom and healthy human brain data with retrospective and prospective (real time) undersampling. Compared with fully sampled reference scans, the use of phase information reduces the error of the accelerated T_2^* maps up to 20% as compared to the magnitude-only method. Coherent fitting results in better denoising and additionally provides valuable information about magnetic field inhomogeneity.

Model-based and super-resolution reconstruction in Chapter 5 enables high-resolution T_2 mapping(1 mm^3) from low resolution T_2-weighted images acquired with MESE which was highly

undersampled. With the help of numerical simulations, the best trade-off between acceleration and number of low-resolution datasets was evaluated (10-fold acceleration with four acquisitions, TA=18 mins). The proposed approach showed improved resolution over low-resolution images for both phantom and brain. ROI analysis of the phantom compartments revealed that at shorter T_2, the proposed method was compared with the fully sampled MESE. For the volunteer data, the T_2 values found in the brain structures were consistent across subjects (8.5-13.1ms standard deviation). This proof-of-concept study demonstrated promising results that can be further improved by employing robust motion and signal correction and incorporating correct slice profiles.

In summary, the main contributions of this work are to propose and study various signal models and to employ them in newly developed reconstruction techniques to accelerate image acquisition or improve imaging quality, especially in the field of quantitative MRI.

6.2 Towards Clinical Use

The use of undersampled data acquisition and compressed sensing reconstruction has the potential to reduce the total scan time and cost of MR acquisitions and to reduce the burden of imaging to patients. The current work was done in this context to improve the inherent trade-off between acquisition time, spatial resolution and SNR of qMRI experiments. Decreasing the acquisition time without reducing the SNR and spatial resolution would improve patient comfort and the quality of the parameter maps by decreasing the chance of involuntary motion. Improving the SNR would increase the precision of the qMRI parameter estimates, possibly leading to earlier and better diagnosis. Most importantly, it enables quantitative high-resolution investigation of the brain in clinically compatible scan time on a standard clinical MRI scanner. Quantitative MRI maps at a high spatial resolution would enable a better localisation of the changes in the biological parameters, which could improve the diagnosis of several diseases. Combining these methods with future hardware improvements may enable qMRI with unprecedented spatial resolution.

The method presented in this thesis has been implemented in a clinical scanner with the most commonly used Cartesian trajectory to widen its clinical application. However, to translate these techniques into clinical routine, the input of the radiologists is essential. Recent work demonstrated that the clinical condition to be assessed by radiological assessment significantly

influences the radiological scores of accelerated brain MRI [206]. Therefore, in order to increase the application of this method, the inclusion of radiologists to assess the diagnostic quality is very necessary. The field strength of MRI scanners being used has increased to 7T or 3T depending on the application, and we find ourselves increasingly constrained by physiological limitations of specific absorption rates and peripheral nerve stimulation. Nevertheless, the significance of accelerated methods in terms of patient comfort, cost and time cannot be denied, and further developments to increase its clinical use will be a way forward towards precision medicine.

6.3 Future Work

A major drawback of advanced iterative techniques for image reconstruction is the increased computation time. While this is one of the reasons why such methods have been disregarded in clinical settings, the situation has been changed in the past few years. Nowadays, graphics processing unit (GPU) has been one of the standard tools in high-performance computing. Among the GPU-based applications of MRI reconstruction, they have been gradually recognised and widely applied [207]. Hence, implementation on a massively parallel GPU will further speed up the reconstruction time considerably.

Noise amplification is the limiting factor in PI; a better regularisation seems to be the most important next step. The integration of adaptive regularisation has been studied in previous works to provide a more powerful mathematical framework for reconstruction [205, 208]. The idea of adapting the acquisition and reconstruction to a special application can be exploited in multiple ways. The benefits of incorporating prior information to reduce the noise level of reconstructed images have also been demonstrated ([209–211]. This could be achieved, for instance, by applying further prior knowledge in the reconstruction. The prior knowledge used in the reconstruction should be specific to the application, but as general as possible, to avoid undesired errors in the image due to the reconstruction.

As discussed in Chapter 5, one of the major limitations of the proposed method is the long acquisition time (TA= 18 mins), which needs to be reduced. One possible solution is to employ Simultaneous Multi Slice (SMS) to further accelerate the scan time. Model-based reconstruction with SMS has been employed for accelerating T_2 mapping [203]. Using the Power independent of a number of slices (PINS) pulse that limits the SAR, T_2 maps were acquired under

3 minutes. The additional acceleration and the possibility to acquire more slices may help to use it in other organs, e.g. in other abdominal regions, where only a short time during end-expiration or during a breath hold is available to acquire a T_2 map. The low power deposition of the PINS pulses may also allow using the new method at higher field strength.

Machine learning has seen some dramatic developments recently, leading to a lot of interest from industry, academia and popular culture. On the other hand, novel applications in medical image segmentation and reconstruction [212] indicate that deep learning has just begun and will continue to transform the field. Hence, future work will also focus in this direction, combining the previously developed techniques with deep learning algorithms to further improve MRI in general, and quantitative MRI in specific. In the context of quantitative MRI, machine learning has already been applied for MRF [213, 214]. The combination of deep learning with quantitative MRI techniques could significantly increase the capabilities and diagnostic value of MRI scanners, especially in situations where physical and theoretical models do not hold. For example, deep learning could play a key role when the acquired data violate the Nyquist limit, the SNR is too low, or the underlying biophysical models are too complex or inaccurate. This would transform MRI into a commodity instead of a luxury, increasing patient access and benefiting the population and health care systems on a global scale.

This thesis demonstrated the feasibility of the proposed methods in simulations and experiments with volunteers. Further research is necessary before these approaches can be adopted in clinical practice. In summary, advanced reconstruction techniques are necessary to exploit the potential of accelerated techniques in qMRI. The results of this thesis demonstrate the methods to develop and optimise accelerating methods; however, the path to a routine use still requires more research and validation studies. Quantitative MRI maps at a high spatial resolution would enable a better localisation of the changes in the biological parameters, which could improve the diagnosis of several diseases as well as the understanding of brain connectivity.

Chapter 7
Appendix

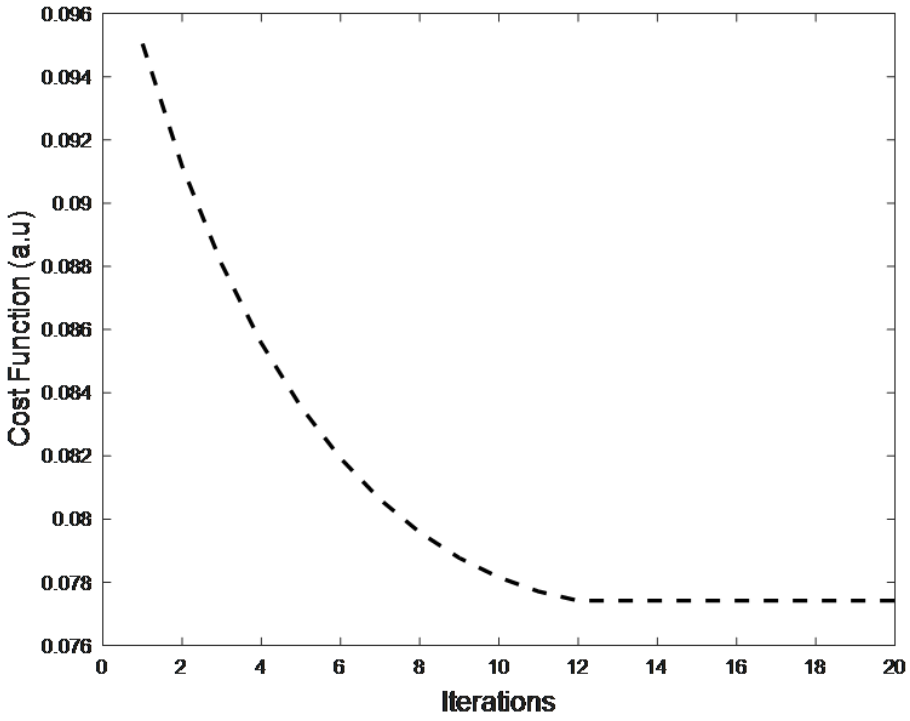

Figure 7.1: *The cost function of the algorithm converging smoothly and reaching a minimum after 15 iterations for a typical slice.*

References

[1] J. Hamilton, D. Franson, and N. Seiberlich, "Recent advances in parallel imaging for MRI," *Progress in nuclear magnetic resonance spectroscopy*, vol. 101, pp. 71–95, 2017.

[2] B. Aubert-Broche, A. C. Evans, and L. Collins, "A new improved version of the realistic digital brain phantom," *NeuroImage*, vol. 32, no. 1, pp. 138–145, 2006.

[3] T. Hilbert, T. J. Sumpf, E. Weiland, J. Frahm, J. Thiran, R. Meuli, T. Kober, and G. Krueger, "Accelerated T2 mapping combining parallel mri and model-based reconstruction: GRAPPATINI," *Journal of Magnetic Resonance Imaging*, 2018.

[4] A. Hsiao, M. Lustig, M. T. Alley, M. Murphy, F. P. Chan, R. J. Herfkens, and S. S. Vasanawala, "Rapid pediatric cardiac assessment of flow and ventricular volume with compressed sensing parallel imaging volumetric cine phase-contrast MRI," *American Journal of Roentgenology*, vol. 198, no. 3, pp. W250–W259, 2012.

[5] M. S. Cohen and R. M. Weisskoff, "Ultra-fast imaging," *Magnetic Resonance Imaging*, vol. 9, no. 1, pp. 1–37, 1991.

[6] S. Geethanath, R. Reddy, A. S. Konar, S. Imam, R. Sundaresan, and R. Venkatesan, "Compressed sensing MRI: a review," *Critical Reviews^{TM} in Biomedical Engineering*, vol. 41, no. 3, 2013.

[7] G. McGibney, M. Smith, S. Nichols, and A. Crawley, "Quantitative evaluation of several partial fourier reconstruction algorithms used in MRI," *Magnetic Resonance in Medicine*, vol. 30, no. 1, pp. 51–59.

[8] K. P. Pruessmann, M. Weiger, M. B. Scheidegger, P. Boesiger, *et al.*, "SENSE: sensitivity encoding for fast MRI," *Magnetic Resonance in Medicine*, vol. 42, no. 5, pp. 952–962, 1999.

[9] M. A. Griswold, P. M. Jakob, R. M. Heidemann, M. Nittka, V. Jellus, J. Wang, B. Kiefer, and A. Haase, "Generalized autocalibrating partially parallel acquisitions (GRAPPA)," *Magnetic Resonance in Medicine*, vol. 47, no. 6, pp. 1202–1210, 2002.

[10] M. Hutchinson and U. Raff, "Fast MRI data acquisition using multiple detectors," *Magnetic Resonance in Medicine*, vol. 6, no. 1, pp. 87–91, 1988.

[11] E. Candes, J. Romberg, and T. Tao, "Robust uncertainty principles: Exact signal reconstruction from highly incomplete frequency information," *arXiv preprint math/0409186*, 2004.

[12] D. L. Donoho *et al.*, "Compressed sensing," *IEEE Transactions on information theory*, vol. 52, no. 4, pp. 1289–1306, 2006.

[13] M. Lustig, D. Donoho, and J. M. Pauly, "Sparse MRI: The application of compressed sensing for rapid MR imaging," *Magnetic Resonance in Medicine*, vol. 58, no. 6, pp. 1182–1195, 2007.

[14] G. H. Glover and J. M. Pauly, "Projection reconstruction techniques for reduction of motion effects in MRI," *Magnetic Resonance in Medicine*, vol. 28, no. 2, pp. 275–289, 1992.

[15] H. Greenspan, G. Oz, N. Kiryati, and S. Peled, "MRI inter-slice reconstruction using super-resolution," *Magnetic Resonance Imaging*, vol. 20, no. 5, pp. 437–446, 2002.

[16] E. M. Shapiro, A. Borthakur, A. Gougoutas, and R. Reddy, "23Na MRI accurately measures fixed charge density in articular cartilage," *Magnetic Resonance in Medicine*, vol. 47, no. 2, pp. 284–291, 2002.

[17] J.-x. Yu, V. D. Kodibagkar, W. Cui, and R. P. Mason, "19F: a versatile reporter for non-invasive physiology and pharmacology using Magnetic Resonance," *Current Medicinal Chemistry*, vol. 12, no. 7, pp. 819–848, 2005.

[18] K. Golman, J. S. Petersson, P. Magnusson, E. Johansson, P. Åkeson, C.-M. Chai, G. Hansson, and S. Månsson, "Cardiac metabolism measured noninvasively by hyperpolarized 13C MRI," *Magnetic Resonance in Medicine*, vol. 59, no. 5, pp. 1005–1013, 2008.

[19] R. W. Brown, Y.-C. N. Cheng, E. M. Haacke, M. R. Thompson, and R. Venkatesan, *Magnetic resonance imaging: physical principles and sequence design*. John Wiley & Sons, 2014.

[20] Z.-P. Liang and P. C. Lauterbur, *Principles of Magnetic Resonance Imaging: a signal processing perspective*. SPIE Optical Engineering Press, 2000.

[21] A. Abragam and A. Abragam, *The principles of nuclear magnetism*. No. 32, Oxford university press, 1961.

[22] F. Bloch, "Nuclear induction," *Physical review*, vol. 70, no. 7-8, p. 460, 1946.

[23] B. Bleaney and B. Bleaney, "Electricity and magnetism," 1965.

[24] P. Tofts, *Quantitative MRI of the brain: measuring changes caused by disease*. John Wiley & Sons, 2005.

[25] N. Bloembergen, E. M. Purcell, and R. V. Pound, "Relaxation effects in nuclear magnetic resonance absorption," *Physical Review*, vol. 73, no. 7, p. 679, 1948.

[26] E. L. Hahn, "Spin echoes," *Phys. Rev.*, vol. 80, pp. 580–594, Nov 1950.

[27] E. L. Hahn, "Free nuclear induction," *Physics Today*, vol. 6, no. 11, pp. 4–9, 1953.

[28] R. Damadian, "Tumor detection by Nuclear Magnetic Resonance," *Science*, vol. 171, no. 3976, pp. 1151–1153, 1971.

[29] W. Perman, S. Hilal, H. Simon, and A. A. Maudsley, "Contrast manipulation in NMR imaging," *Magnetic Resonance Imaging*, vol. 2, no. 1, pp. 23–32, 1984.

[30] W. Nitz and P. Reimer, "Contrast mechanisms inMR imaging," *European radiology*, vol. 9, no. 6, pp. 1032–1046, 1999.

[31] J. Frahm, A. Haase, and D. Matthaei, "Rapid NMR imaging of dynamic processes using the FLASII technique," *Magnetic Resonance in Medicine*, vol. 3, no. 2, pp. 321–327, 1986.

[32] A. D. Elster, "Gradient-echo MR imaging: techniques and acronyms.," *Radiology*, vol. 186, no. 1, pp. 1–8, 1993.

[33] D. B. Plewes, "The AAPM/RSNA physics tutorial for residents. contrast mechanisms in spin-echo mr imaging.," *Radiographics*, vol. 14, no. 6, pp. 1389–1404, 1994.

[34] P. C. Lauterbur *et al.*, "Image formation by induced local interactions: examples employing nuclear Magnetic Resonance," 1973.

[35] D. B. Twieg, "The k-trajectory formulation of the NMR imaging process with applications in analysis and synthesis of imaging methods," *Medical Physics*, vol. 10, no. 5, pp. 610–621, 1983.

[36] K. F. King and P. R. Moran, "A unified description of NMR imaging, data-collection strategies, and reconstruction," *Medical Physics*, vol. 11, no. 1, pp. 1–14, 1984.

[37] S. Ljunggren, "A simple graphical representation of Fourier-based imaging methods," *Journal of Magnetic Resonance*, vol. 54, pp. 338–343, 1983.

[38] A. Kumar, D. Welti, and R. R. Ernst, "NMR fourier zeugmatography," *Journal of Magnetic Resonance (1969)*, vol. 18, no. 1, pp. 69–83, 1975.

[39] J. Hennig, "k-space sampling strategies," *European Radiology*, vol. 9, no. 6, pp. 1020–1031, 1999.

[40] M. Lustig, D. L. Donoho, J. M. Santos, and J. M. Pauly, "Compressed sensing MRI," *IEEE Signal Processing Magazine*, vol. 25, no. 2, p. 72, 2008.

[41] R. Mezrich, "A perspective on k-space.," *Radiology*, vol. 195, no. 2, pp. 297–315, 1995.

[42] E. Pusey, R. B. Lufkin, R. Brown, M. A. Solomon, D. D. Stark, R. Tarr, and W. Hanafee, "Magnetic Resonance Imaging artifacts: mechanism and clinical significance.," *Radiographics*, vol. 6, no. 5, pp. 891–911, 1986.

[43] D. W. McRobbie, E. A. Moore, M. J. Graves, and M. R. Prince, *MRI from Picture to Proton*. Cambridge university press, 2007.

[44] W. Edelstein, G. Glover, C. Hardy, and R. Redington, "The intrinsic signal-to-noise ratio in NMR imaging," *Magnetic Resonance in Medicine*, vol. 3, no. 4, pp. 604–618, 1986.

[45] O. Dietrich, J. G. Raya, S. B. Reeder, M. F. Reiser, and S. O. Schoenberg, "Measurement of signal-to-noise ratios in MR images: influence of multichannel coils, parallel imaging, and reconstruction filters," *Journal of Magnetic Resonance Imaging*, vol. 26, no. 2, pp. 375–385, 2007.

[46] T. W. Redpath, "Signal-to-noise ratio in MRI," *The British Journal of Radiology*, vol. 71, no. 847, pp. 704–707, 1998.

[47] L. B. Babcock, J. C. Weinreb, and S. D. Horner, "Edge artifacts in MR images: chemical shift effect," *J Comput Assist Tornogr*, vol. 9, no. 2, 1985.

[48] O. Ocali and E. Atalar, "Ultimate intrinsic signal-to-noise ratio in MRI," *Magnetic Resonance in Medicine*, vol. 39, no. 3, pp. 462–473, 1998.

[49] A. Macovski, "Noise in MRI," *Magnetic Resonance in Medicine*, vol. 36, no. 3, pp. 494–497, 1996.

[50] M. Firbank, A. Coulthard, R. Harrison, and E. Williams, "A comparison of two methods for measuring the signal to noise ratio on MR images," *Physics in Medicine & Biology*, vol. 44, no. 12, p. N261, 1999.

[51] J. Hornak, "The basics of MRI," May 10, 2005 1996.

[52] Y. Yanagawa, Y. Tsushima, A. Tokumaru, Y. Un-no, T. Sakamoto, Y. Okada, H. Nawashiro, and K. Shima, "A quantitative analysis of head injury using T2*-weighted gradient-echo imaging," *Journal of Trauma and Acute Care Surgery*, vol. 49, no. 2, pp. 272–277, 2000.

[53] F. Fazekas, R. Kleinert, G. Roob, G. Kleinert, P. Kapeller, R. Schmidt, and H.-P. Hartung, "Histopathologic analysis of foci of signal loss on Gradient-Echo T2*-weighted MR images in patients with spontaneous intracerebral hemorrhage: Evidence of microangiopathy-related microbleeds," *American Journal of Neuroradiology*, vol. 20, no. 4, pp. 637–642, 1999.

[54] A. McNeill, D. Birchall, S. J. Hayflick, A. Gregory, J. F. Schenk, E. A. Zimmerman, H. Shang, H. Miyajima, and P. F. Chinnery, "T2* and FSE MRI distinguishes four subtypes of neurodegeneration with brain iron accumulation," *Neurology*, vol. 70, no. 18, pp. 1614–1619, 2008.

[55] J. Dennie, J. B. Mandeville, J. L. Boxerman, S. D. Packard, B. R. Rosen, and R. M. Weisskoff, "NMR imaging of changes in vascular morphology due to tumor angiogenesis," *Magnetic Resonance in Medicine*, vol. 40, no. 6, pp. 793–799, 1998.

[56] H. An and W. Lin, "Cerebral oxygen extraction fraction and cerebral venous blood volume measurements using MRI: Effects of magnetic field variation," *Magnetic Resonance in Medicine*, vol. 47, no. 5, pp. 958–966, 2002.

[57] H. Dahnke and T. Schaeffter, "Limits of detection of SPIO at 3.0T using T2* relaxometry," *Magnetic Resonance in Medicine*, vol. 53, no. 5, pp. 1202–1206, 2005.

[58] "Quantitative mapping of T1 and T2* discloses nigral and brainstem pathology in early parkinson's disease," *NeuroImage*, vol. 51, no. 2, pp. 512 – 520, 2010.

[59] W. R. W. Martin, M. Wieler, and M. Gee, "Midbrain iron content in early parkinson disease," vol. 70, no. 16 Part 2, pp. 1411–1417, 2008.

[60] D. Aquino, A. Bizzi, M. Grisoli, B. Garavaglia, M. G. Bruzzone, N. Nardocci, M. Savoiardo, and L. Chiapparini, "Age-related iron deposition in the basal ganglia: Quantitative analysis in healthy subjects," *Radiology*, vol. 252, no. 1, pp. 165–172, 2009.

[61] C. Langkammer, C. Enzinger, S. Quasthoff, P. Grafenauer, M. Soellinger, F. Fazekas, and S. Ropele, "Mapping of iron deposition in conjunction with assessment of nerve fiber tract integrity in amyotrophic lateral sclerosis," *Journal of Magnetic Resonance Imaging*, vol. 31, no. 6, pp. 1339–1345, 2010.

[62] R. J. Ordidge, J. M. Gorell, J. C. Deniau, R. A. Knight, and J. A. Helpern, "Assessment of relative brain iron concentrations using T2-weighted and T2*-weighted MRI at 3 Tesla," *Magnetic Resonance in Medicine*, vol. 32, no. 3, pp. 335–341, 1994.

[63] B. Holst, S. Siemonsen, J. Finsterbusch, M. Bester, S. Schippling, R. Martin, and J. Fiehler, "T2' imaging indicates decreased tissue metabolism in frontal white matter of ms patients," *Multiple Sclerosis Journal*, vol. 15, no. 6, pp. 701–707, 2009. PMID: 19482862.

[64] S. Siemonsen, J. Finsterbusch, J. Matschke, A. Lorenzen, X.-Q. Ding, and J. Fiehler, "Age-dependent normal values of T2* and T2' in brain parenchyma," *American Journal of Neuroradiology*, vol. 29, no. 5, pp. 950–955, 2008.

[65] H. Y. Carr and E. M. Purcell, "Effects of diffusion on free precession in nuclear magnetic resonance experiments," *Physical review*, vol. 94, no. 3, p. 630, 1954.

[66] T. J. Sumpf, M. Uecker, S. Boretius, and J. Frahm, "Model-based nonlinear inverse reconstruction for T2 mapping using highly undersampled spin-echo MRI," *Journal of Magnetic Resonance Imaging*, vol. 34, no. 2, pp. 420–428, 2011.

[67] D. Neumann, M. Blaimer, P. M. Jakob, and F. A. Breuer, "Simple recipe for accurate T2 quantification with multi spin-echo acquisitions," *Magnetic Resonance Materials in Physics, Biology and Medicine*, vol. 27, no. 6, pp. 567–577, 2014.

[68] N. Lukzen, M. Petrova, I. Koptyug, A. Savelov, and R. Sagdeev, "The generating functions formalism for the analysis of spin response to the periodic trains of rf pulses. echo sequences with arbitrary refocusing angles and resonance offsets," *Journal of Magnetic Resonance*, vol. 196, no. 2, pp. 164–169, 2009.

[69] T. J. Sumpf, A. Petrovic, M. Uecker, F. Knoll, and J. Frahm, "Fast T2] mapping with improved accuracy using undersampled spin-echo MRI and model-based reconstructions with a generating function, journal = IEEE Transactions on Medical Imaging, volume = 33, number = 12, pages = 2213-2222, issn = 0278-0062, year = 2014, type = Journal Article,"

[70] N. Ben-Eliezer, D. K. Sodickson, and K. T. Block, "Rapid and accurate T2 mapping from multi–spin-echo data using bloch-simulation-based reconstruction," *Magnetic Resonance in Medicine*, vol. 73, no. 2, pp. 809–817, 2015.

[71] R. Van Heeswijk, D. Piccini, H. Feliciano, R. Hullin, J. Schwitter, and M. Stuber, "Self-navigated isotropic three-dimensional cardiac T2 mapping," *Magnetic Resonance in Medicine*, vol. 73, pp. 1549–1554, 4 2015.

[72] E. D. Crouser, C. Ono, T. Tran, X. He, and S. V. Raman, "Improved detection of cardiac sarcoidosis using magnetic resonance with myocardial t2 mapping," *American journal of respiratory and critical care medicine*, vol. 189, no. 1, pp. 109–112, 2014.

[73] A. A. Usman, K. Taimen, M. Wasielewski, J. McDonald, S. Shah, S. Giri, W. Cotts, E. McGee, R. Gordon, J. D. Collins, *et al.*, "Cardiac magnetic resonance T2 mapping in the monitoring and follow-up of acute cardiac transplant rejection: a pilot study," *Circulation: Cardiovascular Imaging*, vol. 5, no. 6, pp. 782–790, 2012.

[74] D. W. Goodwin, Y. Z. Wadghiri, and J. F. Dunn, "Micro-imaging of articular cartilage: T2, proton density, and the magic angle effect," *Academic radiology*, vol. 5, no. 11, pp. 790–798, 1998.

[75] C. Glaser, "New techniques for cartilage imaging: T2 relaxation time and diffusion-weighted mr imaging," *Radiologic Clinics*, vol. 43, no. 4, pp. 641–653, 2005.

[76] T. J. Mosher and B. J. Dardzinski, "Cartilage MRI T2 relaxation time mapping: overview and applications," in *Seminars in musculoskeletal radiology*, vol. 8, pp. 355–368, Copyright© 2004 by Thieme Medical Publishers, Inc., 333 Seventh Avenue, New ..., 2004.

[77] H.-L. Margaret Cheng, N. Stikov, N. R. Ghugre, and G. A. Wright, "Practical medical applications of quantitative MR relaxometry," *Journal of Magnetic Resonance Imaging*, vol. 36, no. 4, pp. 805–824, 2012.

[78] I. Blystad, J. M. Warntjes, Ö. Smedby, P. Lundberg, E.-M. Larsson, and A. Tisell, "Quantitative MRI for analysis of peritumoral edema in malignant gliomas," *PLoS One*, vol. 12, no. 5, p. e0177135, 2017.

[79] M. House, T. S. Pierre, J. Foster, R. Martins, and R. Clarnette, "Quantitative MR imaging R2 relaxometry in elderly participants reporting memory loss," *American journal of neuroradiology*, vol. 27, no. 2, pp. 430–439, 2006.

[80] P. Mansfield, "Multi-planar image formation using NMR spin echoes," *Journal of Physics C: Solid State Physics*, vol. 10, no. 3, p. L55, 1977.

[81] J. Hennig, "Multiecho imaging sequences with low refocusing flip angles," *Journal of Magnetic Resonance (1969)*, vol. 78, no. 3, pp. 397–407, 1988.

[82] A. Haase, J. Frahm, D. Matthaei, W. Hänicke, and K.-D. Merboldt, "FLASH imaging: Rapid NMR imaging using low flip-angle pulses," *Journal of Magnetic Resonance*, vol. 213, no. 2, pp. 533 – 541, 2011. Magnetic Moments.

[83] K. Oshio and D. A. Feinberg, "GRASE (gradient-and spin-echo) imaging: A novel fast MRI technique," *Magnetic Resonance in Medicine*, vol. 20, no. 2, pp. 344–349, 1991.

[84] D. C. Noll, F. E. Boada, and W. F. Eddy, "A spectral approach to analyzing slice selection in planar imaging: optimization for through-plane interpolation," *Magnetic Resonance in Medicine*, vol. 38, no. 1, pp. 151–160, 1997.

[85] D. A. Feinberg and K. Setsompop, "Ultra-fast MRI of the human brain with simultaneous multi-slice imaging," *Journal of magnetic resonance*, vol. 229, pp. 90–100, 2013.

[86] J. B. Ra and C. Y. Rim, "Fast imaging using subencoding data sets from multiple detectors," *Magnetic Resonance in Medicine*, vol. 30, no. 1, pp. 142–145, 1993.

[87] D. K. Sodickson and W. J. Manning, "Simultaneous acquisition of spatial harmonics (SMASH): fast imaging with radiofrequency coil arrays," *Magnetic Resonance in Medicine*, vol. 38, no. 4, pp. 591–603, 1997.

[88] K. P. Pruessmann, M. Weiger, P. Börnert, and P. Boesiger, "Advances in sensitivity encoding with arbitrary k-space trajectories," *Magnetic Resonance in Medicine*, vol. 46, no. 4, pp. 638–651, 2001.

[89] R. M. Heidemann, M. A. Griswold, A. Haase, and P. M. Jakob, "VD-AUTO-SMASH imaging," *Magnetic Resonance in Medicine*, vol. 45, no. 6, pp. 1066–1074, 2001.

[90] P. M. Jakob, M. A. Grisowld, R. R. Edelman, and D. K. Sodickson, "AUTO-SMASH: A self-calibrating technique for smash imaging," *Magnetic Resonance Materials in Physics, Biology and Medicine*, vol. 7, pp. 42–54, Nov 1998.

[91] C. A. McKenzie, E. N. Yeh, M. A. Ohliger, M. D. Price, and D. K. Sodickson, "Self-calibrating parallel imaging with automatic coil sensitivity extraction," *Magnetic Resonance in Medicine*, vol. 47, no. 3, pp. 529–538, 2002.

[92] M. Bydder, D. Larkman, and J. Hajnal, "Combination of signals from array coils using image-based estimation of coil sensitivity profiles," *Magnetic Resonance in Medicine*, vol. 47, no. 3, pp. 539–548, 2002.

[93] F.-H. Lin, Y.-J. Chen, J. W. Belliveau, and L. L. Wald, "A wavelet-based approximation of surface coil sensitivity profiles for correction of image intensity inhomogeneity and parallel imaging reconstruction," *Human Brain Mapping*, vol. 19, no. 2, pp. 96–111, 2003.

[94] M. Uecker, T. Hohage, K. T. Block, and J. Frahm, "Image reconstruction by regularized nonlinear inversion—joint estimation of coil sensitivities and image content," *Magnetic Resonance in Medicine*, vol. 60, no. 3, pp. 674–682, 2008.

[95] L. Ying and J. Sheng, "Joint image reconstruction and sensitivity estimation in sense (JSENSE)," *Magnetic Resonance in Medicine*, vol. 57, no. 6, pp. 1196–1202, 2007.

[96] D. K. Sodickson and W. J. Manning, "Simultaneous acquisition of spatial harmonics (SMASH): Fast imaging with radiofrequency coil arrays," *Magnetic Resonance in Medicine*, vol. 38, no. 4, pp. 591–603, 1997.

[97] M. Blaimer, F. A. Breuer, M. Mueller, N. Seiberlich, D. Ebel, R. M. Heidemann, M. A. Griswold, and P. M. Jakob, "2D-GRAPPA-operator for faster 3D parallel MRI," *Magnetic Resonance in Medicine*, vol. 56, no. 6, pp. 1359–1364, 2006.

[98] F. Huang, J. Akao, S. Vijayakumar, G. R. Duensing, and M. Limkeman, "k-t GRAPPA: A k-space implementation for dynamic MRI with high reduction factor," *Magnetic Resonance in Medicine*, vol. 54, no. 5, pp. 1172–1184, 2005.

[99] C. Liu, R. Bammer, and M. E. Moseley, "Parallel imaging reconstruction for arbitrary trajectories using k-space sparse matrices (kSPA)," *Magnetic Resonance in Medicine*, vol. 58, no. 6, pp. 1171–1181, 2007.

[100] N. Seiberlich, F. A. Breuer, M. Blaimer, K. Barkauskas, P. M. Jakob, and M. A. Griswold, "Non-cartesian data reconstruction using grappa operator gridding (GROG)," *Magnetic Resonance in Medicine*, vol. 58, no. 6, pp. 1257–1265, 2007.

[101] M. Lustig and J. M. Pauly, "SPIRiT: Iterative self-consistent parallel imaging reconstruction from arbitrary k-space," *Magnetic Resonance in Medicine*, vol. 64, no. 2, pp. 457–471, 2010.

[102] M. Guerquin-Kern, D. Van De Ville, C. Vonesch, J.-C. Baritaux, K. P. Pruessmann, and M. Unser, "Wavelet-regularized reconstruction for rapid mri," in *Proceedings of the Sixth IEEE International Conference on Symposium on Biomedical Imaging: From Nano to Macro*, ISBI'09, (Piscataway, NJ, USA), pp. 193–196, IEEE Press, 2009.

[103] S. Esedoḡlu and S. J. Osher, "Decomposition of images by the anisotropic rudin-osher-fatemi model," *Communications on Pure and Applied Mathematics*, vol. 57, no. 12, pp. 1609–1626, 2004.

[104] T. Chan, S. Esedoglu, F. Park, and A. Yip, "Recent developments in total variation image restoration," in *In Mathematical Models of Computer Vision*, Springer Verlag, 2005.

[105] K. T. Block, M. Uecker, and J. Frahm, "Model-based iterative reconstruction for radial fast spin-echo MRI," *IEEE transactions on medical imaging*, vol. 28, no. 11, pp. 1759–1769, 2009.

[106] A. Ben-Ezra, H. Greenspan, and Y. Rubner, "Regularized super-resolution of brain MRI," in *2009 IEEE International Symposium on Biomedical Imaging: From Nano to Macro*, pp. 254–257, IEEE, 2009.

[107] M. Murphy, M. Alley, J. Demmel, K. Keutzer, S. Vasanawala, and M. Lustig, "Fastl_1-SPIRiT compressed sensing parallel imaging MRI: Scalable parallel implementation and clinically feasible runtime," *IEEE Transactions on Medical Imaging*, vol. 31, June 2012.

[108] M. Uecker, P. Lai, M. J. Murphy, P. Virtue, M. Elad, J. M. Pauly, S. S. Vasanawala, and M. Lustig, "ESPIRiT—an eigenvalue approach to autocalibrating parallel MRI: Where SENSE meets GRAPPA," *Magnetic Resonance in Medicine*, vol. 71, no. 3, pp. 990–1001, 2014.

[109] H. Jung, J. C. Ye, and E. Y. Kim, "Improved k-t BLAST and k-t SENSE using FOCUSS," *Physics in Medicine & Biology*, vol. 52, no. 11, p. 3201, 2007.

[110] H. Jung, K. Sung, K. S. Nayak, E. Y. Kim, and J. C. Ye, "k-t FOCUSS: a general compressed sensing framework for high resolution dynamic MRI," *Magnetic Resonance in Medicine*, vol. 61, no. 1, pp. 103–116, 2009.

[111] D. Liang, B. Liu, J. Wang, and L. Ying, "Accelerating SENSE using compressed sensing," *Magnetic Resonance in Medicine*, vol. 62, no. 6, pp. 1574–1584, 2009.

[112] R. Otazo, D. Kim, L. Axel, and D. K. Sodickson, "Combination of compressed sensing and parallel imaging for highly accelerated first-pass cardiac perfusion MRI," *Magnetic Resonance in Medicine*, vol. 64, no. 3, pp. 767–776, 2010.

[113] M. Lustig and J. M. Pauly, "SPIRiT: Iterative self-consistent parallel imaging reconstruction from arbitrary k-space," *Magnetic Resonance in Medicine*, vol. 64, no. 2, pp. 457–471, 2010.

[114] S. Ravishankar and Y. Bresler, "MR image reconstruction from highly undersampled k-space data by dictionary learning," *IEEE Transactions on Medical Imaging*, vol. 30, no. 5, pp. 1028–1041, 2011.

[115] S. Ravishankar and Y. Bresler, "Blind compressed sensing using sparsifying transforms," in *2015 International Conference on Sampling Theory and Applications (SampTA)*, pp. 513–517, IEEE, 2015.

[116] R. Otazo and D. Sodickson, "Adaptive compressed sensing MRI," in *Proceedings of the 18th Scientific Meeting of ISMRM, Stockholm*, p. 4867, 2010.

[117] U. Gamper, P. Boesiger, and S. Kozerke, "Compressed sensing in dynamic MRI," *Magnetic Resonance in Medicine*, vol. 59, no. 2, pp. 365–373, 2008.

[118] M. Lustig, J. M. Santos, D. L. Donoho, and J. M. Pauly, "kt SPARSE: High frame rate dynamic MRI exploiting spatio-temporal sparsity," in *Proceedings of the 13th Annual Meeting of ISMRM, Seattle*, vol. 2420, 2006.

[119] J. Tsao, P. Boesiger, and K. P. Pruessmann, "k-t BLAST and k-t SENSE: dynamic MRI with high frame rate exploiting spatiotemporal correlations," *Magnetic Resonance in Medicine*, vol. 50, no. 5, pp. 1031–1042, 2003.

[120] P. J. Shin, P. E. Z. Larson, M. A. Ohliger, M. Elad, J. M. Pauly, D. B. Vigneron, and M. Lustig, "Calibrationless parallel imaging reconstruction based on structured low-rank matrix completion," *Magnetic Resonance in Medicine*, vol. 72, no. 4, pp. 959–970, 2014.

[121] J. P. Haldar, "Low-rank modeling of local k-space neighborhoods (LORAKS) for constrained MRI," *IEEE transactions on medical imaging*, vol. 33, no. 3, pp. 668–681, 2014.

[122] K. H. Jin, D. Lee, and J. C. Ye, "A general framework for compressed sensing and parallel mri using annihilating filter based low-rank hankel matrix," *IEEE Transactions on Computational Imaging*, vol. 2, pp. 480–495, Dec 2016.

[123] D. Lee, K. H. Jin, E. Y. Kim, S.-H. Park, and J. C. Ye, "Acceleration of MR parameter mapping using annihilating filter-based low rank hankel matrix (ALOHA)," *Magnetic Resonance in Medicine*, vol. 76, no. 6, pp. 1848–1864, 2016.

[124] J. V. Velikina, A. L. Alexander, and A. Samsonov, "Accelerating MR parameter mapping using sparsity-promoting regularization in parametric dimension," *Magnetic resonance in medicine*, vol. 70, no. 5, pp. 1263–1273, 2013.

[125] T. Zhang, J. M. Pauly, and I. R. Levesque, "Accelerating parameter mapping with a locally low rank constraint," *Magnetic Resonance in Medicine*, vol. 73, no. 2, pp. 655–661, 2015.

[126] B. Zhao, W. Lu, T. K. Hitchens, F. Lam, C. Ho, and Z.-P. Liang, "Accelerated MR parameter mapping with low-rank and sparsity constraints," *Magnetic Resonance in Medicine*, vol. 74, no. 2, pp. 489–498, 2015.

[127] C. Huang, C. G. Graff, E. W. Clarkson, A. Bilgin, and M. I. Altbach, "T2 mapping from highly undersampled data by reconstruction of principal component coefficient maps using compressed sensing," *Magnetic Resonance in Medicine*, vol. 67, no. 5, pp. 1355–1366, 2012.

[128] F. H. Petzschner, I. P. Ponce, M. Blaimer, P. M. Jakob, and F. A. Breuer, "Fast MR parameter mapping using k-t principal component analysis," *Magnetic Resonance in Medicine*, vol. 66, no. 3, pp. 706–716, 2011.

[129] G. Vincenti, P. Monney, J. Chaptinel, T. Rutz, S. Coppo, M. O. Zenge, M. Schmidt, M. S. Nadar, D. Piccini, P. Chèvre, *et al.*, "Compressed sensing single–breath-hold CMR for fast quantification of LV function, volumes, and mass," *JACC: Cardiovascular Imaging*, vol. 7, no. 9, pp. 882–892, 2014.

[130] B. A. Landman, J. A. Bogovic, H. Wan, F. E. Z. ElShahaby, P.-L. Bazin, and J. L. Prince, "Resolution of crossing fibers with constrained compressed sensing using diffusion tensor MRI," *NeuroImage*, vol. 59, no. 3, pp. 2175–2186, 2012.

[131] M. Doneva, P. Börnert, H. Eggers, C. Stehning, J. Sénégas, and A. Mertins, "Compressed sensing reconstruction for Magnetic Resonance parameter mapping," *Magnetic Resonance in Medicine*, vol. 64, no. 4, pp. 1114–1120, 2010.

[132] V. T. Olafsson, D. C. Noll, and J. A. Fessler, "Fast joint reconstruction of dynamic R_2^* and field maps in functional MRI," *IEEE Transactions on Medical Imaging*, vol. 27, pp. 1177–1188, Sep. 2008.

[133] J. Tran-Gia, T. Wech, T. Bley, and H. Köstler, "Model-based acceleration of look-locker T1 mapping," *PLOS ONE*, vol. 10, pp. 1–15, 04 2015.

[134] J. Tran-Gia, D. Stäb, T. Wech, D. Hahn, and H. Köstler, "Model-based acceleration of parameter mapping (MAP) for saturation prepared radially acquired data," *Magnetic Resonance in Medicine*, vol. 70, no. 6, pp. 1524–1534, 2013.

[135] X. Wang, V. Roeloffs, J. Klosowski, Z. Tan, D. Voit, M. Uecker, and J. Frahm, "Model-based T1 mapping with sparsity constraints using single-shot inversion-recovery radial FLASH," *Magnetic Resonance in Medicine*, vol. 79, no. 2, pp. 730–740, 2018.

[136] M. Doneva, P. Börnert, H. Eggers, A. Mertins, J. Pauly, and M. Lustig, "Compressed sensing for chemical shift-based water–fat separation," *Magnetic Resonance in Medicine*, vol. 64, no. 6, pp. 1749–1759, 2010.

[137] D. Ma, V. Gulani, N. Seiberlich, K. Liu, J. L. Sunshine, J. L. Duerk, and M. A. Griswold, "Magnetic resonance fingerprinting," *Nature*, vol. 495, no. 7440, p. 187, 2013.

[138] M. Davies, G. Puy, P. Vandergheynst, and Y. Wiaux, "A Compressed Sensing Framework for Magnetic Resonance Fingerprinting," *SIAM Journal on Imaging Sciences*, vol. 7, no. 4, pp. 2623–2656, 2014.

[139] C. N. Wiens, C. M. McCurdy, J. D. Willig-Onwuachi, and C. A. McKenzie, "-corrected water–fat imaging using compressed sensing and parallel imaging," *Magnetic Resonance in Medicine*, vol. 71, no. 2, pp. 608–616, 2014.

[140] S. D. Sharma, H. H. Hu, and K. S. Nayak, "Chemical shift encoded water–fat separation using parallel imaging and compressed sensing," *Magnetic Resonance in Medicine*, vol. 69, no. 2, pp. 456–466, 2013.

[141] B. Wu, W. Li, A. Guidon, and C. Liu, "Whole brain susceptibility mapping using compressed sensing," *Magnetic Resonance in Medicine*, vol. 67, no. 1, pp. 137–147, 2012.

[142] M. Doneva, P. Börnert, H. Eggers, A. Mertins, J. Pauly, and M. Lustig, "Compressed sensing for chemical shift-based water–fat separation," *Magnetic Resonance in Medicine*, vol. 64, no. 6, pp. 1749–1759, 2010.

[143] M. Kang and S. Chaudhuri, "Super-resolution image reconstruction," *IEEE Signal Processing Magazine*, vol. 20, pp. 19–20, 1 2003.

[144] S. C. Park, M. K. Park, and M. G. Kang, "Super-resolution image reconstruction: a technical overview," *IEEE Signal Processing Magazine*, vol. 20, no. 3, pp. 21–36, 2003.

[145] S. Farsiu, D. Robinson, M. Elad, and P. Milanfar, "Advances and challenges in super-resolution," *International Journal of Imaging Systems and Technology*, vol. 14, no. 2, pp. 47–57, 2004.

[146] E. Van Reeth, I. W. Tham, C. H. Tan, and C. L. Poh, "Super-resolution in Magnetic Resonance Imaging: a review," *Concepts in Magnetic Resonance Part A*, vol. 40, no. 6, pp. 306–325, 2012.

[147] M. A. Bernstein, K. F. King, and X. J. Zhou, *Handbook of MRI pulse sequences*. Elsevier, 2004.

[148] E. Plenge, D. H. Poot, M. Bernsen, G. Kotek, G. Houston, P. Wielopolski, L. van der Weerd, W. J. Niessen, and E. Meijering, "Super-resolution methods in MRI: Can they improve the trade-off between resolution, signal-to-noise ratio, and acquisition time?," *Magnetic Resonance in Medicine*, vol. 68, no. 6, pp. 1983–1993, 2012.

[149] R. Z. Shilling, *A multi-stack framework in Magnetic Resonance Imaging*. PhD thesis, Georgia Institute of Technology, 2009.

[150] S. P. Kim and W. . Su, "Recursive high-resolution reconstruction of blurred multiframe images," *IEEE Transactions on Image Processing*, vol. 2, pp. 534–539, Oct 1993.

[151] S. Kim, N. K. Bose, and H. Valenzuela, "Recursive reconstruction of high resolution image from noisy undersampled multiframes," *IEEE Transactions on Acoustics, Speech, and Signal Processing*, vol. 38, no. 6, pp. 1013–1027, 1990.

[152] R. Tsai and T. Huang, "Moving image restoration and registration," in *ICASSP'80. IEEE International Conference on Acoustics, Speech, and Signal Processing*, vol. 5, pp. 418–421, IEEE, 1980.

[153] J. G. Pipe, "Motion correction with PROPELLER MRI: application to head motion and free-breathing cardiac imaging," *Magnetic Resonance in Medicine*, vol. 42, no. 5, pp. 963–969, 1999.

[154] K. Setsompop, J. Cohen-Adad, B. Gagoski, T. Raij, A. Yendiki, B. Keil, V. J. Wedeen, and L. L. Wald, "Improving diffusion MRI using simultaneous multi-slice echo planar imaging," *NeuroImage*, vol. 63, no. 1, pp. 569–580, 2012.

[155] D. Fiat, "Method of enhancing an MRI signal," *Number US Patent*, vol. 6, 1997.

[156] S. Peled and Y. Yeshurun, "Superresolution in MRI—perhaps sometimes," *Magnetic Resonance in Medicine*, vol. 48, no. 2, pp. 409–409, 2002.

[157] E. Carmi, S. Liu, N. Alon, A. Fiat, and D. Fiat, "Resolution enhancement in MRI," *Magnetic Resonance Imaging*, vol. 24, no. 2, pp. 133–154, 2006.

[158] K. Scheffler, "Superresolution in MRI?," *Magnetic Resonance in Medicine*, vol. 48, no. 2, pp. 408–408, 2002.

[159] D. H. Poot, V. Van Meir, and J. Sijbers, "General and efficient super-resolution method for multi-slice MRI," in *International Conference on Medical Image Computing and Computer-Assisted Intervention*, pp. 615–622, Springer, 2010.

[160] J. G. Pipe, "Asymmetric sampling along kslice-select in two-dimensional multislice MRI," *Magnetic Resonance in Medicine*, vol. 39, no. 4, pp. 625–634, 1998.

[161] R. Z. Shilling, S. Ramamurthy, and M. E. Brummer, "Sampling strategies for super-resolution in multi-slice MRI," in *2008 15th IEEE International Conference on Image Processing*, pp. 2240–2243, IEEE, 2008.

[162] F. Peeters, L. Annet, L. Hermoye, and B. E. Van Beers, "Inflow correction of hepatic perfusion measurements using T1-weighted, fast gradient-echo, contrast-enhanced MRI," *Magnetic Resonance in Medicine*, vol. 51, no. 4, pp. 710–717, 2004.

[163] B. Scherrer, A. Gholipour, and S. K. Warfield, "Super-resolution reconstruction to increase the spatial resolution of diffusion weighted images from orthogonal anisotropic acquisitions," *Medical Image Analysis*, vol. 16, no. 7, pp. 1465–1476, 2012.

[164] D. H. Poot, B. Jeurissen, Y. Bastiaensen, J. Veraart, W. Van Hecke, P. M. Parizel, and J. Sijbers, "Super-resolution for multislice diffusion tensor imaging," *Magnetic Resonance in Medicine*, vol. 69, no. 1, pp. 103–113, 2013.

[165] M. Fogtmann, S. Seshamani, C. Kroenke, X. Cheng, T. Chapman, J. Wilm, F. Rousseau, and C. Studholme, "A unified approach to diffusion direction sensitive slice registration and 3-D DTI reconstruction from moving fetal brain anatomy," *IEEE Transactions on Medical Imaging*, vol. 33, no. 2, pp. 272–289, 2014.

[166] F. Rousseau, O. A. Glenn, B. Iordanova, C. Rodriguez-Carranza, D. B. Vigneron, J. A. Barkovich, and C. Studholme, "Registration-based approach for reconstruction of high-resolution in utero fetal MR brain images," *Academic radiology*, vol. 13, no. 9, pp. 1072–1081, 2006.

[167] F. Rousseau, K. Kim, C. Studholme, M. Koob, and J.-L. Dietemann, "On super-resolution for fetal brain MRI," in *International Conference on Medical Image Computing and Computer-Assisted Intervention*, pp. 355–362, Springer, 2010.

[168] A. Gholipour, J. A. Estroff, and S. K. Warfield, "Robust super-resolution volume reconstruction from slice acquisitions: application to fetal brain MRI," *IEEE Transactions on Medical Imaging*, vol. 29, no. 10, pp. 1739–1758, 2010.

[169] E. Oubel, M. Koob, C. Studholme, J.-L. Dietemann, and F. Rousseau, "Reconstruction of scattered data in fetal diffusion MRI," *Medical Image Analysis*, vol. 16, no. 1, pp. 28–37, 2012.

[170] G. Van Steenkiste, D. H. Poot, B. Jeurissen, A. J. Den Dekker, F. Vanhevel, P. M. Parizel, and J. Sijbers, "Super-resolution T1 estimation: Quantitative high resolution T1 mapping from a set of low resolution T1-weighted images with different slice orientations," *Magnetic Resonance in Medicine*, vol. 77, no. 5, pp. 1818–1830, 2017.

[171] H. Gudbjartsson and S. Patz, "The Rician distribution of noisy MRI data," *Magnetic Resonance in Medicine*, vol. 34, no. 6, pp. 910–914, 1995.

[172] J.-M. Bonny, M. Zanca, J.-Y. Boire, and A. Veyre, "T2 maximum likelihood estimation from multiple spin-echo magnitude images," *Magnetic Resonance in Medicine*, vol. 36, no. 2, pp. 287–293, 1996.

[173] J. Sijbers and A. Den Dekker, "Maximum likelihood estimation of signal amplitude and noise variance from MR data," *Magnetic Resonance in Medicine*, vol. 51, no. 3, pp. 586–594, 2004.

[174] P. A. Hardy and A. H. Andersen, "Calculating T2 in images from a phased array receiver," *Magnetic Resonance in Medicine*, vol. 61, no. 4, pp. 962–969, 2009.

[175] P. B. Roemer, W. A. Edelstein, C. E. Hayes, S. P. Souza, and O. Mueller, "The NMR phased array," *Magnetic Resonance in Medicine*, vol. 16, no. 2, pp. 192–225, 1990.

[176] R. Escalante and M. Raydan, *Alternating Projection Methods*. Philadelphia, PA, USA: Society for Industrial and Applied Mathematics, 2011.

[177] D. Dunbar and G. Humphreys, "A spatial data structure for fast poisson-disk sample generation," in *ACM Transactions on Graphics (TOG)*, vol. 25, pp. 503–508, ACM, 2006.

[178] Y. Jiang, D. Ma, K. E. Keenan, K. F. Stupic, V. Gulani, and M. A. Griswold, "Repeatability of magnetic resonance fingerprinting t1 and t2 estimates assessed using the ismrm/nist mri system phantom," *Magnetic resonance in medicine*, vol. 78, no. 4, pp. 1452–1457, 2017.

[179] M. Lustig, D. L. Donoho, J. M. Santos, and J. M. Pauly, "Compressed sensing MRI," *Signal Processing Magazine, IEEE*, vol. 25, no. 2, pp. 72–82, 2008.

[180] V. T. Olafsson, D. C. Noll, and J. A. Fessler, "Fast joint reconstruction of dynamic R2* and field maps in functional MRI," *IEEE Trans. Med. Imaging*, vol. 27, no. 9, pp. 1177–1188, 2008.

[181] T. Knopp, H. Eggers, H. Dahnke, J. Prestin, and J. Senegas, "Iterative off-resonance and signal decay estimation and correction for multi-echo MRI," *IEEE transactions on medical imaging*, vol. 28, no. 3, pp. 394–404, 2009.

[182] G. C. Ngo and B. P. Sutton, "R2* mapping for robust brain function detection in the presence of magnetic field inhomogeneity," in *Engineering in Medicine and Biology Society (EMBC), 2014 36th Annual International Conference of the IEEE*, pp. 1537–1540, IEEE, 2014.

[183] K. T. Block, M. Uecker, and J. Frahm, "Model-based iterative reconstruction for radial fast spin-echo MRI," *IEEE transactions on medical imaging*, vol. 28, no. 11, pp. 1759–1769, 2009.

[184] A. Beck and M. Teboulle, "A fast iterative shrinkage-thresholding algorithm for linear inverse problems," *SIAM Journal on Imaging Sciences*, vol. 2, no. 1, pp. 183–202, 2009.

[185] N. Perraudin, D. Shuman, G. Puy, and P. Vandergheynst, "Unlocbox: A matlab convex optimization toolbox using proximal splitting methods," *arXiv preprint arXiv:1402.0779*, 2014.

[186] S. Aja-Fernández and A. Tristán-Vega, "Influence of noise correlation in multiple-coil statistical models with sum of squares reconstruction," *Magnetic Resonance in Medicine*, vol. 67, no. 2, pp. 580–585, 2012.

[187] I. Marshall, G. Rilling, Y. Tao, C. Du, S. Varma, D. Job, A. Farrall, and M. Davies, "Radiological and quantitative assessment of compressed sensing reconstruction of undersampled 3d brain images," 5 2015. ISMRM 23rd Annual Meeting and Exhibition ; Conference date: 30-05-2015 Through 05-06-2015.

[188] M. A. Griswold, D. Walsh, R. M. Heidemann, A. Haase, and P. M. Jakob, "The use of an adaptive reconstruction for array coil sensitivity mapping and intensity normalization," *Proc. Intl. Soc. Mag. Reson. Med.*, 2002.

[189] Z. Wang, A. C. Bovik, H. R. Sheikh, E. P. Simoncelli, *et al.*, "Image quality assessment: from error visibility to structural similarity," *IEEE transactions on image processing*, vol. 13, no. 4, pp. 600–612, 2004.

[190] B. Bilgic, A. Pfefferbaum, T. Rohlfing, E. V. Sullivan, and E. Adalsteinsson, "MRI estimates of brain iron concentration in normal aging using quantitative susceptibility mapping," *NeuroImage*, vol. 59, no. 3, pp. 2625–2635, 2012.

[191] F.-H. Lin, K. K. Kwong, J. W. Belliveau, and L. L. Wald, "Parallel imaging reconstruction using automatic regularization," *Magnetic Resonance in Medicine*, vol. 51, no. 3, pp. 559–567, 2004.

[192] A. Petrovic, E. Scheurer, and R. Stollberger, "Closed-form solution for T2 mapping with nonideal refocusing of slice selective CPMG sequences," *Magnetic Resonance in Medicine*, vol. 73, no. 2, pp. 818–827, 2015.

[193] K. C. McPhee and A. H. Wilman, "Limitations of skipping echoes for exponential T2 fitting," *Journal of Magnetic Resonance Imaging*, vol. 48, no. 5, pp. 1432–1440, 2018.

[194] F. H. Petzschner, I. P. Ponce, M. Blaimer, P. M. Jakob, and F. A. Breuer, "Fast MR parameter mapping using k-t principal component analysis," *Magnetic Resonance in Medicine*, vol. 66, no. 3, pp. 706–716, 2011.

[195] K. Setsompop, Q. Fan, J. Stockmann, B. Bilgic, S. Huang, S. F. Cauley, A. Nummenmaa, F. Wang, Y. Rathi, and T. Witzel, "High-resolution in vivo diffusion imaging of the human brain with generalized slice dithered enhanced resolution: Simultaneous multislice (g-s lider-SMS)," *Magnetic Resonance in Medicine*, vol. 79, no. 1, pp. 141–151, 2018.

[196] G. Van Steenkiste, B. Jeurissen, J. Veraart, A. J. Den Dekker, P. M. Parizel, D. H. Poot, and J. Sijbers, "Super-resolution reconstruction of diffusion parameters from diffusion-weighted images with different slice orientations," *Magnetic Resonance in Medicine*, vol. 75, no. 1, pp. 181–195, 2016.

[197] T. Hilbert, J. P. Marques, J.-P. Thiran, R. Meuli, G. Krueger, and T. Kober, "Model-based super-resolution reconstruction of T2 maps," in *Proc. Intl. Soc. Mag. Reson. Med*.

[198] W. Bano, M. Piredda, Gian Franco Davies, I. Marshall, M. Golbabbaee, R. Meuli, T. Kober, J.-P. Thiran, and Hilbert, "High-resolution isotropic whole brain T2 mapping with model-based super-resolution reconstruction.," in *Proc. Intl. Soc. Mag. Reson. Med*.

[199] T. Hilbert, J.-P. Thiran, R. Meuli, G. Krueger, and T. Kober, "SAFT: Split-algorithm for fast T2 mapping," in *Proc. Intl. Soc. Mag. Reson. Med*, vol. 24.

[200] M. Guerquin-Kern, L. Lejeune, K. P. Pruessmann, and M. Unser, "Realistic analytical phantoms for parallel magnetic resonance imaging," *IEEE Transactions on Medical Imaging*, vol. 31, no. 3, pp. 626–636, 2012.

[201] S. Klein, M. Staring, K. Murphy, M. A. Viergever, and J. P. Pluim, "Elastix: a toolbox for intensity-based medical image registration," *IEEE Transactions on Medical Imaging*, vol. 29, no. 1, pp. 196–205, 2010.

[202] M. Barth, F. Breuer, P. J. Koopmans, D. G. Norris, and B. A. Poser, "Simultaneous multislice (SMS) imaging techniques," *Magnetic Resonance in Medicine*, vol. 75, no. 1, pp. 63–81, 2016.

[203] T. Hilbert, J. Schulz, L. J. Bains, J. P. Marques, R. Meuli, J.-P. Thiran, G. Krueger, D. Norris, and T. Kober, "Fast quantitative T2 mapping using simultaneous-multi-slice and model-based reconstruction," in *ISMRM 2016, ISMRM 24rd Annual Meeting Exhibition, SMRT 25th Annual Meeting*.

[204] D. B. Pier, A. Gholipour, O. Afacan, C. Velasco-Annis, S. Clancy, K. Kapur, J. A. Estroff, and S. K. Warfield, "3D super-resolution motion-corrected MRI: Validation of fetal posterior fossa measurements," *Journal of Neuroimaging*, vol. 26, no. 5, pp. 539–544, 2016.

[205] S. Tourbier, X. Bresson, P. Hagmann, J.-P. Thiran, R. Meuli, and M. B. Cuadra, "An efficient total variation algorithm for super-resolution in fetal brainMRI with adaptive regularization," *NeuroImage*, vol. 118, pp. 584–597, 2015.

[206] A. Benjamin, "The clinical condition to be assessed by radiological assessment significantly influences the radiological scores of compressed sensing accelerated 3D brain MRI," 4 2019. ISMRM 27th Annual Meeting amp; Exhibition, 11-16 May 2019 ; Conference date: 11-05-2019 Through 16-05-2019.

[207] H. Wang, H. Peng, Y. Chang, and D. Liang, "A survey of GPU-based acceleration techniques in mri reconstructions," *Quantitative Imaging in Medicine and Surgery*, vol. 8, no. 2, p. 196, 2018.

[208] F.-H. Lin, K. K. Kwong, J. W. Belliveau, and L. L. Wald, "Parallel imaging reconstruction using automatic regularization," *Magnetic Resonance in Medicine: An Official Journal of the International Society for Magnetic Resonance in Medicine*, vol. 51, no. 3, pp. 559–567, 2004.

[209] F. Lin, K. Kwong, Y. Chen, J. Belliveau, and L. Wald, "Reconstruction of sensitivity encoded images using regularization and discrete time wavelet transform estimates of the coil maps," in *Proceedings of the 10th Annual Meeting of ISMRM, Honolulu, HI, USA*, p. 2389, 2002.

[210] K. King and L. Angelos, "Sense image quality improvement using matrix regularization," in *Proceedings of the 9th Annual Meeting of ISMRM, Glasgow, Scotland*, p. 1771, 2001.

[211] J. Tsao, K. Pruessmann, and P. Boesiger, "Prior-information-enhanced dynamic imaging using single or multiple coils with kt BLAST and kt SENSE," in *Proceedings of the 10th Annual Meeting of ISMRM, Honolulu*, p. 2369, 2002.

[212] C. Qin, J. Schlemper, J. Caballero, A. N. Price, J. V. Hajnal, and D. Rueckert, "Convolutional recurrent neural networks for dynamic MR image reconstruction," *IEEE Transactions on Medical Imaging*, vol. 38, no. 1, pp. 280–290, 2018.

[213] O. Cohen, B. Zhu, and M. S. Rosen, "Mr fingerprinting deep reconstruction network (DRONE)," *Magnetic resonance in medicine*, vol. 80, no. 3, pp. 885–894, 2018.

[214] E. Hoppe, G. Körzdörfer, T. Würfl, J. Wetzl, F. Lugauer, J. Pfeuffer, and A. K. Maier, "Deep learning for Magnetic Resonance Fingerprinting: A new approach for predicting quantitative parameter values from time series.," in *GMDS*, pp. 202–206, 2017.